(26)

Analysis of Blade-Mounted Servoflap Actuation for Active Helicopter Rotor Control

by

Masahiko Kuzume Ikuta

B.S., Cornell University (1993)

Submitted to the Department of Aeronautics and Astronautics
in partial fulfillment of the requirements
for the degree of

Master of Science in Aeronautics and Astronautics

at the

Massachusetts Institute of Technology

September 1995

Author_____
Department of Aeronautics and Astronautics
August 23, 1995

Certified by_____
Professor Steven R. Hall
Department of Aeronautics and Astronautics
Thesis Supervisor

Accepted by_____
Professor Harold Y. Wachman
Chairman, Departmental Graduate Committee

Analysis of Blade-Mounted Servoflap Actuation for Active Helicopter Rotor Control

by

Masahiko Kuzume Ikuta

Submitted to the Department of Aeronautics and Astronautics
on August 23, 1995, in partial fulfillment of the
requirements for the degree of
Master of Science in Aeronautics and Astronautics

Abstract

In this thesis, the feasibility of using blade-mounted servoflap actuation or conventional root pitch (swashplate) actuation to control helicopter vibration is investigated. A linear, time invariant, state space model is derived and presented in a form of frequency response (Bode plot) which is useful for control studies. Multi-blade coordinates are used to transform the blade's degrees of freedom in the rotating frame to the rotor disk modes in the non-rotating frame in order to achieve linear, time invariant system. The linearized model provides general trends of the rotor blade behavior at different flight situations but may not be as accurate at high advance ratio cases.

The model was used to investigate the feasibility of using the servoflap actuation on a one-sixth scale CH-47 model rotor. It is found from the model that as little as 3 deg of servoflap deflection can achieve significant level of vibration reduction. Surprisingly, it is also found that an inboard actuator ($\bar{r}$ = 0.6-0.8) is more effective than an outboard actuator ($\bar{r}$ = 0.8-1.0). The root pitch actuation is found to be less effective than the servoflap actuation, due to a zero introduced in the transfer function at the frequency of interest.

Thesis Supervisor: Steven R. Hall, Sc.D.
Title: Associate Professor of Aeronautics and Astronautics

Acknowledgements

There are many people here at MIT to whom I owe my gratitude for giving freely of their time throughout this project. First of all, I would like to thank my advisor, Professor Steven Hall, for his guidance and support. Boeing Helicpters provided data on the model scale version of the CH-47 rotor, as well as simulation data. I would particulary like to thank Leo Dadone, Bob Derham, and Doug Weems of Boeing Helicopters. Their assistance is greatly appreciated.

I also would like to thank Eric Prechtl, Kyle Yang, and James Garcia for the countless help they provided to answer all my questions. In addition, I would like to acknowledge Dr. BooHo Yang for tutoring me in the fundamentals of control theory and providing me his moral support. I am indebted to all my friends in MIT who made these last two years unforgetable.

Lastly, I would like to thank my brothers, Hirotsugu and Akiyoshi Kuzume, my grandparents, Shun-Ichi and Shizue Ikuta, and off course my parents, Katsuhiko and Hisako Kuzume, for everthing.

Contents

List of Figures

List of Tables

Notation

An attempt was made to use notation as consistent as possible with that of Johnson [11] and Garcia [7]. Dimensionless quantities are normalized by the rotor radius R, the rotation rate Ω, and/or the air density ρ, where possible.

a	blade section lift-curve slope c_{l_α}
$\boldsymbol{a}$	modal amplitude of the generalized mode
A	rotor area, πR^2
$\boldsymbol{A}$	state matrix
A^k	rotor integral, see Appendix A
$\boldsymbol{B}$	state control matrix
B^k	rotor integral, see Appendix A
c	blade chord
$\bar{c}$	normalized blade chord, c/R
$\boldsymbol{C}$	output matrix
C_L	roll moment coefficient, $M_x/\rho AR(\Omega R)^2$
C_M	pitch moment coefficient, $M_y/\rho AR(\Omega R)^2$
C_T	thrust coefficient, $T/\rho A(\Omega R)^2$
C_T/σ	blade loading
C^k	rotor integral, see Appendix A
$\boldsymbol{D}$	output control matrix
D^k	rotor integral, see Appendix A
e	flap hinge offset
$\bar{e}$	normalized flap hinge offset, e/R
E^k	rotor integral, see Appendix A
EI	flapping stiffness
F^k	rotor integral, see Appendix A
$G_{\theta_{r_0}}$	transfer function, $(C_T/\sigma)/\theta_{r_0}$
G_{η_0}	transfer function, $(C_T/\sigma)/\eta_0$
GJ	torsional stiffness
G^k	rotor integral, see Appendix A
h_i	spanwise length of the i th finite element
H^k	rotor integral, see Appendix A
$\boldsymbol{I}$	identity matrix
I_b	characteristic inertia of the rotor blade, $\int_e^R mr^2 dr$

I_{cg} blade sectional inertia

J^k rotor integral, see Appendix A

$\mathbf{K}$ blade stiffness matrix in general

k_θ stiffness of rotor pitch link

K^k rotor integral, see Appendix A

ℓ sectional lift force

$\boldsymbol{L}$ aerodynamic matrices, see Appendix A

$\mathcal{L}$ stiffness matrix for inflow dynamics

L^k rotor integral, see Appendix A

m blade sectional mass

$\mathbf{m}$ sectional moment force

$\mathbf{M}$ blade mass matrix in general

$\boldsymbol{M}$ aerodynamic matrices, see Appendix A

$m^*_{\dot{\theta}_r}$ rotor integral, see Appendix A

$m^*_{\ddot{a}_L}$ rotor integral, see Appendix A

M^k rotor integral, see Appendix A

$\mathcal{M}$ mass matrix for inflow dynamics

n lift coefficient of servoflap, c_{l_η}

$\bar{n}$ normalized lift coefficient of servoflap, c_{l_η}/a

N number of blades

N_e number of elements in finite element model

nm number of modes selected for generalized purpose

p moment coefficient of servoflap, c_{m_η}

$\bar{p}$ normalized moment coefficient of servoflap, c_{m_η}/a

q blade index

q_k eigenvector corresponding to the kth eigenvalue

$\boldsymbol{Q}$ aerodyanmic forcing term

r rotor disk radial coordinate

$\bar{r}$ normalized radial coordinate, r/R

r_1 inboard servoflap location

r_2 outboard servoflap location

r_c root cutout

R rotor radius

s Laplace variable

$\bar{s}$ normalized Laplace variable, $\bar{s}/\Omega$

S^k rotor integral, see Appendix A

t time

T tension due to centripetal force

T^* kinetic coenergy of the rotor blade

$\boldsymbol{u}$ control input vector

$\mathbf{u}$ state vector for finite element analysis

u_P velocity ratio of blade section, normal to disk plane

u_R velocity ratio of blade section, in radial direction

u_T velocity ratio of blade section, parallel to disk plane

U section resultant velocity ratio, $\sqrt{u_T^2 + u_P^2}$

V potential energy of the rotor blade

w spanwise deflection

x rotating blade chordwise coordinate

$\bar{x}$ normalized chordwise coordinate, x/c

x_{cg} center of gravity offset, positive aft of quarter chord

$\boldsymbol{x}$ state vector

$\boldsymbol{y}$ output vector

α blade section angle of attack

α_d rotor disk angle with respect to helicopter velocity

β_i flapping slope of the i th element, positive upward

γ Lock number, $\rho a c R^4 / I_b$

$\boldsymbol{\Gamma}$ aerodynamic hub reaction matrices, see Appendix A

$\boldsymbol{\Delta}$ dynamic matrices, see Appendix A

η servoflap angle

θ blade sectional pitch angle

θ_r blade root pitch angle

λ rotor inflow ratio, $\lambda_f + \lambda_i$

λ_f free stream inflow ratio, $(V \sin \alpha_d + v)/\Omega R$

λ_i induced inflow ratio, $v/\Omega R$

μ rotor advance ratio, $V \cos \alpha_d / \Omega R$

ρ air density

σ rotor solidity $Nc/\pi R$

ϕ section inflow angle, $\tan^{-1}(u_P/u_T)$

ϕ_m^w	m th flapping deflection mode shape
$\phi_m^{w'}$	m th flapping slope mode shape
ϕ_m^θ	m th torsional mode shape
ϕ^{θ_r}	rigid twisting mode shape
Φ	eigenvector matrix used for generalizing purpose
$\boldsymbol{\Phi}$	inertial hub reaction matrices, see Appendix A
ψ	azimuth angle of rotor blade
ψ_q	azimuth angle of q th rotor blade
$\boldsymbol{\Psi}$	dynamic matrices, see Appendix A
ω	frequency [rad/s]
$\bar{\omega}$	nondimensional frequency ω/Ω
ω_k	natural frequency of k th generalized mode
$\bar{\omega}_k$	normalized natural frequency of k th generalized mode, ω_k/Ω
Ω	rotor speed [rad/s]

Subscripts

0	collective
c	longitudinal cyclic
f	free stream
i	induced flow
r	blade root
s	lateral cyclic

Superscripts

$'$	derivative
n	exponent on r, see Appendix A
T	transpose

Chapter 1

Introduction

Helicopter rotors are subjected to periodic aerodynamic forces, especially due to so-called blade vortex interaction (BVI). BVI can cause significant levels of vibration, which reduces pilot effectiveness, passenger comfort, and increases structural weight and maintenance cost. Therefore, reducing vibration is of great interest.

The main cause of BVI is the blade tip vortices created by the spinning rotor. As the rotor spins, these vortices trail and create a nonuniform flow field behind each blade, and the passage of the other blades through the nonuniform flow field causes them to vibrate. As each blade moves around the azimuth, it experiences aerodynamic forcing. The forcing is periodic, so that the blade experiences the same force each time it passes a given azimuthal position. Therefore, the force on each blade can be Fourier decomposed as a sum of sines and cosines, with frequencies at integer multiples of the rotation rate, Ω. The forces experienced by one blade will be the same as the forces experienced by another, except for a change in the phase. When summing up the forces from all the blades, the phase differences cause the forces to cancel, except at multiples of the blade passage frequency, $N\Omega$, where N is the number of blades. Controlling these harmonics is known as higher harmonic control (HHC). Much research effort has been directed to the use of HHC theory, and number of wind-tunnel tests, as well as flight tests, were performed based on the HHC algorithms [19] [22]. For more complete references to HHC techniques, see Reference 9.

There are several ways to reduce vibrations, including the use of a rotor isolation system [3], a floor/fuel isolation system [4], and vibration absorbers [10]. In this thesis, we are concerned with using the rotor itself to control vibrations. There are two ways to actuate the rotor. Most of the HHC literature has assumed root pitch actuation through the swashplate. The other approach is to use some sort of blade-mounted actuation. These two methods are discussed in the sections below.

1.1 Root Pitch Actuation

Conventional helicopter rotors are controlled by a swashplate, located below the hub of the main rotor, which converts pilot controls in the fixed frame to blade pitch angle in the rotating frame. By moving the swashplate through the flight control, the pilot can control the collective thrust, the pitching moment, and the rolling moment of the helicopter rotor. Shaw *et al.* [19] have demonstrated the use of closed-loop HHC on a dynamically scaled model of the three-bladed CH-47D rotor. The controller applied small amounts of oscillatory swashplate motion to produce multi-harmonic blade pitch angle of up to ± 3.0 degrees, and they were able to demonstrate a 90 percent decrease in vibratory shears at the hub. Kottapalli *et al.* [12] have showed similar results using a 4 bladed full scale S-76 rotor.

There are two problems with the use of the swashplate for rotor control. First, in order to achieve HHC, the swashplate must be actuated as fast as $N\Omega$, where a typical value of Ω is 200 RPM. Therefore, actuation must take place at about 10 Hz, and accomplishing that with a swashplate is difficult. Second, the swashplate has only three degrees of freedom. For some applications other than HHC (blade tracking, noise control etc) it is desirable to control each blade individually. It is not possible to control the blades of a rotor with four or more blades individually using only a swashplate.

In order to resolve the problem of the limited degrees of freedom, the conventional swashplate actuation can be substituted with servo actuators for each blade. Use of such actuators makes it possible to apply individual control to any number of rotor

blades. This control strategy is called individual blade control (IBC).

Jacklin and Nguyen[16] have demonstrated the IBC technique on a full scale BO-105 rotor by replacing the rotating pitchlinks at the hub with servo actuators. The effect of up to ± 1.2 deg of open-loop IBC was studied at various speeds, and for some cases 50 to 70 percent of rotor balance forces and moments were suppressed.

One difficulty with direct control of blade root pitch is the weight and complexity of the actuators. Generally, the power density of electric actuators is too low. Hydraulic actuators have higher power densities, but it is impractical to use hydraulics in the rotating frame.

1.2 Blade-Mounted Actuation

Blade-mounted actuation have been developed as another vibration reduction method. The blade-mounted methods include the use of circulation control rotor (CCR) [21] and servoflap control [20] method.

CCR is based on the Coanda Effect, in which tangential air flow from the trailing edge of an elliptically shaped rotor blade delays the boundary layer separation, providing high sectional lift coefficients. HHC can be achieved without moving any parts except the rotating blade itself. However, the mechanical complexity of CCR limits its usage.

Mounting an actuator on a helicopter blade for HHC is not an easy task, due to the limited space within or around each blade and the large centripetal force exerted during normal operations. A helicopter blade is a long thin structure usually built with solid shell and honeycomb fillings. The available space for placing a servoflap is, therefore, limited. Also, during a normal flight, the rotor blades experience a centripetal force on the order of hundreds of g's. These considerations eliminate the use of any type of conventional hydraulic systems.

Spangler and Hall [20] first suggested the use of active materials to actuate a servoflap for rotor control. They proposed using a piezoelectric bimorph bender to actuate a trailing edge flap. Piezoelectric ceramics possess the high bandwidth

necessary for rotor control. Furthermore, they are solid state devices requiring no additional moving parts for operation. Spangler and Hall demonstrated the bender concept in a wind tunnel by incorporating a dynamically scaled actuator into a one fifth model scale CH-47 rotor blade section. Their results showed that blade-mounted actuation is possible, but they ran into problems due to friction and backlash in the flap hinges.

Hall and Prechtl [8] improved on this design, eliminating the friction and backlash problems by replacing the hinges with flexures. In addition, they increased the bender mechanical efficiency by tapering its cross-sectional properties. They conducted a bench test of this actuator and demonstrated flap deflections of ± 11.5 deg under no-load conditions. Their results show that, if properly scaled, this actuator can provide up to ± 5 deg of flap deflection at the 90 percent span location of an operational helicopter in hover. Furthermore, the bandwidth of their actuator went as high as 7/rev in the experiment and, with proper inertial scaling, can be raised to 10/rev.

Piezoelectric ceramics, on the other hand, are heavy and brittle material. Therefore, placing them in such an aggressive environment as a helicopter rotor blade requires much thought to ensure actuator lifetimes. It is not clear that a piezoelectric bender is the best way to actuate a trailing edge flap. Current research at MIT is examining a number of actuator alternatives to achieve the same goal.

1.3 Thesis Goal and Overview

Due to the complex dynamics and aeroelasticity involved in helicopter rotor operations, it is necessary to computationally simulate the rotor dynamics in order to investigate the feasibility of adding the active control system. Developing a simple, linear time invariant model of a helicopter rotor would allow us to observe the trends of the rotor behavior at various flying conditions. Fox [6] has developed a linear, time invariant, state space rotor model using multi-blade coordinates to transform dynamics from the rotating frame to the fixed frame. Garcia's work [7] was the extension of the work done by Fox [6], and this thesis builds on Garcia's work. The goal of

this thesis is to develop a linear time invariant model which incorporates some blade properties which are known to be important for the rotor dynamics but are excluded in Garcia's model. Such properties include the blade elastic bending properties and the blade spanwise center of gravity offset distribution.

Chapter 2 explains the derivation of the state space model of a rotor system with assumptions such as time invariant rotor dynamics and linear aerodynamic forces. Multi-blade coordinates are used to achieve successful transformation from rotating frame dynamics to non-rotating frame dynamics.

Chapter 3 presents results of the linear, time invariant, state space model derived in Chapter 2. The model is validated by comparing certain results with the results obtained by Garcia's [7] state space model. Parametric studies using a one-sixth model scale CH-47 rotor are done by varying properties such as servoflap spanwise location and helicopter forward velocity. The thrust response due to collective root pitch actuation and servoflap actuation are the primary interest, therefore, thrust frequency response due to such actuations are presented and studied in the form of Bode plots.

Chapter 4 presents the summary of the important conclusions, and some suggestions for the possible further research are listed.

Chapter 2

Model Derivation

In this chapter, a linear, time invariant, state space model of a helicopter rotor is developed. A semi-articulated rotor model with elastic flapping and elastic torsion is assumed. The inputs of the state space system are the root pitch angle and servoflap deflection. The outputs are the hub loads, namely, vertical force, pitching moment, and rolling moment. The model is derived by first finding the stiffness and mass matrices of the rotor blade from the blade structural properties using a finite element method. The natural frequencies of the blade flapping and torsion, as well as their mode shapes are simultaneously found. Then, the forces and moments due to aerodynamic forces due to modal deflections are calculated. Modal forces and moments are then transformed from the rotating frame to the fixed frame using multi-blade coordinates (MBC). A dynamic inflow model developed by Pitt and Peters [17] is also added to the dynamics. Finally, these structural dynamics, aerodynamics and inflow dynamics are coupled together to form a state space model of a helicopter rotor which includes root pitch and servoflap actuations. Before the derivation of the state space model, the notation and coordinates of the rotor system is presented.

2.1 Rotor Coordinates

Polar coordinates are used to describe a rotor disk: r for radial position and ψ for azimuth angle. These coordinates are illustrated in Figure 2-1. It is assumed that the

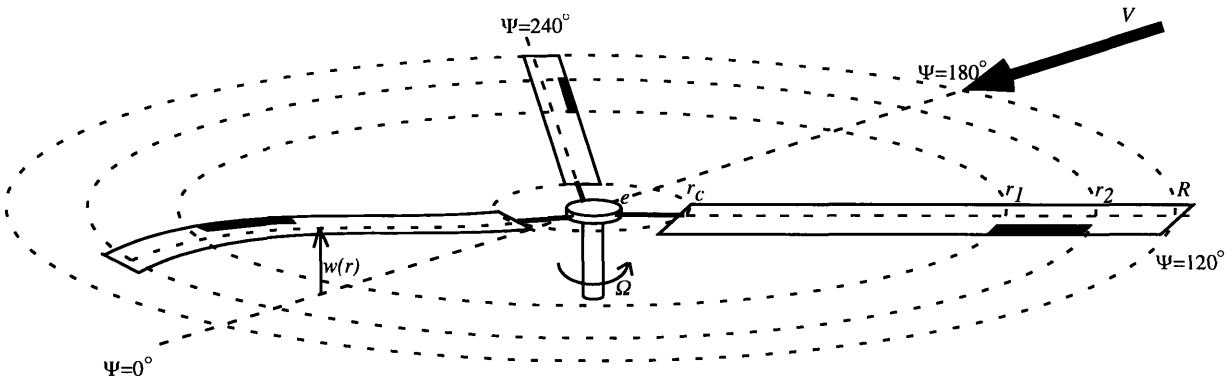

Figure 2-1: Helicopter Rotor Coordinates

rotor rotates counterclockwise if viewed from the top, as is conventional for American helicopters. The rotational velocity is denoted Ω. Each blade flaps elastically about a flapping hinge at $r = e$, and the blade's spanwise flapping displacement from the horizontal plane is denoted $w(r)$. Servoflaps are located between spanwise locations r_1 and r_2 of each blade, and servoflaps are deflected an angle of η, defined positive downward. Each blade is also allowed to twist elastically across the span with an angle θ, defined nose up positive. In order to achieve root pitch actuation, the whole blade is allowed to pitch rigidly with an angle θ_r. For this model, the pitch axis coincides with the neutral axis at the quarter chord. The center of gravity offset is denoted x_{cg} defined aft of quarter chord positive. The sectional coordinate are illustrated in Figure 2-2. For convenience, the normalized radial location is $\bar{r} = r/R$ and the normalized chordwise location is $\bar{x} = x/c$.

2.2 Multi-Blade Coordinates

In this chapter, a linear, time invariant, state space model is derived. A linear, time invariant system allows the use of frequency response as a method for rotor dynamics simulation. Frequency response has not been thought to suite as a method of solution to rotor blade dynamics simulation because rotor blade dynamic forces are periodic

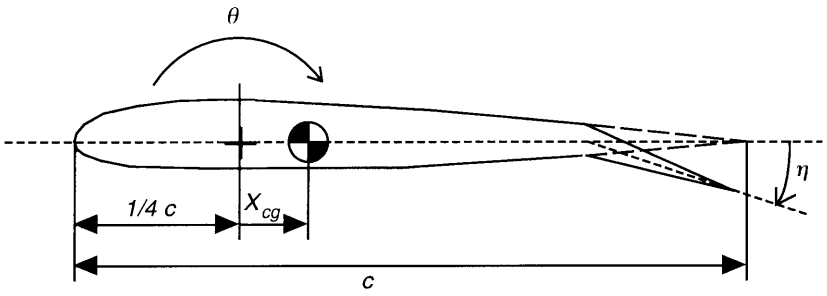

Figure 2-2: Blade Sectional Coordinate

and incorporating periodic effects into frequency response is very complicated. In the previous work such as Shaw [19], $N\Omega$ root pitch actuations were often evaluated in a form of T matrix. T matrix shows the $N\Omega$ cosine and sine output effects due to $N\Omega$ cosine and sine input with varying forward speed. The results of the T matrix, however, often showed only a small influence of periodic effects in the output. Therefore, by neglecting certain periodic terms, linear, time invariant, system of the rotor blade dynamics could be derived, and the frequency response of both root pitch and servoflap actuations can be obtained. Multi-blade coordinates (MBC) are used to transform blade forcing properties from the rotating frame to the non-rotating frame in order to achieve linear, time invariant, system. In Appendix B, the general procedure of using MBC and an example are given. This information is taken from Garcia [7, chapter 2]. A more detailed explanation is available in Johnson [11].

2.3 Finite Element Analysis

In this section, the finite element procedure used to model the blade's elastic motion is described. The finite element model will produce equations of motion of the form

$$\mathbf{M}\ddot{\mathbf{u}} + \mathbf{K}\mathbf{u} = \boldsymbol{Q} \tag{2.1}$$

where $\mathbf{M}$, and $\mathbf{K}$ are the mass and stiffness matrices, respectively, $\mathbf{u}$ is a vector of elastic degrees of freedom, and $\boldsymbol{Q}$ is the forcing term from aerodynamics. In this study,

material damping is ignored, and hence there is no damping term in Equation 2.1. All damping in the model will arise from aerodynamic considerations. The objective of the finite element code developed in this section is to find the stiffness and mass matrices of Equation 2.1, and also find the natural frequencies with the corresponding mode shapes for a given rotor blade. The natural frequencies and the mode shapes are obtained by solving the generalized eigenvalue problem

$$\mathbf{K}q_k = \omega_k^2 \mathbf{M}q_k \tag{2.2}$$

where ω_k is the kth natural frequency and q_k is the corresponding mode shape.

The stiffness and mass matrices can be found by many different techniques. Garcia [7] used a lumped mass model to simulate the blade properties. However, due to the limited number of masses which can be incorporated in a lumped mass model, only the approximated spanwise properties (mass, inertia etc) could be used. The finite element method, on the other hand, can incorporate the blade properties across the span with much higher precision than the lumped mass model since blade properties are usually given in either tabular or graphical format, and are generally piecewise linear. By breaking up a blade into elements appropriately, each element will have all linear properties. Therefore, much more accurate equations of motion can be derived.

The advantage of the finite element method over any other method is that the equations of motion for the system can be derived by first deriving the equations of motion for a typical finite element and then assembling the individual elements' equations of motion to find the over all system's equation of motion.

Figure 2-3 shows a typical rotor blade finite element of arbitrary width, h_i. Let N_e be the number of total number of blade elements. The motion of the system is defined in terms of the displacement, $w_i(t)$, slope, $w_i'(t)$, and torsional displacement, θ_i, of the element end points, where i varies from 1 to $N_e + 1$. The stiffness and mass matrices for each element are found by determining the elastic potential energy, V,

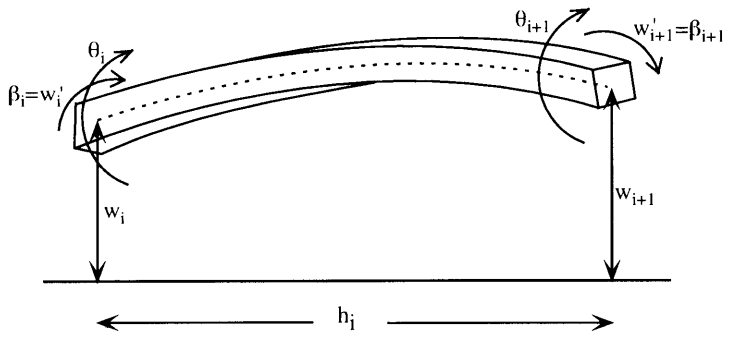

Figure 2-3: Finite element example

and the kinetic energy, T^*, of the element. The potential energy is

$$V = \frac{1}{2}\int_0^{h_i} EI\left(\frac{\partial^2 w}{\partial x^2}\right)^2 dx + \frac{1}{2}\int_0^{h_i} T\left(\frac{\partial w}{\partial x}\right)^2 dx + \frac{1}{2}\int_0^{h_i} GJ\left(\frac{\partial \theta}{\partial x}\right)^2 dx \tag{2.3}$$

and the kinetic energy is

$$T^* = \frac{1}{2}\int_0^{h_i} m\left(\dot{w} - x_{cg}\dot{\theta}\right)^2 dx + \frac{1}{2}\int_0^{h_i} I_{cg}\dot{\theta}^2 dx \ . \tag{2.4}$$

where EI, T, and GJ in Equation 2.3 are the blade spanwise flapping stiffness, the tension due to blade centripetal force, and the twisting torsional stiffness, respectively. I_{cg} is the blade's sectional moment mass of inertia about its center of gravity. The deflections, w and θ, are interpolated between the element end points via

$$\theta(x,t) = L_\theta^T(x) q_\theta(t) \tag{2.5}$$

$$w(x,t) = L_w^T(x) q_w(t). \tag{2.6}$$

where

$$\boldsymbol{L}(x) = \begin{bmatrix} L_\theta(x) \\ L_w(x) \end{bmatrix} = \begin{bmatrix} L_{\theta_1} \\ L_{\theta_2} \\ L_{w_1} \\ L_{w_2} \\ L_{w_3} \\ L_{w_4} \end{bmatrix} = \begin{bmatrix} 1-\tilde{x} \\ \tilde{x} \\ 1-3\tilde{x}^2+2\tilde{x}^3 \\ h\tilde{x}-2h\tilde{x}^2+h\tilde{x}^3 \\ 3\tilde{x}^2-2\tilde{x}^3 \\ -h\tilde{x}^2+h\tilde{x}^3 \end{bmatrix} \tag{2.7}$$

and

$$\boldsymbol{q}(t) = \begin{pmatrix} q_\theta(t) \\ q_w(t) \end{pmatrix} = \begin{pmatrix} \theta_i \\ \theta_{i+1} \\ w_i \\ w_i' \\ w_{i+1} \\ w_{i+1}' \end{pmatrix} \tag{2.8}$$

where $\tilde{x} = x/h_i$. The polynomials in $\boldsymbol{L}$(x) are chosen to satisfy the torsional and bending boundary conditions, which are

$$\begin{array}{cccc} L_{\theta_1}(0) = 1 & & L_{\theta_1}(h_i) = 0 & \\ L_{\theta_2}(h_i) = 0 & & L_{\theta_2}(h_i) = 1 & \\ L_{w_1}(0) = 1 & L'_{w_1}(0) = 0 & L_{w_1}(h_i) = 0 & L'_{w_1}(h_i) = 0 \\ L_{w_2}(0) = 0 & L'_{w_2}(0) = 1 & L_{w_2}(h_i) = 0 & L'_{w_2}(h_i) = 0 \\ L_{w_3}(0) = 0 & L'_{w_3}(0) = 0 & L_{w_3}(h_i) = 1 & L'_{w_3}(h_i) = 0 \\ L_{w_4}(0) = 0 & L'_{w_4}(0) = 0 & L_{w_4}(h_i) = 0 & L'_{w_4}(h_i) = 1 \end{array} \tag{2.9}$$

By substituting Equations 2.5 and 2.6 into Equations 2.3 and 2.4, the potential and kinetic energies become

$$V = \frac{1}{2}\begin{bmatrix} q_\theta^T & q_w^T \end{bmatrix} \int_0^{h_i} \begin{bmatrix} GJ\left(\frac{\partial L_\theta}{\partial x}\right)\left(\frac{\partial L_\theta}{\partial x}\right)^T & 0 \\ 0 & EI\left(\frac{\partial^2 L_w}{\partial x^2}\right)\left(\frac{\partial^2 L_w}{\partial x^2}\right)^T + T\left(\frac{\partial L_w}{\partial x}\right)\left(\frac{\partial L_w}{\partial x}\right)^T \end{bmatrix} dx \begin{bmatrix} q_\theta \\ q_w \end{bmatrix} \tag{2.10}$$

$$T^* = \frac{1}{2}\begin{bmatrix} \dot{q}_\theta^T & \dot{q}_w^T \end{bmatrix} \int_0^{h_i} \begin{bmatrix} mx_{cg}^2 L_\theta L_\theta^T + I_{cg} L_\theta L_\theta^T & mx_{cg} L_\theta L_w^T \\ mx_{cg} L_w L_\theta^T & mL_w L_w^T \end{bmatrix} dx \begin{bmatrix} \dot{q}_\theta \\ \dot{q}_w \end{bmatrix} \tag{2.11}$$

The matrices within each integrals in Equations 2.10 and 2.11 are the stiffness matrix and mass matrix, respectively:

$$K_i = \int_0^{h_i} \begin{bmatrix} GJ\left(\frac{\partial L_\theta}{\partial x}\right)\left(\frac{\partial L_\theta}{\partial x}\right)^T & 0 \\ 0 & EI\left(\frac{\partial^2 L_w}{\partial x^2}\right)\left(\frac{\partial^2 L_w}{\partial x^2}\right)^T + T\left(\frac{\partial L_w}{\partial x}\right)\left(\frac{\partial L_w}{\partial x}\right)^T \end{bmatrix} dx \tag{2.12}$$

$$M_i = \int_0^{h_i} \begin{bmatrix} mx_{cg}^2 L_\theta L_\theta^T + I_{cg} L_\theta L_\theta^T & mx_{cg} L_\theta L_w^T \\ mx_{cg} L_w L_\theta^T & mL_w L_w^T \end{bmatrix} dx \tag{2.13}$$

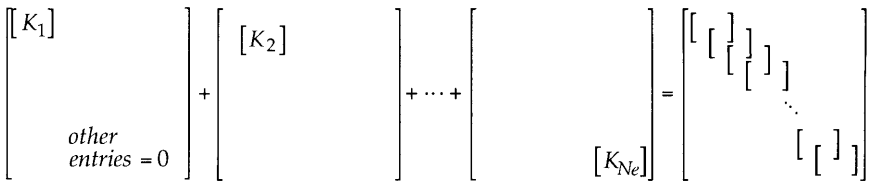

Figure 2-4: Assembly process

The properties in Equations 2.12 and 2.13 such as GJ, EI, T, m, I_{cg}, and x_{cg}, are linear within the element which makes it possible to evaluate the integrals in closed form. The element stiffness and mass matrices are calculated in subroutine `FE_subexact.m`, attached in Appendix D.

Each 6×6 stiffness and mass matrices represent potential and kinetic energies of each element, and by summing the energies of each element appropriately, the potential and kinetic energies of the whole rotor blade can be found in the form of stiffness and mass matrices. Let K_i and M_i be the stiffness and mass matrices of the ith element, and K_w and M_w be the stiffness and mass matrices of the whole rotor blade. Then, summing of energies can be accomplished as shown in Figure 2-4. The stiffness matrix of the whole blade, K_w, is found by placing the 6×6 stiffness matrices from each element diagonally to each other with left upper and/or right lower 3×3 part overlapping to the adjacent matrices. The overlapped parts between the two matrices are the potential energies from the same blade location. Therefore, they are simply added entry by entry. The mass matrix of the whole blade is found the same way. Eventually, both K_w and M_w become $(3N_e + 3) \times (3N_e + 3)$, large where N_e is the number of elements used to model the rotor blade.

The boundary conditions for this rotor blade come from the fact that the flapping deflection and the flapping moment at the flapping hinge are both zero. It is sufficient to satisfy only the geometric boundary condition, $w_1 = 0$, to achieve an accurate model. Therefore, the row and column corresponding to w_1 in K_w and M_w are set to zero and deleted. Finally, to find all the natural frequencies, ω_k, and the corresponding mode shapes, q_k, the eigenvalue problem in Equation 2.2 is solved by using the obtained K_w and M_w.

The eigenvalues represent the combined torsional and flapping natural frequencies of the rotor blade. Each eigenvalue has a corresponding eigenvector, and the eigenvector which contains information of torsional, flapping deflection and flapping slope modes represents the mode shape of the corresponding eigenvalue. Similar to Fourier Series, a motion of a blade can be expressed as a linear combinations of the mode shapes. The coefficient or the amplifying factor for each mode shape is the modal amplitude which is used as the state variable in the state space model derived in this thesis. In Garcia's approach [7], torsional modes and rigid flapping deflection mode were treated separately whereas the present study combines all torsional, flapping deflection and flapping slope modes as just plain modes. One of the advantages of using combined modes is that the necessary number of modal amplitudes for the state space model is much less. Therefore, fewer state variables are needed. Also, modes with coupled torsion and flapping are easily incorporated into the state space model.

One of our objectives for this study is to analyze the effect of rotor blade's root pitch actuation, *i.e.*, swashplate control. In order to do this, there is a need to include a torsional mode which represents pure rigid pitch motion, because the mode shapes obtained from the finite element code have boundary conditions which exclude this rigid pitch mode. Let Φ_0 consist of a vector that represents the rigid pitch mode shape, q_0, and let $\boldsymbol{a}_0$ be the modal amplitude of the rigid pitch mode.

The state vector, $\mathbf{u}$, in Equation 2.1, which consists of the modal amplitudes of all of the eigenvectors, can be simplified and reduced to have a desired number of degrees of freedom by retaining a certain number of modes with lowest frequencies. Let N_m be the desired number of degrees of freedom to be contained in the state space model, then, Φ_L consists of the first N_m columns of eigenvectors, q_i's, and $\boldsymbol{a}_L$ consists of the first N_m modal amplitudes. The simplification can be accomplished by expressing $\mathbf{u}$ as

$$\mathbf{u} = \Phi \boldsymbol{a} \tag{2.14}$$

where

$$\Phi = \begin{bmatrix} \Phi_0 & \Phi_L \end{bmatrix} = \begin{bmatrix} q_0 & q_1 & q_2 & \cdots & q_{N_m} \end{bmatrix} \tag{2.15}$$

and

$$\boldsymbol{a} = \begin{bmatrix} \boldsymbol{a}_0 & \boldsymbol{a}_L \end{bmatrix} = \begin{bmatrix} a_0 & a_1 & a_2 & \cdots & a_{N_m} \end{bmatrix}. \tag{2.16}$$

Substituting Equation 2.14 into Equation 2.1 and multiplying by Φ^T on both sides, the equations of motion can be rewritten as

$$\Phi^T M_w \Phi \ddot{\boldsymbol{a}} + \Phi^T K_w \Phi \boldsymbol{a} = \Phi^T \boldsymbol{Q}. \tag{2.17}$$

Substituting Equation 2.15 and 2.16 into Equation 2.17, the equations of motion can be rewritten as

$$\begin{bmatrix} q_0^T M_w q_0 & q_0^T M_w q_L \\ q_L^T M_w q_0 & q_L^T M_w q_L \end{bmatrix} \begin{Bmatrix} \ddot{a}_0 \\ \ddot{a}_L \end{Bmatrix} + \begin{bmatrix} q_0^T K_w q_0 & q_0^T K_w q_L \\ q_L^T K_w q_0 & q_L^T K_w q_L \end{bmatrix} \begin{Bmatrix} a_0 \\ a_L \end{Bmatrix} = \begin{bmatrix} q_0^T Q \\ q_L^T Q \end{bmatrix}. \tag{2.18}$$

The matrices above may be simplified as

$$\begin{bmatrix} M_{00} & M_{0L} \\ M_{L0} & M_{LL} \end{bmatrix} \begin{Bmatrix} \ddot{a}_0 \\ \ddot{a}_L \end{Bmatrix} + \begin{bmatrix} K_{00} & K_{0L} \\ K_{L0} & K_{LL} \end{bmatrix} \begin{Bmatrix} a_0 \\ a_L \end{Bmatrix} = \begin{bmatrix} Q_0 \\ Q_L \end{bmatrix} \tag{2.19}$$

where subscripts with 0 represents properties of the rigid pitch motion and subscripts with L represents properties of other modes. The terms Q_0 and Q_L represent the aerodynamic forcing terms applied on the rigid pitch mode and the other modes, respectively, and they are derived in the next section. Notice that the original mass and stiffness matrices from Equation 2.1 were $(3N_e + 2) \times (3N_e + 2)$, but the new mass and stiffness matrices in Equation 2.19 are shrunk to $(N_m + 1) \times (N_m + 1)$.

The second row of Equation 2.19 can be rewritten as

$$M_{LL}\ddot{a}_L + K_{LL}a_L = Q_L - M_{L0}\ddot{a}_0 - K_{L0}a_0. \tag{2.20}$$

The term K_{00} in Equation 2.19 is the stiffness associated with the blade's rigid pitch motion, and is therefore zero. In fact, K_{00} is not quite zero, due to propeller moment terms. However, these effects are small, and will be ignored. Since K_{00} is zero and the stiffness matrix is positive definite, K_{L0} and K_{0L} must be zero. In the

finite element code, however, the pitch link stiffness is incorporated into the blade properties, modeled as one end of the pitch link attached to the blade and the other attached to the swashplate. The finite element code allows the movement of the blade's rigid pitch actuation but holds the swashplate rigid. This motion results in stretching and compressing the pitch link as the root pitch actuation is done. Therefore, the stiffness associated with the blade's rigid pitch motion without moving the swashplate is not zero. The actual root pitch actuation is achieved by actuating both the blade and the swashplate, therefore, the stiffness of the pitch link does not affect the stiffness associated with the rigid pitch motion. This is why K_{00} as well as K_{L0} and K_{0L} must all be set to zero.

After setting K_{L0} equal to zero, the modal amplitudes and their time-derivatives in Equation 2.20 are transformed using multi-blade coordinates, and the equations of motion become

$$\boldsymbol{\Delta}_{\ddot{a}}\ddot{\boldsymbol{a}}_L + \boldsymbol{\Delta}_{\dot{a}}\dot{\boldsymbol{a}}_L + \boldsymbol{\Delta}_{a}\boldsymbol{a}_L = \boldsymbol{Q}_L - \boldsymbol{\Psi}_{\ddot{\theta}_r}\ddot{\boldsymbol{a}}_0 - \boldsymbol{\Psi}_{\dot{\theta}_r}\dot{\boldsymbol{a}}_0 - \boldsymbol{\Psi}_{\theta_r}\boldsymbol{a}_0. \tag{2.21}$$

The various Δ and Ψ matrices are defined in Appendix A. In order to complete the derivation, the aerodynamic forcing term, $\boldsymbol{Q}_L$, needs to be evaluated.

2.4 Aerodynamic Model

In this section, aerodynamic forcing term, $\boldsymbol{Q}_L$, in Equation 2.21 is derived. Linear aerodynamic forces are assumed by keeping sectional lift curve slope, c_{l_α}, sectional servoflap lift coefficient, c_{l_η}, and other variables constant spanwise and azimuthally. Torsional aerodynamic damping is also included assuming quasi-steady aerodynamics. Before proceeding with the aerodynamic derivations, nondimensional fixed frame and rotating frame velocity components are explained.

The rotor disk may have an angle of attack, α_d, relative to the helicopter velocity, V. The air velocity relative to the rotor disk can be decomposed into two components, one parallel and one normal to the disk plane. After being nondimensionalized by

the blade tip velocity, ΩR, the parallel velocity component relative to the rotor disk is the advance ratio, μ, defined as

$$\mu = \frac{V \cos \alpha_d}{\Omega R}. \tag{2.22}$$

The normal component of the air velocity is the inflow, λ, which is composed of two parts,

$$\lambda = \lambda_f + \lambda_i \tag{2.23}$$

where λ_f is the inflow due to the free stream velocity, V, defined as

$$\lambda_f = \frac{V \sin \alpha_d}{\Omega R} \tag{2.24}$$

and λ_i is the induced inflow of the rotor.

The airflow relative to the blade due to rotor motions can be decomposed into three terms, namely the tangential velocity, u_T, defined positive toward trailing edge, radial velocity, u_R, defined positive toward blade tip, and normal velocity, u_P, defined positive up through the disk plane. Figure 2-5 illustrates these velocities, nondimensionalized by ΩR. In forward flight, these velocities are

$$u_T = \bar{r} + \mu \sin \psi \tag{2.25}$$

$$u_R = \mu \cos \psi \tag{2.26}$$

$$u_P = \lambda + \mu w' \cos \psi + \dot{w} \tag{2.27}$$

which are the function of azimuth angle, ψ, and radial position, $\bar{r}$.

The aerodynamic components that make up the forcing term, Q_L, in Equation 2.20 are the modal forces due to the airfoil sectional lift and moment. The modal forces are expressed as the sum of the product of a sectional force and the corresponding mode shape over the whole blade. The sectional lift force, with small angle approximation,

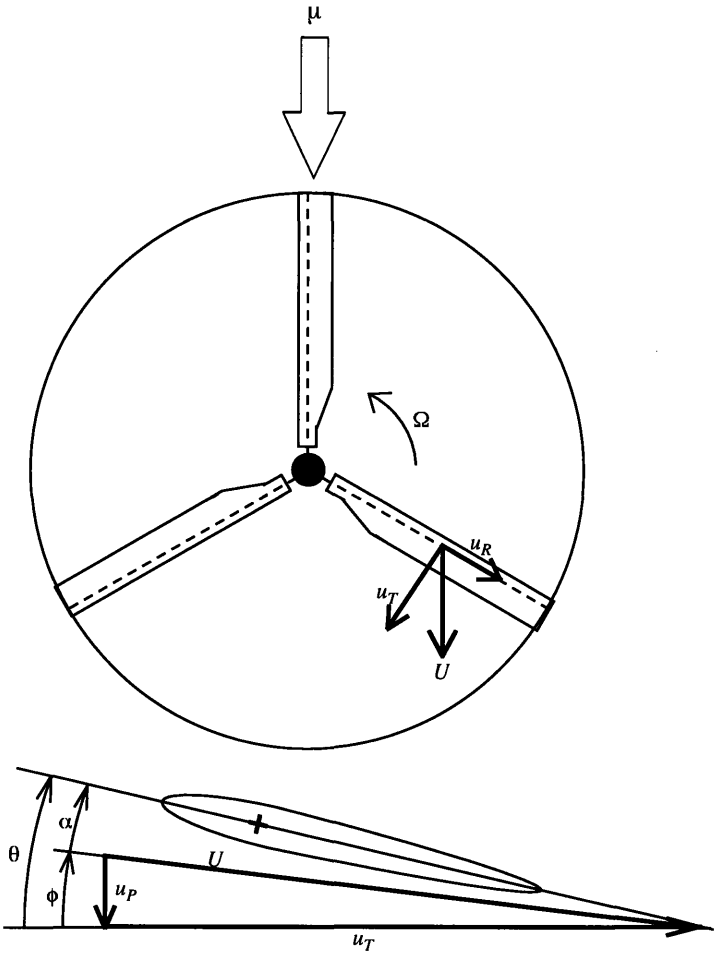

Figure 2-5: Nondimensional velocities

is

$$\ell = \frac{1}{2}\rho c u_T^2 \left(\Omega R\right)^2 c_l \tag{2.28}$$

$$= \frac{1}{2}\rho c u_T^2 \left(\Omega R\right)^2 \left(a\alpha + n\eta\right) \tag{2.29}$$

where the sectional lift coefficient, c_l, is approximated as a linear combination of angle of attack, α, and servoflap deflection angle, η. The sectional lift curve slope, a and

the sectional servoflap lift coefficient, n, are

$$a = c_{l_\alpha} \tag{2.30}$$

$$n = c_{l_\eta}. \tag{2.31}$$

The sectional moment force is

$$\mathbf{m} = \frac{1}{2}\rho c^2 u_T^2 \left(\Omega R\right)^2 \left(p\eta\right) \tag{2.32}$$

where the moment is also assumed to be linear to servoflap deflection, and the sectional servoflap moment coefficient, p, is

$$p = c_{m_\eta}. \tag{2.33}$$

The airfoil coefficients, a, n, and p are obtained from the 2-dimensional panel code, XFOIL [5], which includes viscous and compressibility effects.

Due to the three-dimensional flow effects, there must be a finite distance near the blade tip to drop blade loading to zero. This so-called *tip-loss* effect is approximated by assuming the blade loading farther outboard of radial station $\bar{r} = B$ to be zero. Typical values for B range from 0.96 to 0.98. Therefore, spanwise aerodynamic integrations are carried out from the root cutout, $\bar{r}_c$, to B.

The modal force due to lift, $\boldsymbol{L}$, is obtained by integrating the sectional lift, ℓ, over the corresponding mode shapes. Normalizing $\boldsymbol{L}$ by $I_b\Omega^2$ gives

$$\overline{\boldsymbol{L}}_m = \frac{\gamma}{2}\int_{\bar{r}_c}^{B} u_T^2 \alpha \phi_m^w\left(\bar{r}\right) d\bar{r} + \frac{\gamma}{2}\int_{\bar{r}_1}^{\bar{r}_2} u_T^2 \bar{n}\eta\phi_m^w\left(\bar{r}\right) d\bar{r} \tag{2.34}$$

where the subscript, m, indicates the mth mode shape. The mth flapping and torsional mode shapes are expressed as $\phi_m^w\left(\bar{r}\right)$ and $\phi_m^\theta\left(\bar{r}\right)$, respectively. The angle of attack, α, can be expressed as

$$\alpha\left(\bar{r}\right) = \theta_r + \theta - \frac{u_P}{u_T} \tag{2.35}$$

$$= \theta_r + \theta - \frac{1}{u_T}\left(\lambda + \mu w' \cos\psi + \dot{w}\right). \tag{2.36}$$

Therefore, the modal force can be decomposed into the sum of several terms:

$$\overline{\boldsymbol{L}} = \overline{L}_{\theta_r} + \overline{L}_{\theta} + \overline{L}_{\lambda} + \overline{L}_{w'} + \overline{L}_{\dot{w}} + \overline{L}_{\eta} \tag{2.37}$$

where

$$\overline{L}_{\theta_{rm}} = \frac{\gamma}{2}\int_{\bar{r}_c}^{B} u_T^2 \phi_m^w(\bar{r})\,\phi^{\theta_r}(\bar{r})\,d\bar{r}\;\boldsymbol{a}_0 \tag{2.38}$$

$$\overline{L}_{\theta_{mn}} = \frac{\gamma}{2}\int_{\bar{r}_c}^{B} u_T^2 \phi_n^{\theta}(\bar{r})\,\phi_m^w(\bar{r})\;\,d\bar{r}\;\boldsymbol{a}_{L_n} \tag{2.39}$$

$$\overline{L}_{\lambda_m} = -\frac{\gamma}{2}\int_{\bar{r}_c}^{B} u_T \phi_m^w(\bar{r})\;\,d\bar{r}\;\lambda \tag{2.40}$$

$$\overline{L}_{w'_{mn}} = -\frac{\gamma}{2}\int_{\bar{r}_c}^{B} u_T \mu\cos\psi\,\phi_n^{w'}(\bar{r})\,\phi_m^w(\bar{r})\;\,d\bar{r}\;\boldsymbol{a}_{L_n} \tag{2.41}$$

$$\overline{L}_{\dot{w}_{mn}} = -\frac{\gamma}{2}\int_{\bar{r}_c}^{B} u_T \phi_n^w(\bar{r})\,\phi_m^w(\bar{r})\;\,d\bar{r}\;\dot{\boldsymbol{a}}_{L_n} \tag{2.42}$$

$$\overline{L}_{\eta_m} = \frac{\gamma}{2}\int_{\bar{r}_1}^{\bar{r}_2} \bar{n} u_T^2 \phi_m^w(\bar{r})\;\,d\bar{r}\;\eta. \tag{2.43}$$

Notice that blade deflection, w, slope, w', and torsional angle, θ are substituted with the corresponding products of mode shapes and modal amplitudes. Inserting the linear inflow approximation of Equation 2.55, the tangential velocity of Equation 2.25, and the rotor integrals of Appendix A, the modal force components can be rewritten as

$$\overline{L}_{\theta_{rm}} = \left[S_m^2 + 2\mu\sin\psi S_m^1 + \mu^2\sin^2\psi S_m^0\right]\boldsymbol{a}_0 \tag{2.44}$$

$$\overline{L}_{\theta_{mn}} = \left[A_{mn}^2 + 2\mu\sin\psi A_{mn}^1 + \mu^2\sin^2\psi A_{mn}^0\right]\boldsymbol{a}_{L_n} \tag{2.45}$$

$$\begin{aligned}\overline{L}_{\lambda_m} = &-\left[D_m^1 + \mu\sin\psi D_m^0\right]\lambda_0 - \\ &\left[D_m^2 + \mu\sin\psi D_m^1\right](\lambda_c\cos\psi + \lambda_s\sin\psi)\end{aligned} \tag{2.46}$$

$$\overline{L}_{w'_{mn}} = \left[\mu\cos\psi B_{mn}^1 + \frac{1}{2}\mu^2\sin 2\psi B_{mn}^0\right]\boldsymbol{a}_{L_n} \tag{2.47}$$

$$\overline{L}_{\dot{w}_{mn}} = \left[C_{mn}^1 + \mu\sin\psi C_{mn}^0\right]\dot{\boldsymbol{a}}_{L_n} \tag{2.48}$$

$$\overline{L}_{\eta_m} = \left[E_m^2 + 2\mu\sin\psi E_m^1 + \mu^2\sin^2\psi E_m^0\right]\eta. \tag{2.49}$$

The modal force due to moment, $\boldsymbol{M}$, is obtained by integrating the sectional moment, $\mathbf{m}$, over the corresponding mode shapes. Normalizing $\boldsymbol{M}$ by $I_b\Omega^2$ gives

$$\overline{\boldsymbol{M}}_m = \frac{\gamma}{2}\int_{\bar{r}_1}^{\bar{r}_2} \bar{p}\bar{c}u_T^2\phi_m^\theta(\bar{r})\ d\bar{r}\ \eta - \gamma\int_{\bar{r}_c}^{B}\frac{\bar{c}^2}{16}u_T\phi_n^\theta(\bar{r})\,\phi_m^\theta(\bar{r})\ d\bar{r}\ \dot{\boldsymbol{a}}_{L_m} - \gamma\int_{\bar{r}_c}^{B}\frac{\bar{c}^2}{16}u_T\phi^{\theta_r}(\bar{r})\,\phi_m^\theta(\bar{r})\ d\bar{r}\ \dot{\boldsymbol{a}}_0 \tag{2.50}$$

where the first term, which will be denoted $\overline{M}_{\eta_m}$, is the moment modal force on mth modal shape due to servoflap deflection, and the last two terms, $\overline{M}_{\dot{\theta}_m}$ and $\overline{M}_{\dot{\theta}_{r_m}}$, are the elastic and the root pitch torsional aerodynamic damping terms if quasi-steady aerodynamics are assumed [2]. The term $\phi^{\theta_r}(\bar{r})$ is the mode shape for rigid pitch motion. Substituting the tangential velocity Equation 2.25, and the rotor integrals of Appendix A, the components of the modal force due to moment can be rewritten as

$$\overline{M}_{\eta_m} = \left[L_m^2 + 2\mu\sin\psi L_m^1 + \mu^2\sin^2\psi L_m^0\right]\eta \tag{2.51}$$

$$\overline{M}_{\dot{\theta}_{mn}} = \left[M_{mn}^1 + \mu\sin\psi M_{mn}^0\right]\dot{\boldsymbol{a}}_{L_n} \tag{2.52}$$

$$\overline{M}_{\dot{\theta}_{r_m}} = \left[N_m^1 + \mu\sin\psi N_m^0\right]\dot{\boldsymbol{a}}_0. \tag{2.53}$$

Combining modal forces due to lift and moment and transforming them to MBC, the forcing term, Q_L, in Equation 2.21 becomes

$$\boldsymbol{Q}_L = (\boldsymbol{L}_a + \boldsymbol{M}_a)\,\boldsymbol{a}_L + (\boldsymbol{L}_{\dot{a}} + \boldsymbol{M}_{\dot{a}})\,\dot{\boldsymbol{a}}_L + (\boldsymbol{L}_{\theta_r} + \boldsymbol{M}_{\theta_r})\,\boldsymbol{a}_0 + \boldsymbol{M}_{\dot{\theta}_r}\dot{\boldsymbol{a}}_0 + (\boldsymbol{L}_\eta + \boldsymbol{M}_\eta)\,\boldsymbol{\eta} + \boldsymbol{L}_\lambda\boldsymbol{\lambda} \tag{2.54}$$

where the $\boldsymbol{L}$ and $\boldsymbol{M}$ terms are given in Appendix A.

2.5 Inflow Dynamics

Unlike the fixed wing case, helicopter rotor in forward flight creates very complicated inflow dynamics. The shed wake and trailing vorticities produced by the rotating airfoil creates a skewed helical wake which influences the inflow at the rotor disk, so

that the induced inflow is a complicated function of radius and azimuth. However, a simple linear approximation developed by Pitt and Peters [17] can provide adequate results. The linear inflow approximation

$$\lambda = \lambda_0 + \lambda_c \bar{r} \cos\psi + \lambda_s \bar{r} \sin\psi \tag{2.55}$$

is used for the purpose of this research which is based on the actuator disk theory. Simple dynamics relate the λ perturbations to the aerodynamic loads, namely thrust coefficient, C_T, pitch moment coefficient, C_M, and roll moment coefficient, C_L. Defining the vectors

$$\boldsymbol{y}_{\text{aero}} = \left\{ \begin{array}{c} C_T \\ C_M \\ C_L \end{array} \right\}_{\text{aero}}, \quad \boldsymbol{\lambda} = \left\{ \begin{array}{c} \lambda_0 \\ \lambda_c \\ \lambda_s \end{array} \right\}, \tag{2.56}$$

the inflow dynamics presented by Pitt and Peters [17] and used in this research are

$$\dot{\boldsymbol{\lambda}} = -\boldsymbol{\mathcal{M}}_{\lambda}^{-1} \boldsymbol{\mathcal{L}}_{\lambda}^{-1} \boldsymbol{\lambda} + \boldsymbol{\mathcal{M}}_{\lambda}^{-1} \boldsymbol{y}_{\text{aero}} \tag{2.57}$$

which can easily be incorporated into the state space model. The inflow dynamics matrices, $\boldsymbol{\mathcal{M}}_{\lambda}$ and $\boldsymbol{\mathcal{L}}_{\lambda}$, are given in Appendix C.

2.6 Hub Reactions

In the rotating frame, the vertical shear force due to the aerodynamic force minus the inertial force is the applied loading on each blade. These forces can be transformed to non-rotating frame by the MBC transformation, and our nondimensional hub reactions of interests which are the thrust, pitch moment, and roll moment coefficients, or C_T, C_M, and C_L, can be found.

The output of interest has two terms,

$$\left\{ \begin{array}{c} C_T \\ C_M \\ C_L \end{array} \right\} = \left\{ \begin{array}{c} C_T \\ C_M \\ C_L \end{array} \right\}_{\text{aero}} + \left\{ \begin{array}{c} C_T \\ C_M \\ C_L \end{array} \right\}_{\text{inertial}} \tag{2.58}$$

where the aerodynamic term is the shear force and it is needed to force the inflow dynamics. The vertical shear force at the blade root, S, is the integral of the vertical force acting along the blade. This vertical force is composed of sectional lifting force acting upward and the sectional inertial force acting downward. The resultant forces are normalized by $\rho A\left(\Omega R\right)^2$, and they are

$$\begin{aligned}\bar{S} = \frac{\sigma a}{N}\int_{\bar{r}_c}^{B}\frac{1}{2}u_T^2\alpha\ d\bar{r} + \frac{\sigma a}{N}\int_{\bar{r}_1}^{\bar{r}_2}\frac{1}{2}\bar{n}u_T^2\eta\ d\bar{r} - \frac{\sigma aR}{N\gamma I_b}\int_{r_e}^{R}m\ddot{w}\left(r\right)\ dr \\ + \frac{\sigma aR}{N\gamma I_b}\int_{r_e}^{R}mx_{cg}\ddot{\theta}\ dr + \frac{\sigma aR}{N\gamma I_b}\int_{r_e}^{R}mx_{cg}\ddot{\theta}_r\ dr\end{aligned} \tag{2.59}$$

where angle of attack, α, is defined in Equation 2.36. The vertical shear force may be rewritten as

$$\bar{S} = \bar{S}_{\theta_r} + \bar{S}_{\theta} + \bar{S}_{\lambda} + \bar{S}_{w'} + \bar{S}_{\dot{w}} + \bar{S}_{\eta} + \bar{S}_{\ddot{w}} + \bar{S}_{\ddot{\theta}_r} + \bar{S}_{\ddot{\theta}}. \tag{2.60}$$

The first six terms are the aerodynamic terms and the last three are the inertial terms.

Using terms in Appendix A, each normalized vertical shear force may be rewritten as

$$\bar{S}_{\theta_r} = \frac{1}{2N}\left[F^2 + 2\mu\sin\psi F^1 + \mu^2\sin^2\psi F^0\right]\boldsymbol{a}_0 \tag{2.61}$$

$$\bar{S}_{\theta_m} = \frac{1}{2N}\left[G_m^2 + 2\mu\sin\psi G_m^1 + \mu^2\sin^2\psi G_m^0\right]\boldsymbol{a}_{L_m} \tag{2.62}$$

$$\begin{aligned}\bar{S}_{\lambda} = -\frac{1}{2N}\left[F^1 + \mu\sin\psi F^0\right]\lambda_0 \\ - \frac{1}{2N}\left[F^2 + \mu\sin\psi F^1\right]\left(\lambda_c\cos\psi + \lambda_s\sin\psi\right)\end{aligned} \tag{2.63}$$

$$\bar{S}_{w'_m} = \frac{1}{2N}\left[\mu\cos\psi H_m^1 + \frac{1}{2}\mu^2\sin 2\psi H_m^0\right]\boldsymbol{a}_{L_m} \tag{2.64}$$

$$\bar{S}_{\dot{w}_m} = \frac{1}{2N}\left[J_m^1 + \mu\sin\psi J_m^0\right]\dot{\boldsymbol{a}}_{L_m} \tag{2.65}$$

$$\bar{S}_{\eta} = \frac{1}{2N}\left[K^2 + 2\mu\sin\psi K^1 + \mu^2\sin^2\psi K^0\right]\eta \tag{2.66}$$

$$\bar{S}_{\ddot{\theta}_r} = \frac{1}{N}m^*_{\ddot{\theta}_r}\ddot{\boldsymbol{a}}_0 \tag{2.67}$$

$$\bar{S}_{\ddot{a}_{Lm}} = \frac{1}{N}m^*_{\ddot{a}_{Lm}}\ddot{\boldsymbol{a}}_{L_m}. \tag{2.68}$$

Summing over N blades, the rotor thrust coefficient is given by

$$C_T = \sum_{q=1}^{N} \left(\bar{S}_{\theta_r} + \bar{S}_{\theta} + \bar{S}_{\lambda} + \bar{S}_{w'} + \bar{S}_{\dot{w}} + \bar{S}_{\eta} + \bar{S}_{\ddot{\theta}_r} + \bar{S}_{\ddot{a}_L} \right). \tag{2.69}$$

which is equivalent to doing the MBC collective summation operator. The nondimensional moment due to the qth blade is

$$C_{M_q} = \frac{eS}{\rho AR\left(\Omega R\right)^2} \tag{2.70}$$

or

$$C_{M_q} = \bar{e} \left(\bar{S}_{\theta_r} + \bar{S}_{\theta} + \bar{S}_{\lambda} + \bar{S}_{w'} + \bar{S}_{\dot{w}} + \bar{S}_{\eta} + \bar{S}_{\ddot{\theta}_r} + \bar{S}_{\ddot{a}_L} \right). \tag{2.71}$$

By summing the contributions of all the blades, pitch and roll moment coefficients are

$$C_M = \sum_{q=1}^{N} \left(-C_{M_q} \cos\psi_q \right) \tag{2.72}$$

$$C_L = \sum_{q=1}^{N} \left(C_{M_q} \sin\psi_q \right) \tag{2.73}$$

which are similar in the form to the MBC cyclic summation operators.

The partial hub reactions due to the aerodynamic effects only and the total hub reactions are

$$\left\{ \begin{array}{c} C_T \\ C_M \\ C_L \end{array} \right\}_{\text{aero}} = \boldsymbol{\Gamma}_a \boldsymbol{a}_L + \boldsymbol{\Gamma}_{\dot{a}} \dot{\boldsymbol{a}}_L + \boldsymbol{\Gamma}_{\lambda} \boldsymbol{\lambda} + \boldsymbol{\Gamma}_{\theta_r} \boldsymbol{a}_0 + \boldsymbol{\Gamma}_{\eta} \boldsymbol{\eta} \tag{2.74}$$

$$\begin{aligned} \left\{ \begin{array}{c} C_T \\ C_M \\ C_L \end{array} \right\} &= \left(\boldsymbol{\Gamma}_a + \boldsymbol{\Phi}_a \right) \boldsymbol{a}_L + \left(\boldsymbol{\Gamma}_{\dot{a}} + \boldsymbol{\Phi}_{\dot{a}} \right) \dot{\boldsymbol{a}}_L + \boldsymbol{\Phi}_{\ddot{a}} \ddot{\boldsymbol{a}}_L \\ &\quad + \left(\boldsymbol{\Gamma}_{\theta_r} + \boldsymbol{\Phi}_{\theta_r} \right) \boldsymbol{a}_0 + \boldsymbol{\Phi}_{\dot{\theta}_r} \dot{\boldsymbol{a}}_0 + \boldsymbol{\Phi}_{\ddot{\theta}_r} \ddot{\boldsymbol{a}}_0 + \boldsymbol{\Gamma}_{\lambda} \boldsymbol{\lambda} + \boldsymbol{\Gamma}_{\eta} \boldsymbol{\eta} \end{aligned} \tag{2.75}$$

where the Γ and Φ matrices are defined in Appendix A.

2.7 State Space Model

Using the dynamic equations of motions defined in Equations 2.21 and 2.54 with the hub reaction Equations 2.74 and 2.75, a linear, time invariant, state space representation of a rotor with blade-mounted servoflaps can be assembled. The model is

$$\dot{\boldsymbol{x}} = \boldsymbol{A}\boldsymbol{x} + \boldsymbol{B}\boldsymbol{u} + \boldsymbol{B}_\lambda \boldsymbol{y}_{\text{aero}}, \tag{2.76}$$

$$\boldsymbol{y}_{\text{aero}} = \boldsymbol{C}_{\text{aero}}\boldsymbol{x} + \boldsymbol{D}_{\text{aero}}\boldsymbol{u}, \tag{2.77}$$

$$\boldsymbol{y} = \boldsymbol{C}\boldsymbol{x} + \boldsymbol{D}\boldsymbol{u} \tag{2.78}$$

where the state and control vectors, $\boldsymbol{x}$ and $\boldsymbol{u}$, are defined as

$$\boldsymbol{x} = \begin{Bmatrix} \boldsymbol{a}_L \\ \dot{\boldsymbol{a}}_L \\ \boldsymbol{\lambda} \\ \boldsymbol{a}_0 \\ \dot{\boldsymbol{a}}_0 \end{Bmatrix}, \quad \boldsymbol{u} = \begin{Bmatrix} \ddot{\boldsymbol{a}}_0 \\ \boldsymbol{\eta} \end{Bmatrix}. \tag{2.79}$$

The output vectors, $\boldsymbol{y}_{\text{aero}}$ and $\boldsymbol{y}$, are defined as

$$\boldsymbol{y}_{\text{aero}} = \begin{Bmatrix} \boldsymbol{C}_T \\ \boldsymbol{C}_M \\ \boldsymbol{C}_L \end{Bmatrix}_{\text{aero}}, \quad \boldsymbol{y} = \begin{Bmatrix} \boldsymbol{C}_T \\ \boldsymbol{C}_M \\ \boldsymbol{C}_L \end{Bmatrix}. \tag{2.80}$$

The state space matrices are

$$\boldsymbol{A} = \begin{bmatrix} 0 & \boldsymbol{I} & 0 & 0 & 0 \\ a_{21} & a_{22} & a_{23} & a_{24} & a_{25} \\ 0 & 0 & -\boldsymbol{\mathcal{M}}_\lambda^{-1}\boldsymbol{\mathcal{L}}_\lambda^{-1} & 0 & 0 \\ 0 & 0 & 0 & 0 & \boldsymbol{I} \\ 0 & 0 & 0 & 0 & 0 \end{bmatrix} \tag{2.81}$$

where

$$
\begin{aligned}
a_{21} &= \boldsymbol{\Delta}_{\ddot{a}}^{-1}\left(\boldsymbol{L}_a + \boldsymbol{M}_a - \boldsymbol{\Delta}_a\right) \\
a_{22} &= \boldsymbol{\Delta}_{\ddot{a}}^{-1}\left(\boldsymbol{L}_{\dot{a}} + \boldsymbol{M}_{\dot{a}} - \boldsymbol{\Delta}_{\dot{a}}\right) \\
a_{23} &= \boldsymbol{\Delta}_{\ddot{a}}^{-1}\boldsymbol{L}_\lambda \\
a_{24} &= \boldsymbol{\Delta}_{\ddot{a}}^{-1}\left(\boldsymbol{L}_{\theta_r} + M_{\theta_r} - \Psi_{\theta_r}\right) \\
a_{25} &= \boldsymbol{\Delta}_{\ddot{a}}^{-1}\left(\boldsymbol{M}_{\dot{\theta}_r} - \Psi_{\dot{\theta}_r}\right),
\end{aligned}
$$

$$
\boldsymbol{B} = \begin{bmatrix} 0 & 0 \\ -\boldsymbol{\Delta}_{\ddot{a}}^{-1}\boldsymbol{\Psi}_{\ddot{\theta}_r} & \boldsymbol{\Delta}_{\ddot{a}}^{-1}\left(\boldsymbol{L}_\eta + \boldsymbol{M}_\eta\right) \\ 0 & 0 \\ 0 & 0 \\ \boldsymbol{I} & 0 \end{bmatrix} \tag{2.82}
$$

$$
\boldsymbol{B}_\lambda = \begin{bmatrix} 0 \\ 0 \\ \boldsymbol{\mathcal{M}}_\lambda^{-1} \\ 0 \\ 0 \end{bmatrix} \tag{2.83}
$$

$$
\boldsymbol{C}_{\text{aero}} = \begin{bmatrix} \boldsymbol{\Gamma}_a & \boldsymbol{\Gamma}_{\dot{a}} & \boldsymbol{\Gamma}_\lambda & \boldsymbol{\Gamma}_{\theta_r} & 0 \end{bmatrix} \tag{2.84}
$$

$$
\boldsymbol{D}_{\text{aero}} = \begin{bmatrix} 0 & \boldsymbol{\Gamma}_\eta \end{bmatrix} \tag{2.85}
$$

$$
\boldsymbol{C} = \begin{bmatrix} c_1 & c_2 & c_3 & c_4 & c_5 \end{bmatrix} \tag{2.86}
$$

where

$$
\begin{aligned}
c_1 &= \boldsymbol{\Gamma}_a + \boldsymbol{\Phi}_a + \boldsymbol{\Phi}_{\ddot{a}}\boldsymbol{\Delta}_{\ddot{a}}^{-1}\left(\boldsymbol{L}_a + \boldsymbol{M}_a - \boldsymbol{\Delta}_a\right) \\
c_2 &= \boldsymbol{\Gamma}_{\dot{a}} + \boldsymbol{\Phi}_{\dot{a}} + \boldsymbol{\Phi}_{\ddot{a}}\boldsymbol{\Delta}_{\ddot{a}}^{-1}\left(\boldsymbol{L}_{\dot{a}} + \boldsymbol{M}_{\dot{a}} - \boldsymbol{\Delta}_{\dot{a}}\right) \\
c_3 &= \boldsymbol{\Gamma}_\lambda + \boldsymbol{\Phi}_{\ddot{a}}\boldsymbol{\Delta}_{\ddot{a}}^{-1}\boldsymbol{L}_\lambda \\
c_4 &= \boldsymbol{\Gamma}_{\theta_r} + \boldsymbol{\Phi}_{\theta_r} + \boldsymbol{\Phi}_{\ddot{a}}\boldsymbol{\Delta}_{\ddot{a}}^{-1}\left(\boldsymbol{L}_{\theta_r} + \boldsymbol{M}_{\theta_r} - \boldsymbol{\Psi}_{\theta_r}\right)
\end{aligned}
$$

$$c_5 = \boldsymbol{\Phi}_{\dot{\theta}_r} + \boldsymbol{\Phi}_{\ddot{a}} \boldsymbol{\Delta}_{\ddot{a}}^{-1} \left(\boldsymbol{M}_{\dot{\theta}_r} - \boldsymbol{\Psi}_{\dot{\theta}_r} \right)$$

$$\boldsymbol{D} = \left[\begin{array}{cc} \boldsymbol{\Phi}_{\ddot{\theta}_r} & \boldsymbol{\Gamma}_\eta \end{array} \right] + \boldsymbol{\Phi}_{\ddot{a}} \left[\begin{array}{cc} -\boldsymbol{\Delta}_{\ddot{a}}^{-1} \boldsymbol{\Psi}_{\ddot{\theta}_r} & \boldsymbol{\Delta}_{\ddot{a}}^{-1} \left(\boldsymbol{L}_\eta + \boldsymbol{M}_\eta \right) \end{array} \right]. \tag{2.87}$$

Combining Equations 2.76 and 2.77, the dynamic inflow loop can be closed yielding the state space model

$$\dot{\boldsymbol{x}} = \left(\boldsymbol{A} + \boldsymbol{B}_\lambda \boldsymbol{C}_{\text{aero}} \right) \boldsymbol{x} + \left(\boldsymbol{B} + \boldsymbol{B}_\lambda \boldsymbol{D}_{\text{aero}} \right) \boldsymbol{u}, \tag{2.88}$$

$$\boldsymbol{y} = \boldsymbol{C}\boldsymbol{x} + \boldsymbol{D}\boldsymbol{u}. \tag{2.89}$$

Chapter 3

Results and Analysis

In this chapter, the notations and definitions of the input and output for the state space model developed in the previous chapter are discussed. Then, the accuracy of the state space model is verified by comparing results with Garcia's results [7]. After validating the model, the behavior of a model scale CH-47 rotor is evaluated by varying parameters such as forward flight speed and servoflap location. The objectives of this parameter studies are to observe the trend of the rotor response to forward flight speed, and estimate the optimal servoflap location

3.1 Input and Output Definitions

In the previous chapter, a linear, time invariant, state space model was developed. The model is capable of simulating both root pitch and servoflap rotor actuations. This model has six inputs, namely collective and two cyclics each for root pitch and servoflap actuations. There are three outputs, namely coefficient of thrust, pitching moment, and rolling moment. Hence, the state space model yields 18 individual transfer functions. Of these, we are mainly interested two, the effect of collective root pitch and servoflap actuations on thrust coefficient. The transfer function from collective root pitch to thrust, $(C_T/\sigma)/\theta_{r_0}$, is denoted by $G_{\theta_{r_0}}(\bar{s})$. Similarly the transfer function from servoflap deflection to thrust is $(C_T/\sigma)/\eta_0$, which is denoted by $G_{\eta_0}(\bar{s})$. $\bar{s}$ is the Laplace operator normalized by Ω. In order to achieve $G_{\theta_{r_0}}(\bar{s})$ from the state

space model, the transfer function for collective root pitch acceleration, $(C_T/\sigma)/\ddot{\theta}_{r_0}$, must be integrated twice, so that

$$G_{\theta_r}(\bar{s}) = \bar{s}^2 \frac{C_T/\sigma}{\ddot{\theta}_{r_0}} = \frac{C_T/\sigma}{\theta_{r_0}}. \tag{3.1}$$

The nominal value of C_T/σ is approximately equivalent to 1 g of thrust, so that $(\Delta C_T/\sigma)/(C_T/\sigma)$ is a measure of control authority in g's. For this study, C_T/σ of 0.1 is assumed, and the control loads required for 0.1 g of higher harmonic control authority is evaluated. The magnitude plots of all $G_{\theta_{r_0}}(j\bar{\omega})$ and $G_{\eta_0}(j\bar{\omega})$ presented in this chapter are measured in units of deg^{-1} to determine the amount of authority per deg of root pitch or servo-flap deflection.

In a higher harmonic control system for vibration reduction, the control effort is concentrated around $N\Omega$, so for the H-34 rotor the frequencies near 4Ω are of interest. Later, for the model CH-47 rotor, the frequencies of interest are near 3Ω.

Table 3.1 lists all the baseline parameters for both H-34 rotor blade and model size CH-47 rotor blade used for this analysis. In this study the size of the servoflap is set to 20 percent chord length wide and 20 percent long spanwise. The detailed blade properties are given in the MATLAB input code listed in Appendix D of this thesis.

3.2 Model Verification

As previously stated, the state space model derived in the previous chapter is verified by comparing with Garcia's results [7]. Garcia used Boeing Helicopters' rotor analysis program, C60, for validation of his state space model. In this thesis, some verification of the model was done by comparing it to the model of Garcia. Garcia's model includes torsional bending modes and rigid flapping mode, but does not include any elastic flapping modes. By scaling the flapping stiffness, EI, six orders of magnitude higher from its original value in the present model, a blade with rigid flapping and elastic torsion can be simulated and compared to Garcia's model. In addition, later in this chapter, some results with elastic flapping were compared to simulations run by

Table 3.1: Baseline Parameters for H-34 and model CH-47 rotors

Property	Variable	H-34	Model CH-47
number of blades	N	4	3
radius of rotor	R	28 ft	5.052 ft
normalized chord length	$\bar{c}$	0.0488	0.0889
normalized flapping hinge location	$\bar{e}$	0.0357	0.0420
rotor solidity	σ	0.0621	0.0849
normalized root cutout location	$\bar{r}_c$	0.2100	0.2000
normalized inner servoflap location	$\bar{r}_1$	0.6000	0.6000
normalized outer servoflap location	$\bar{r}_2$	0.8000	0.8000
sectional lift curve slope	a	6.30	7.64
sectional servoflap lift coefficient	$\bar{n}$	0.500	0.461
sectional servoflap moment coefficient	$\bar{p}$	-0.082	-0.084
Locke number	γ	8.11	10.10
normalized first torsional frequency	$\bar{\omega}_1$	7.65	4.50

Boeing Helicopters, although no systematic verification was done against the Boeing models.

Figure 3-1 shows the frequency response of the blade tip twisting angle due to root pitch actuation and servoflap actuation. The peak around 7.5Ω is the first torsional natural frequency, and the next two peaks at higher frequency range are the second and third torsional natural frequencies. Other peaks obtained by the present model but not by Garcia's model are either the higher torsional natural frequencies or the artificially stiffened elastic flapping natural frequencies. The present model (as well as Garcia's model) can incorporate as many torsional modes as needed. For convenience, the present model has nine torsional modes and Garcia's model has three torsional modes. By adding more modes, the accuracy of the frequency response around the

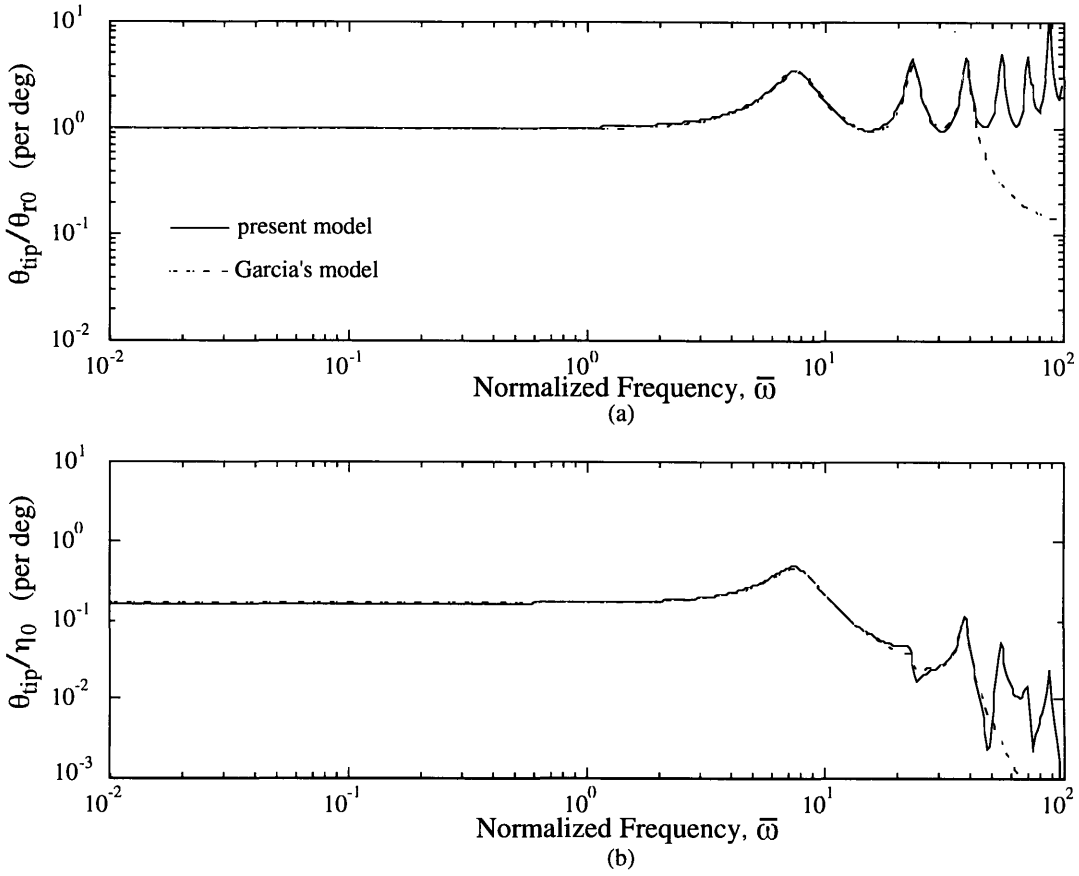

Figure 3-1: Blade tip twist angle due to (a) root pitch actuation and (b) servoflap actuation.

first few modes increases. Therefore, only the results at low frequency range ($< 40\Omega$) in Figure 3-1 should be evaluated, and higher frequency range ($> 40\Omega$) should be ignored. The level of agreement in the frequency responses of the present model and Garcia's model is quite high in both the root pitch actuation and the servoflap actuation cases.

Figure 3-2 shows the frequency response of $G_{\theta_{r_0}}(j\bar{\omega})$ in edgewise flight at various forward flight velocities using the present model. An advance ratio of 0 corresponds to hover, 0.2 is about 80 nautical knots, and 0.4 is about 160 nautical knots. Notice the magnitude of the root pitch actuation at DC increases slightly as the advance ratio is increased. This is due to the fact that higher advance ratio provides higher dynamic pressure on the advancing side of the rotor, and thus more lift is achieved. It should also be noted that rotor operations at higher advance ratio exhibit greater blade stall effects on the blade retreating side of the rotor. The present model does not include

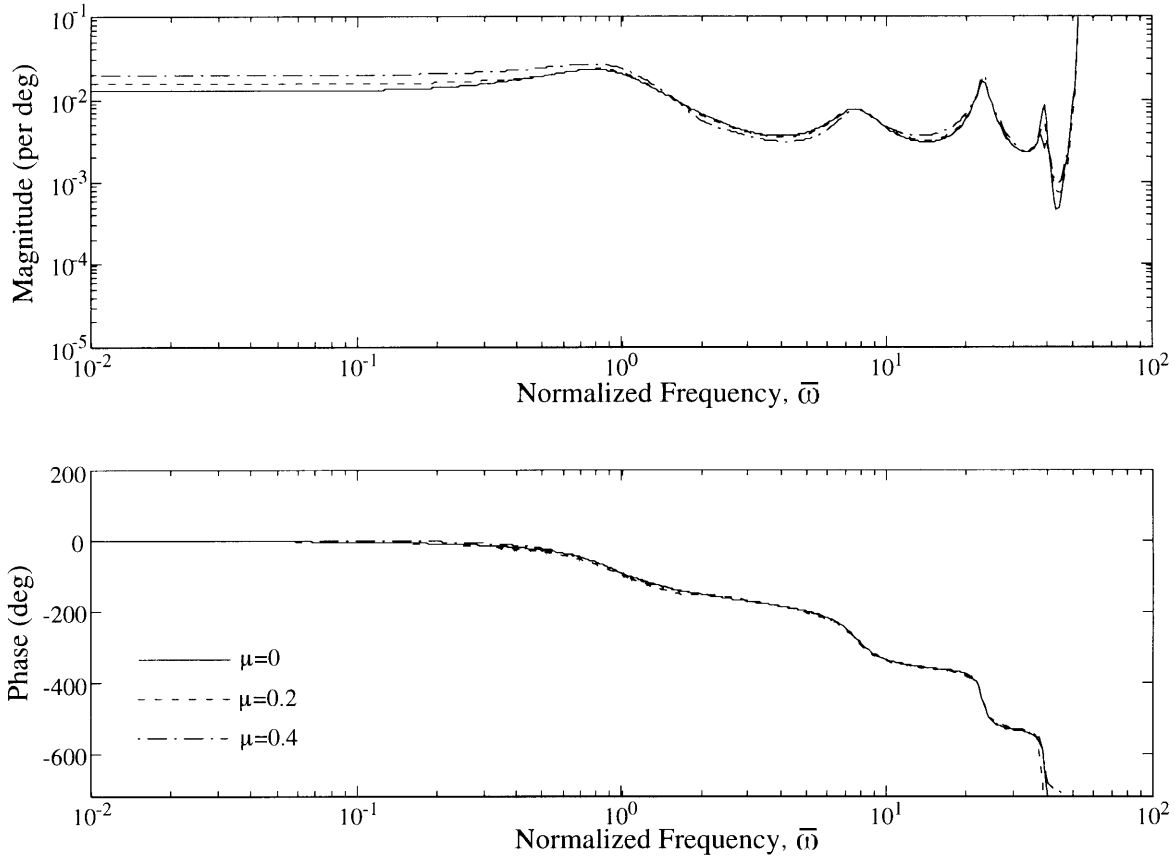

Figure 3-2: $G_{\theta_{r_0}}(j\bar{\omega})$ by the present model with H-34 rotor blade at various forward speeds.

the blade stall effect, so an increase in advance ratio increases the dynamic effects only. Again, the results of frequencies above 40Ω are the high frequency torsional modes and/or artificially stiffened elastic flapping modes, and should be ignored.

The frequency response for the same case using Garcia's model $G_{\eta_0}(j\bar{\omega})$ is shown in Figure 3-3. The locations of natural frequencies, as well as the phase curve, agree with the present model very well. In the high advance ratio case, however, a zero appears in the transfer function around 2Ω, as seen in Figure 3-3, but the zero does not appear in Figure 3-2. In Figure 3-2, the zero may have smoothed out, due to the fact that the flapping stiffness in the present model is not perfectly rigid, as it is in Garcia's case. However, the reason why a zero is introduced only in the high advance ratio cases is not clear. Later in this section, when we compare the H-34 servoflap actuation using the present model to Garcia's model (Figure 3-4 and 3-5), the effect of zero in the high advance ratio cases is evident in Garcia's model, and even though

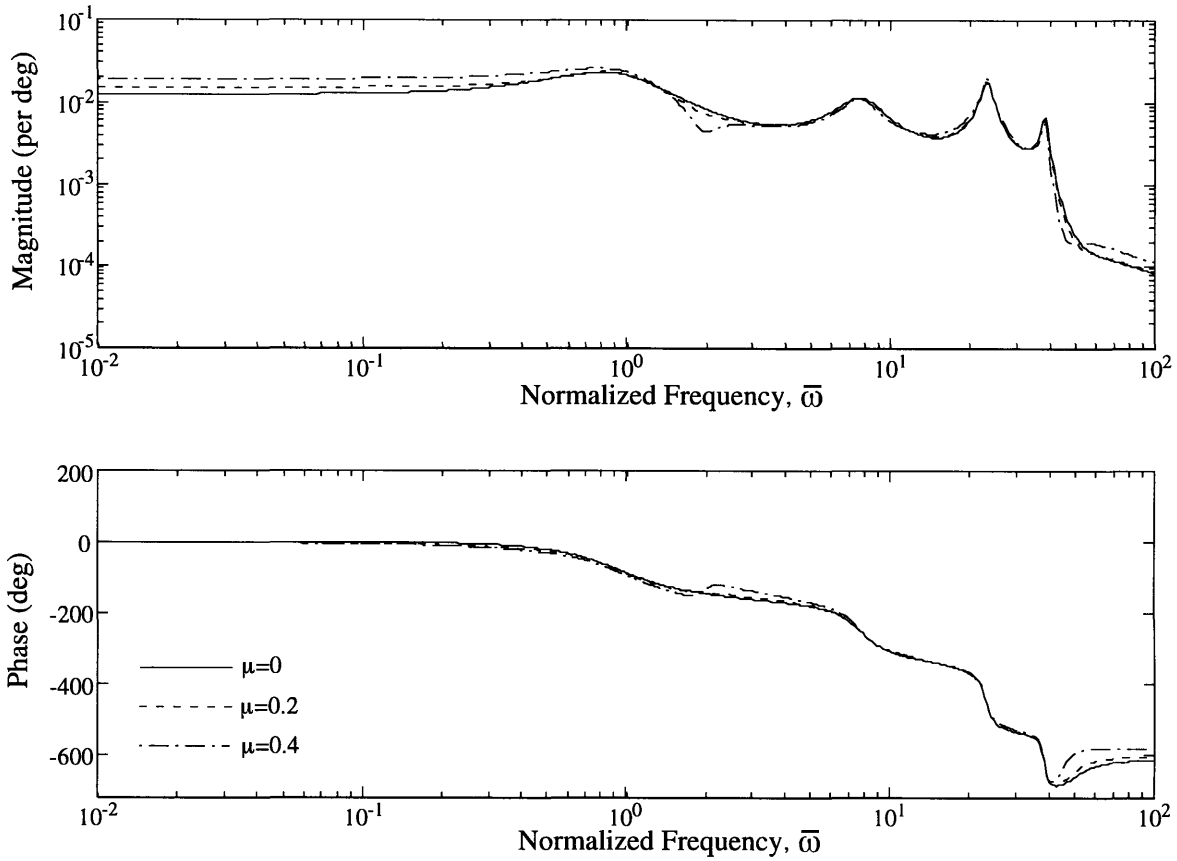

Figure 3-3: $G_{\theta_{T_0}}(j\bar{\omega})$ by Garcia's model with H-34 rotor blade at various forward speeds.

less in magnitude, the same effect is observed in the present model. Therefore, the effect of zero is present in both the present model and Garcia's model; however, the strength of the zero effect is lower in the present model.

Figure 3-4 shows the frequency response $G_{\eta_0}(j\bar{\omega})$ in edgewise flight at various forward flight velocities. It is desired to actuate the servoflap in aileron reversal in order to provide sizable thrust control. Aileron reversal is the condition where positive servoflap deflection twists the blade enough to create a negative rotor thrust change. This is why the thrust output and servoflap input have 180 deg of phase difference, as observed in Figure 3-4, except at DC in the hover case ($\mu = 0$). The dynamic pressure at the servoflap location in hover case is not enough to provide sufficient moment for servoflap deflection to overcome the stiffness of the blade. Using softer blades would achieve aileron reversal easier. However, other problems arise such as instability caused by blade flutter. Aileron reversal of a blade is dependent on the torsional

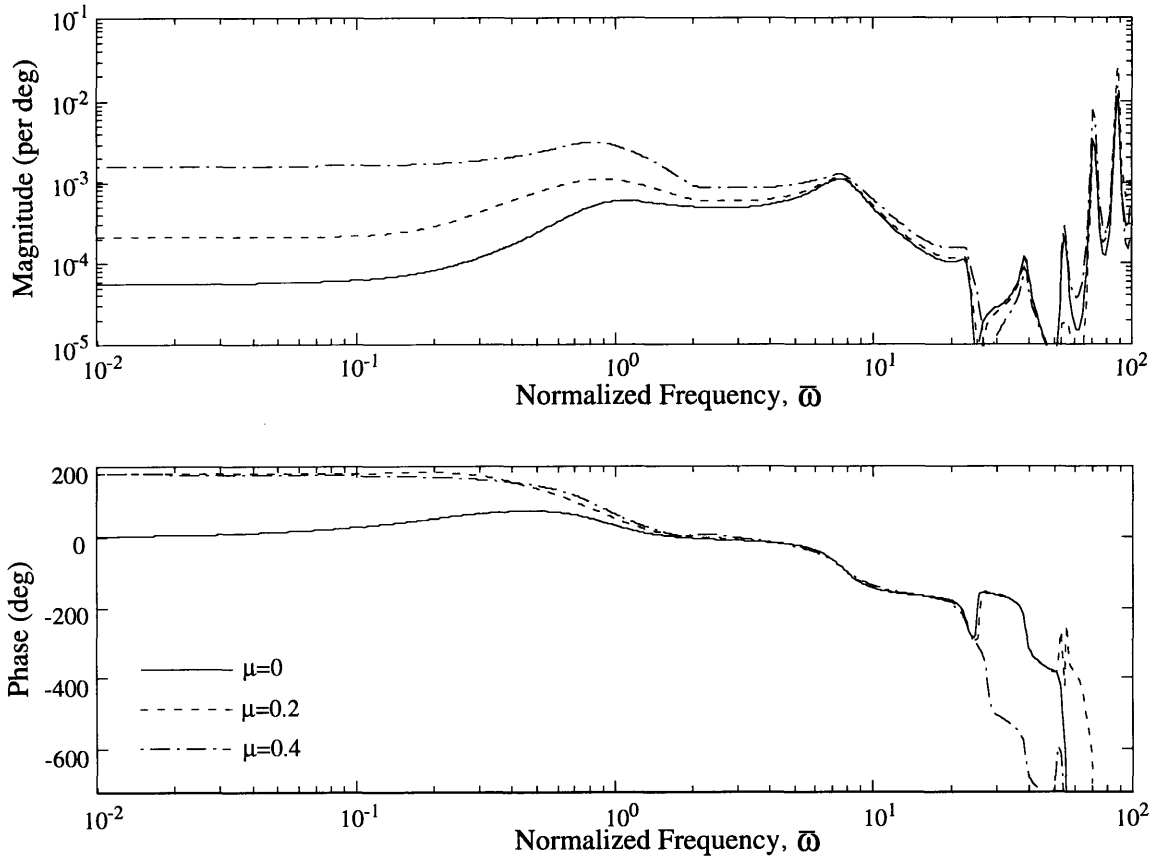

Figure 3-4: $G_{\eta_0}(j\bar{\omega})$ by the state space model with H-34 rotor blade at various forward speeds.

stiffness, location of servoflap, forward flight speed, and many other parameters. The blade response with different servoflap locations is studied later using model scale CH-47 rotor blade.

Figure 3-5 shows Garcia's frequency responses of $G_{\eta_0}(j\bar{\omega})$ in edgewise flight at various forward flight velocities. The hover case also demonstrates the failure of achieving aileron reversal at DC due to torsionally stiff blade and not enough dynamic pressure. The input file of H-34 rotor obtained from Garcia [7] had to be converted from the lumped mass model used by Garcia to the finite element model used in this study, and this conversion creates some discrepancies between the present model and Garcia's model. The DC magnitudes of G_{η_0} show such discrepancies in Figure 3-4 and Figure 3-5.

The effect of the zero in the transfer function, $G_{\eta_0}(j\bar{\omega})$, around 2Ω is much more evident in Garcia's case in Figure 3-5 than in the present model in Figure 3-4. Similar

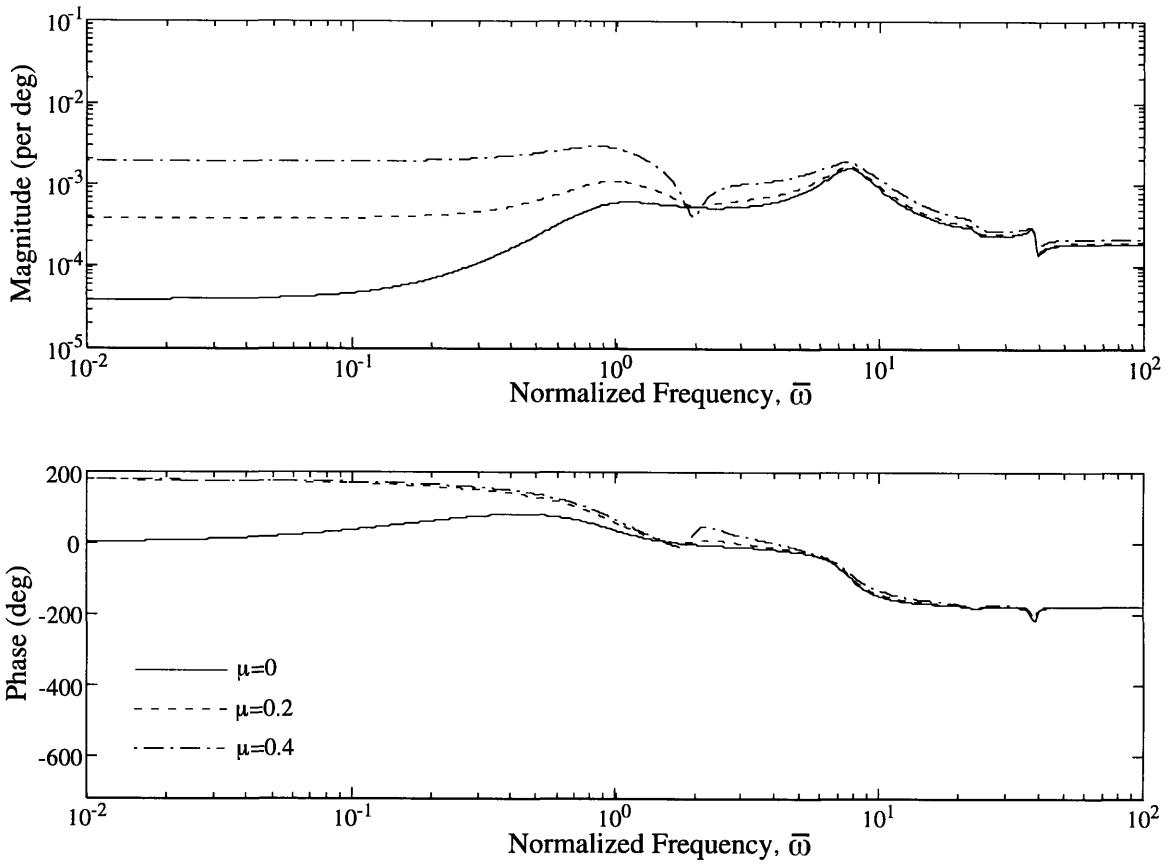

Figure 3-5: $G_{\eta_0}(j\bar{\omega})$ by Garcia's model with H-34 rotor blade at various forward speeds.

to the root pitch actuation case, the finite flapping stiffness in the present model may have smoothed out some of the zero effects, where as Garcia's case which incorporates purely rigid flapping stiffness shows much more of the zero effects.

The general behavior of the H-34 rotor blade determined by both the present model and Garcia's model agree especially in hover case where there is no blade stall effect. For cases at higher advance ratios, the present model and Garcia's model starts to show some differences. These differences may have been caused by the different flapping stiffnesses of the H-34 rotor blade used in the two models. Even though the accuracy of the present model's results in the high advance ratio cases is not as high as in the hover case or in the low advance ratio cases, the results in the high advance ratio cases help to determine the trends of the rotor behavior across the whole frequency envelope.

Other minor differences between the present model and Garcia's model in hover

or in low advance ratio flights, therefore, may have come from the fact that the same problem was solved in two very different methods, and those differences are small enough to ignore. Generally, the frequency response of both root pitch and servoflap actuations in the present model are reliable in hover or at low advance ratio flights. In the next section, the model CH-47 blade is used to study the feasibility of servoflap actuation.

3.3 Parametric Studies

In this section, the model CH-47 rotor with rigid and elastic flapping and elastic torsion is used to simulate the root pitch and the servoflap actuations using the frequency response analysis. Then, parameters such as advance ratio and location of servoflap are varied to observe the blade behavior at different structural and flight situations.

3.3.1 Forward Flight Velocity Study

In this section, the effect of advance ratio on $G_{\theta_{r_0}}(j\bar{\omega})$ and $G_{\eta_0}(j\bar{\omega})$ is investigated. Figure 3-6 and Figure 3-7 display $G_{\theta_{r_0}}(j\bar{\omega})$ and $G_{\eta_0}(j\bar{\omega})$, respectively, with three different advance ratios.

In Figure 3-6, the second, third and fourth flapping natural frequencies can be observed around 2.4Ω, 4.7Ω, and 7.9Ω. The first torsional natural frequency at 4.5Ω is overlapped by the second flapping frequency, which makes it difficult to distinguish in Figure 3-6. The first heavily damped peak at 0.9Ω is the damped rigid flapping mode.

In higher harmonic control for vibration reduction using the CH-47 rotor, the control effort is concentrated around 3Ω. In Figure 3-6, however, the root pitch control around 3Ω is ineffective, due to a zero in the transfer function around the frequency of interest. The zero around 3Ω may be due to the interactions between the second and third flapping modes excited by the root pitch actuation. In order to find the modal force due to the root pitch actuation, the dot product between the

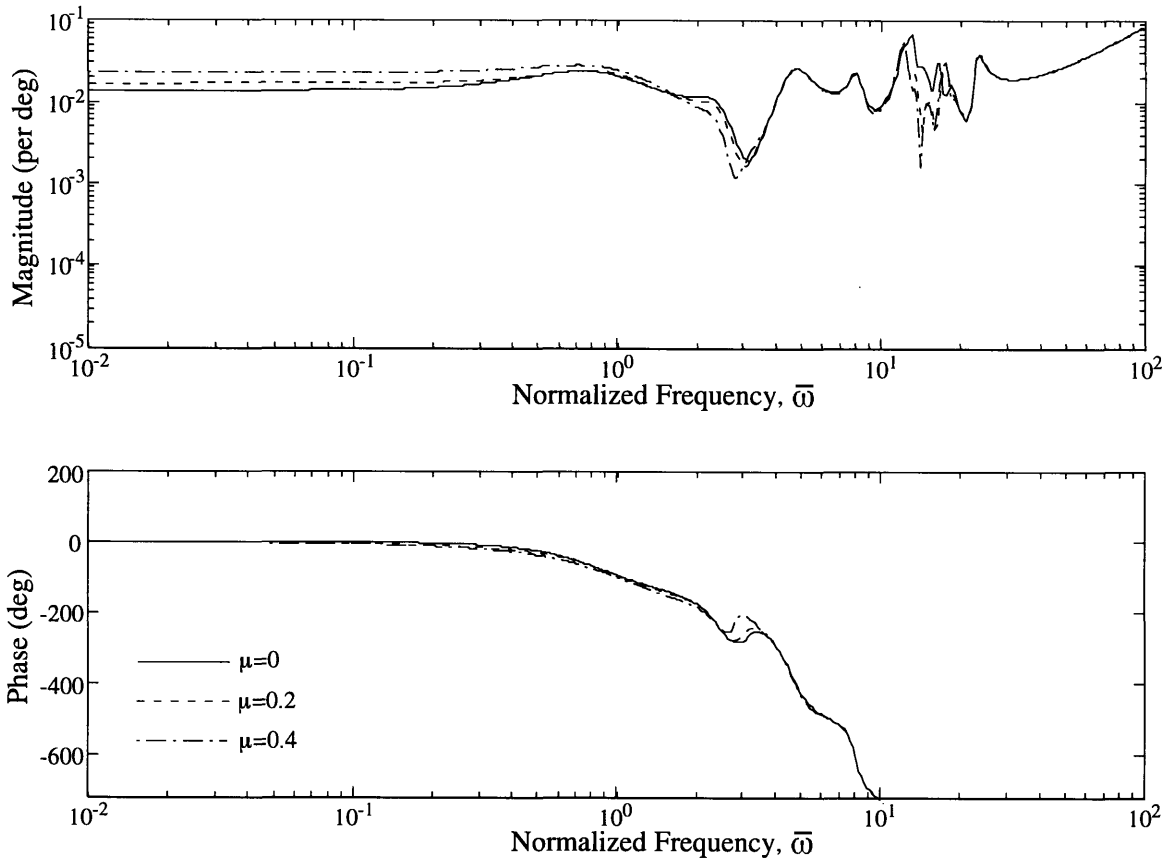

Figure 3-6: $G_{\theta_{r_0}}(j\bar{\omega})$ of model CH-47 rotor at various forward speeds.

spanwise lift force due to the root pitch actuation ($\approx u_T^2 \phi^{\theta_r}(\bar{r})$) and the flapping mode shape ($= \phi^w(\bar{r})$) is taken, as seen in Equation 2.38. The lift force due to the root pitch actuation increases quadratically with radius, thus, the outboard of the rotor blade provides most of the lift. The second and third flapping mode shapes are plotted in Figure 3-8, and the signs of the outboard flapping deflection of the two mode shapes are different. The second flapping mode shape has a positive deflection at outboard, whereas the third flapping mode shape has a negative deflection at outboard. The modal forces due to the second flapping mode and the third flapping mode, therefore, have different signs. The change of sign between the two modal forces indicates that there is a point where root pitch actuation becomes ineffective between the second and third flapping frequencies, and such a point is seen at 3Ω in Figure 3-6. From Figure 3-6, the necessary root pitch actuation angle for achieving 0.1 g thrust increase at 3Ω is about 5 deg.

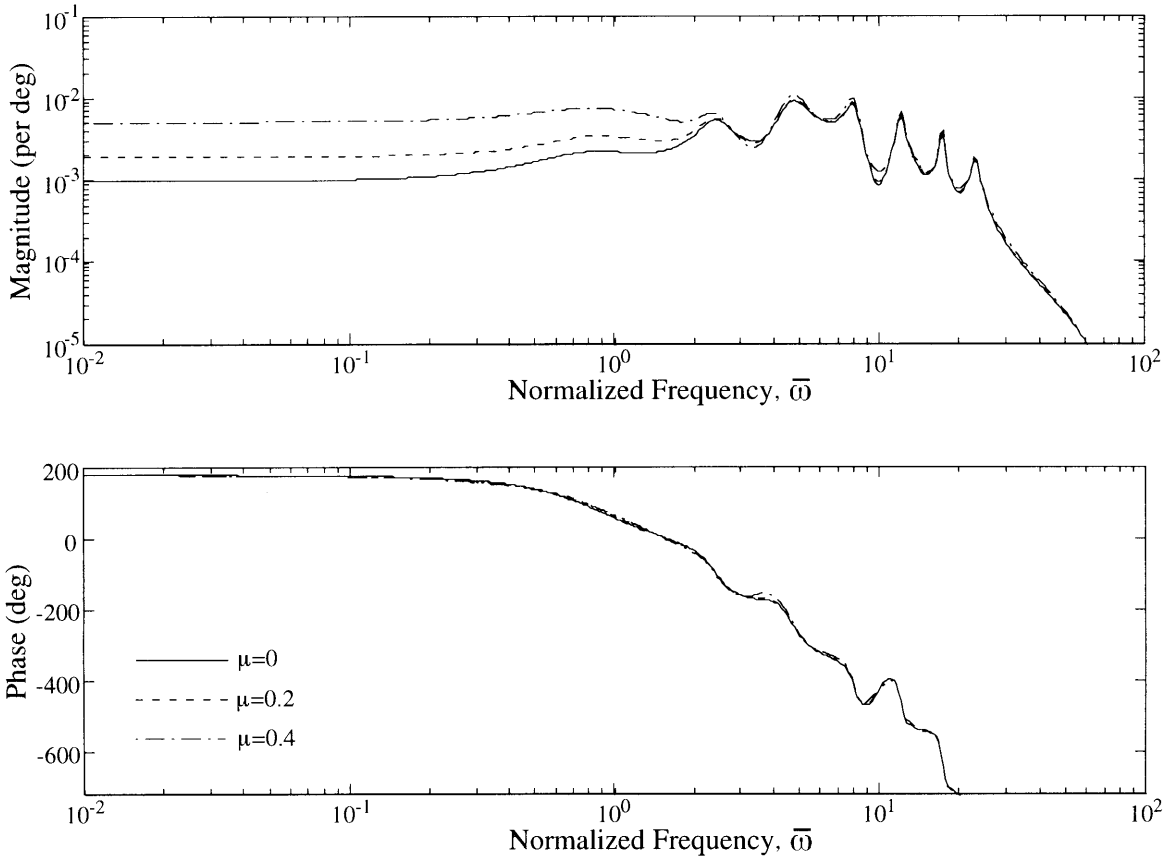

Figure 3-7: $G_{\eta_0}(j\bar{\omega})$ of model CH-47 rotor at various forward speeds.

Figure 3-7 shows the effect of advance ratio on servoflap actuation authority for the model CH-47 rotor. For the low frequency range, the effect of advance ratio is evident. An increase in advance ratio causes the dynamic pressure to increase, which produces more lift and moment, and therefore more thrust authority is achieved. For frequencies higher than the second flapping natural frequency at 2.4Ω, the effect of varying advance ratio diminishes. At 3Ω, there seems to be no effect at all of varying advance ratio on servoflap actuation. The necessary servoflap deflection for achieving 0.1 g thrust increase for the hover case is around 3 deg.

Johnson [11, p.568] discusses the relative accuracy of linear time invariant and periodic models. The major difference between the two types of models is the elimination of periodic terms during the process of multi-blade coordinates, which is done only for the linear time invariant model (See Appendix B). All the eliminated peri-

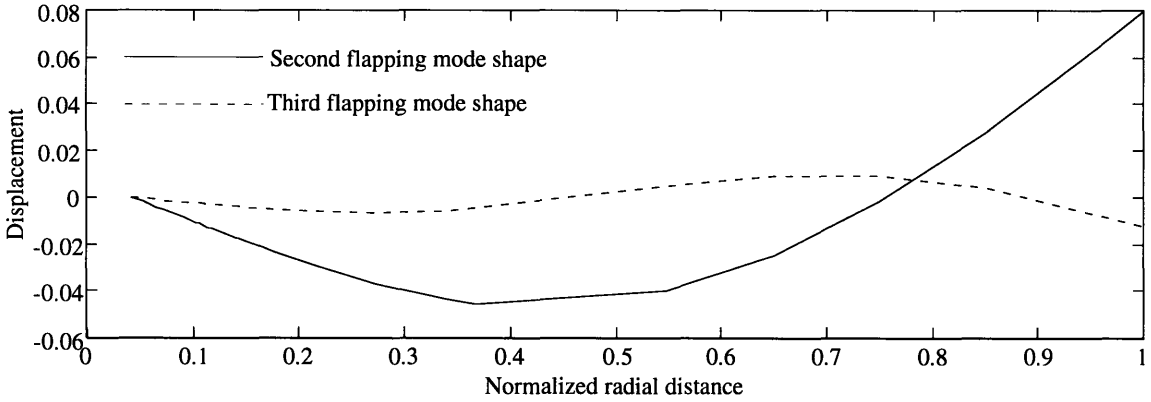

Figure 3-8: The second and third flapping mode shape of model CH-47 rotor blade.

odic terms happen to be multiples of advance ratio. Therefore, there is a significant amount of forward flight information loss when a linear time invariant model is used. This also means that flight cases with small advance ratios, while having some error, will be more accurate than high advance ratio cases.

Another possible reason for the missing advance ratio influence on the servoflap actuation is that blade stall effect is not included in the state space model. The blades experience stall when rotating through the retreating side, especially during the high advance ratio flights. Modeling of the blade stall is very complicated, so it was not included in the model. However, it is known that the effect of blade stall can have a large effect on rotor dynamics.

In general, the present model shows valid root pitch and servoflap frequency responses in hover case. As the advance ratio increases, the accuracy of the frequency responses decreases. During the process of forming the present state space model, some terms with advance ratio were neglected during multi-blade coordinates. Also, blade stall effects are not included in the present model. These simplifications may have caused the loss of accuracy in forward flight cases. However, the general rotor behavior can be observed through out a wide range of frequency envelope, and the reliability of the hover and low advance ratio cases are acceptable.

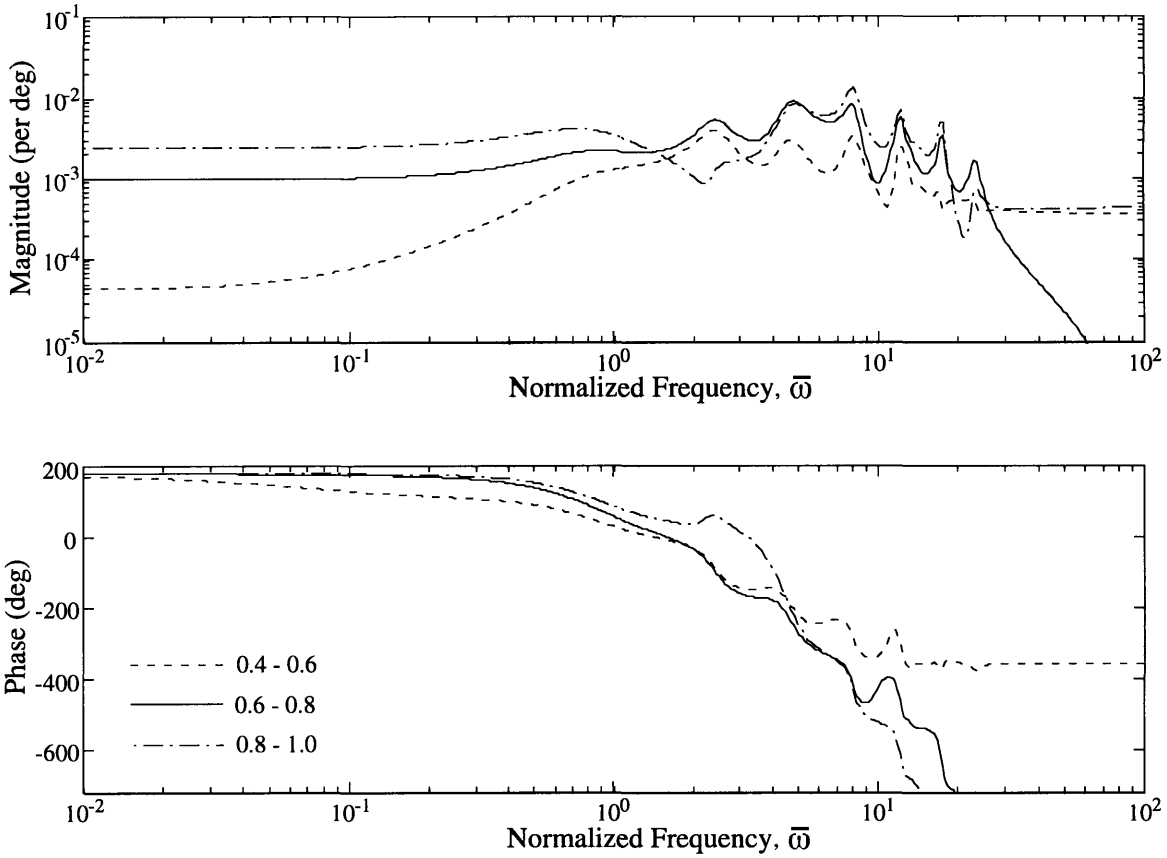

Figure 3-9: $G_{\eta_0}(j\bar{\omega})$ of model CH-47 rotor blade at hover with various servoflap locations.

3.3.2 Servoflap Location Study

In this section, the effect of servoflap placement on $G_{\eta_0}(j\bar{\omega})$ is investigated. Keeping the servoflap span constant at $0.2R$, the radial position is varied from $\bar{r} = 0.4$-0.6 to $\bar{r} = 0.8$-1.0 in hover and forward flight cases. Generally, it is desirable to place the servoflap inboard on the blade, because the actuator is subjected to a centripetal force which is proportional to the radial distance from the root. There is no guarantee that actuators can stand hundreds of g's of centripetal force. Also, the root and hub must be built to hold the stress each blades with actuators exert while rotating.

Figure 3-9 shows the frequency response of $G_{\eta_0}(j\bar{\omega})$ at hover with three different servoflap locations. Aerodynamically, the farther out the servoflap is located, the more effective servoflap actuation becomes due to the increase in dynamic pressure. Also, the effective torsional stiffness of the blade decreases as servoflap is moved

outward, since

$$\text{effective torsional stiffness} \approx \frac{\text{sectional torsional stiffness}}{\text{distance between root and servoflap}} \tag{3.2}$$

and the distance between the root and servoflap is longer. This is why placing the servoflap at $\bar{r} = 0.6\text{-}0.8$ is more effective than placing it at $\bar{r} = 0.4\text{-}0.6$, as seen in Figure 3-9.

By placing the servoflap at $\bar{r} = 0.8\text{-}1.0$, it would be expected to have even higher effectiveness in servoflap actuation. However, there is a zero in the transfer function around 3Ω, which actually makes the servoflap actuation less effective. This phenomena is caused by the interaction between the second flapping mode and the first torsional mode [15]. Placing the centroid of the servoflap on the node location of the second flapping mode minimizes the excitation of that mode. The node location of the second flapping mode is around $0.75R$ as seen in Figure 3-8. Moving the centroid of the servoflap outward from the node location of the second flapping mode causes the excitation of the second flapping and first torsional modes. The interaction of the two modes, then, cancels each other and reduces the effectiveness of 3Ω servoflap actuation.

Similar results are observed in Figure 3-10, in which the effects of servoflap location on $G_{\eta_0}(j\bar{\omega})$ with an advance ratio of 0.2 are shown. The effectiveness of the servoflap actuation increases as its location moves from $\bar{r} = 0.4\text{-}0.6$ to $\bar{r} = 0.6\text{-}0.8$. When the servoflap is moved to $\bar{r} = 0.8\text{-}1.0$, centroid of the servoflap moves outboard of the node location of the second flapping mode shape. Therefore, a zero is introduced to the transfer function which lowers the servoflap actuation effectiveness.

It is desired to place the servoflap inboard to reduce the high centripetal forces exerted on the actuators. However, the actuators must also be effective in terms of thrust control, and placing them too close to the root would not allow the servoflaps to operate in aileron reversal. It is also desired to minimize the interaction between the second flapping and the first torsional modes, which introduces a zero in the transfer function around 3Ω. From these considerations, placing the servoflap between the

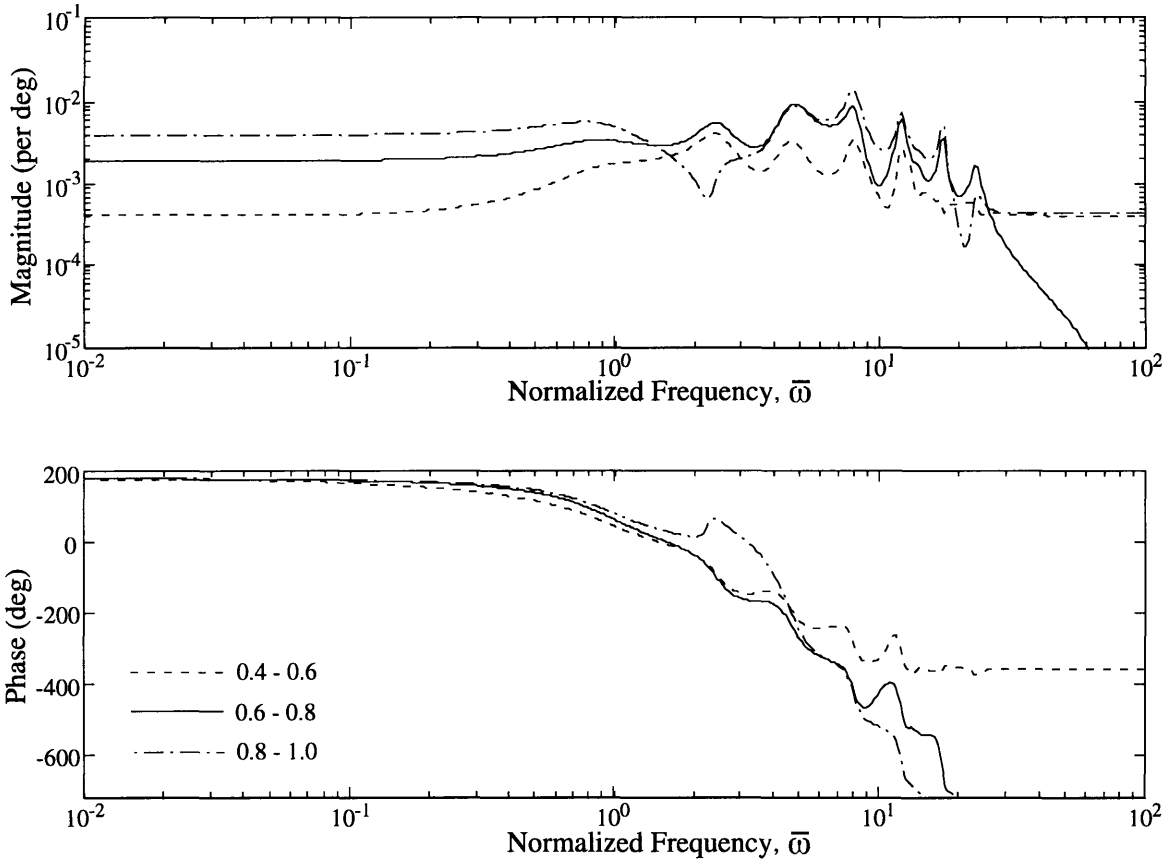

Figure 3-10: $G_{\eta_0}(j\bar{\omega})$ of model CH-47 rotor blade at $\mu = 0.2$ with various servoflap locations.

range of $\bar{r} = 0.4$ to 0.8 would allow effective servoflap actuations. Minimum servoflap deflection is required if the servoflap is located at $\bar{r} = 0.6$-0.8. If not possible due to the mechanical difficulties, then, the servoflap must be moved inboard where larger servoflap deflections are required.

3.3.3 Blade Tip Motion Comparison

In this section, the necessary blade tip pitch angle and its coefficient of lift for achieving 0.1 g thrust increase with forward flight velocities of 80 knots ($\mu = 0.18$) and 160 knots ($\mu = 0.36$) are compared between the present model results and Boeing's results. Boeing Helicopters has run their rotor analysis program using model CH-47 blade with 35 percent chord wide and 10 percent radially long servoflap located at 85 to 95 percent span. Our model, therefore, uses a servoflap sized and located the

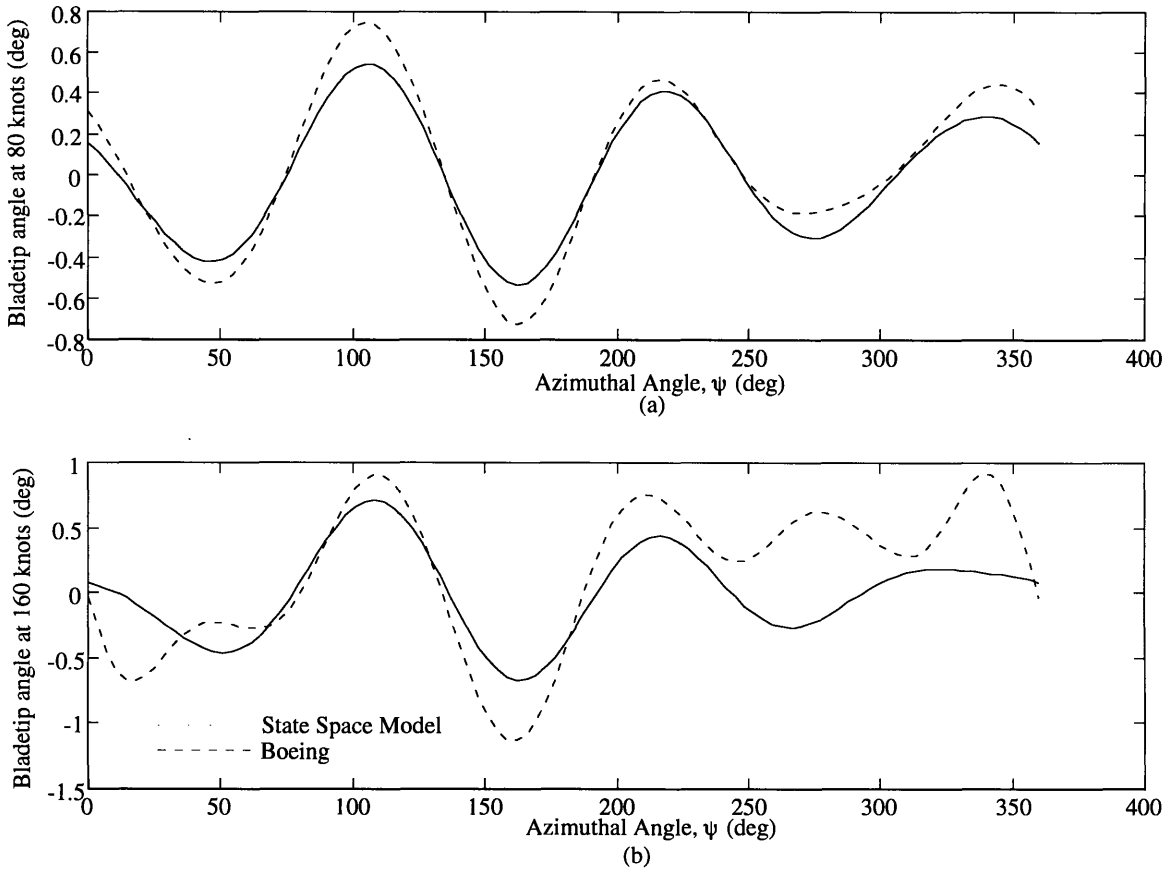

Figure 3-11: Rotor blade tip pitch angle verses azimuthal angle at (a) 80 knots and (b) 160 knots. Solid line is the state space model result and dashed line is Boeing's result.

same as the Boeing's configuration. The data from Boeing Helicopters includes the blade's spanwise pitch angle verses azimuthal angle and other data with and without the 3Ω servoflap actuation. Only the blade tip pitch angle and coefficient of lift verses azimuthal angle are investigated here.

Figure 3-11 shows the change of rotor blade tip pitch angle during one cycle of rotation at two different forward flight speeds. The servoflap is actuated at 3Ω and deflected enough to achieve about 0.1 g thrust increase. The magnitude of the servoflap deflection is on the order of 3 to 5 deg. The 80 knot case is plotted in Figure 3-11(a) and 160 knot case is plotted in Figure 3-11(b). The present model result and Boeing's result are plotted as solid line and dashed line, respectively. In both cases, the blade tip pitch angle on the advancing side ($0 < \psi < 180$) shows larger magnitudes of angle motions compared to the blade tip pitch angle on the retreating

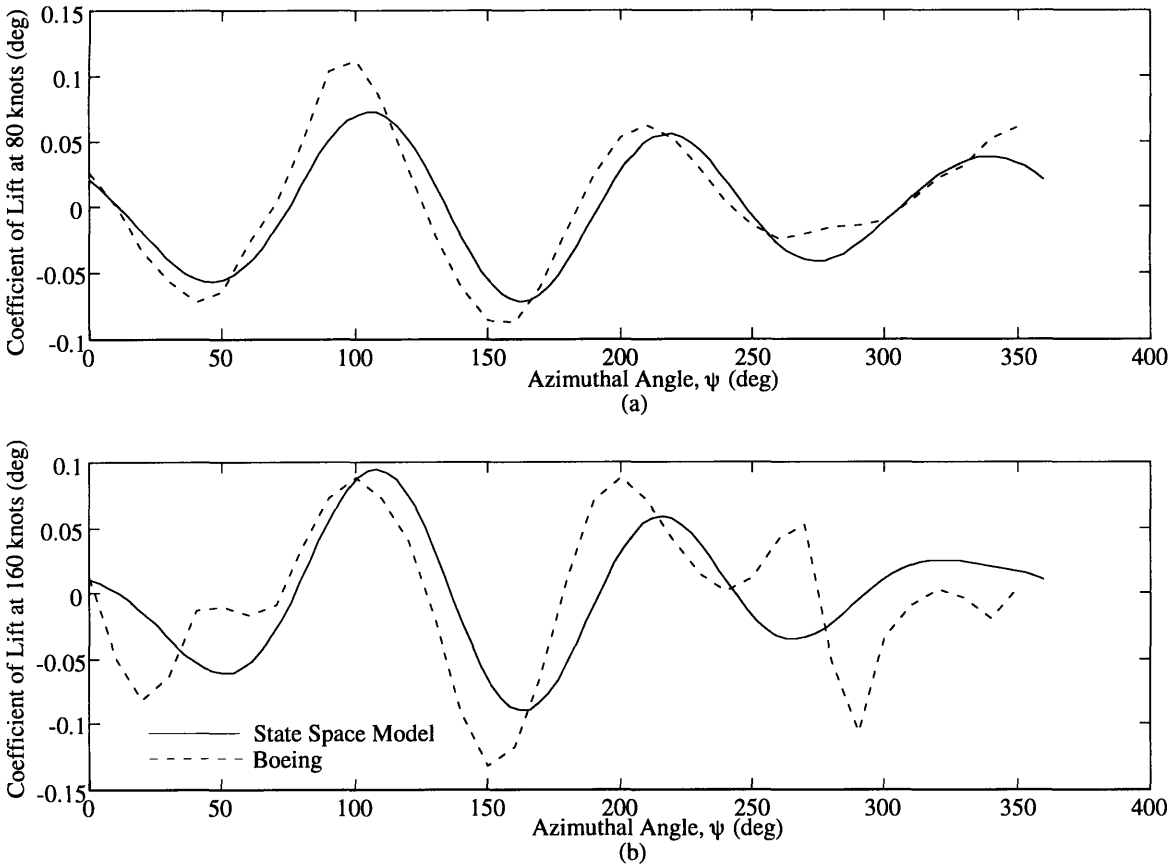

Figure 3-12: Coefficient of Lift at blade tip verses azimuthal angle at (a) 80 knots($\mu = 0.18$) and (b) 160 knots($\mu = 0.36$). Solid line is the state space model result and dashed line is Boeing's result.

side ($180 < \psi < 360$). This is expected, since the relative velocity of the blade to airspeed is higher on the advancing side than on the retreating side. At 80 knots, the agreement between the present model and Boeing's results is good. At 160 knots, the agreement is not as good. The effect of blade stall and nonlinear aerodynamics incorporated in Boeing's model predicts different blade tip motions in high advance ratio flight, especially on the retreating side. As stated before, the present model does not include such nonlinearities.

Figure 3-12 shows the present model results of coefficient of lift at blade tip verses azimuthal angle in solid line and Boeing's results in dashed line at 80 knots and 160 knots. The step taken in the present model from Figure 3-11 to achieve Figure 3-12 is just multiplying the lift curve slope, c_{l_α}, by the blade tip angle curve. However, Boeing's results in both Figure 3-12 (a) and (b) show a slight phase shift and the

presence of blade stall, which are not seen in Figure 3-11 (a) and (b). This is due to the more complicated aerodynamic model used by Boeing. Predicting the rotor behavior becomes more difficult as the advance ratio is increased, since the present model does not include the blade stall effects. Also the linear, time invariant, system ignores some terms with advance ratio during the multi-blade coordinates. Again, the correspondence between the present model and Boeing's results at 80 knots is good but the agreement at 160 knots is not as good.

Even though the detailed pitch angle and coefficient of lift at blade tip were not simulated well by the present model, the general trends and the order of magnitudes were matched with Boeing Helicopter's results, especially in the low advance ratio cases. This indicates that the reliability of the present model at low advance ratio flights is acceptable as a device to predict the general requirements for doing servoflap actuations. Even though the information about the pitch angle and the coefficient of lift at blade tip in hover were not available from Boeing Helicopters, it can be predicted from that those data by the present model and the Boeing's model would agree as well, or agree even better than they did in the 80 knot case.

Chapter 4

Conclusions

In this thesis, a linear time invariant state space model of a helicopter rotor with root pitch or servoflap actuation has been developed. The model includes elastic blade torsion and elastic blade bending. The model also includes the dynamic inflow model developed by Pitt and Peters [17]. The use of multi-blade coordinates and neglecting some periodic terms of the rotor dynamics result in an approximate linear time invariant model for the helicopter dynamics.

Parametric studies of varying forward flight speed and servoflap location have been performed using the model CH-47 rotor blade. The summary of the parametric studies is given in the following section.

4.1 Summary of Parametric Studies

Root pitch actuation and servoflap actuation were compared at several different advance ratios using the one sixth model scale CH-47 rotor. The root pitch actuation seemed to be less sensitive to the advance ratio compared to the case in servoflap actuation. But in both cases for constant input, cases with higher advance ratio provided larger thrust control authority. At 3/rev actuation frequency, however, both root pitch and servoflap actuation demonstrated much less sensitivity of the thrust control authority to advance ratio.

The servoflap location study demonstrated the importance of choosing the appro-

Table 4.1: Effectiveness of root pitch and servoflap actuation at 3/rev for various flight speed and servoflap locations.

Advance Ratio	Servoflap location	$\frac{C_T/\sigma}{\theta_{r_0}}$ (per deg)	$\frac{C_T/\sigma}{\eta_0}$ (per deg)	Actuation for 0.1 g	
				θ_{r_0}	η_0
0	0.4-0.6	2.18e-03	2.05e-03	4.6	4.9
0	0.6-0.8	2.18e-03	3.36e-03	4.6	3.0
0	0.8-1.0	2.18e-03	1.70e-03	4.6	5.9
0.2	0.4-0.6	1.68e-03	2.02e-03	5.9	5.0
0.2	0.6-0.8	1.68e-03	3.26e-03	5.9	3.1
0.2	0.8-1.0	1.68e-03	2.07e-03	5.9	4.8
0.4	0.4-0.6	1.76e-03	1.91e-03	5.7	5.2
0.4	0.6-0.8	1.76e-03	3.03e-03	5.7	3.3
0.4	0.8-1.0	1.76e-03	3.00e-03	5.7	3.3

priate servoflap location in order to achieve efficient thrust control. By adding the flapping modes to the state space model, phenomena such as coupling of the first torsional mode and the second flapping mode were observed. This phenomena was not seen in Garcia's model [7] because it does not incorporate any elastic flapping modes. The best location to attach the servoflap seems to be near the node point of the second flapping mode ($\bar{r} = 0.75$). By doing this, the excitation of the second flapping mode can be suppressed, and the coupling with the first torsional mode can be minimized. Therefore, placing a servoflap at $\bar{r} = 0.6$-0.8 is found much more effective than placing it at $\bar{r} = 0.8$-1.0. A similar result was observed by Millott and Friedmann [15].

The results of necessary root pitch actuation and servoflap actuation for achieving 0.1 g of thrust increase are tabulated in Table 4.1. The width of the servoflap is 20

percent chord and the length is 20 percent of the radius of the helicopter rotor disk.

Note that the state space model presented here has two important approximations that affect the output rotor behavior. The state space model lacks the blade stall model, and stall effects are important for high advance ratio flights. During the multi-blade coordinates, some of the products of advance ratio and periodic terms are neglected to achieve a linear time invariant system. Therefore, for low advance ratio flights, the error is small enough to ignore. However, in high advance ratio flight, the uncertainty in the present model results increase. In any case, even though two important simplifications are made during the process of deriving the state space model, the general requirements and trends can be estimated by this model.

4.2 Future Possible Work

Adding elastic flapping modes to the state space model allowed us to learn the phenomena where first torsional mode and second flapping mode couple and lower the thrust control authorities. This phenomena was also predicted by Millott and Freidmann [15] previously, but they also stated that lead-lag modes couple with flapping and torsional modes. Therefore, adding the lead-lag modes to the state space model would allow us to simulate the blade more realistically and possibly find new phenomena that cannot be seen by the present model.

The requirement that the model be linear time invariant system during forward flight lowers the accuracy of the state space model, especially in flights with high advance ratios. During the multi-blade coordinates, if linear periodic system can be incorporated rather than linear time invariant system, then products of the advance ratios and periodic properties don't have to be neglected, and the accuracy of the state space model in forward flight case would rise.

If the lift curve slope is allowed to vary along the radius and around the azimuthal angle, nonlinear effects such as blade stall can easily be incorporated into the state space model. The bladetip results from Boeing Helicopters presented in Section 3-3-3 were calculated with variable lift curve slope radially and azimuthally. However, the

state space model developed in this study has only one value of lift curve slope for any radial or azimuthal locations. Radially and azimuthally variable lift curve slope would allow the state space model to capture the rotor behavior more realistically.

The state space model developed in this study only accepts one servoflap per blade, but due to the linearity of the model, it would not be hard to modify the code to accept several servoflaps at desired locations actuated at desired frequencies.

Appendix A

Rotor Integrals and Matrices

This Appendix lists all the necessary integrals and matrices used in Chapter 2 in order to derive the state space model.

A.1 Aerodynamic Integrals

$$
\begin{aligned}
A^k_{mn} &= \gamma \int_{\bar{r}_c}^{B} \frac{1}{2} \bar{r}^k \phi^{\theta}_n (\bar{r}) \, \phi^{w}_m (\bar{r}) \, d\bar{r} \\
B^k_{mn} &= -\gamma \int_{\bar{r}_c}^{B} \frac{1}{2} \bar{r}^k \phi^{w'}_n (\bar{r}) \, \phi^{w}_m (\bar{r}) \, d\bar{r} \\
C^k_{mn} &= -\gamma \int_{\bar{r}_c}^{B} \frac{1}{2} \bar{r}^k \phi^{w}_n (\bar{r}) \, \phi^{w}_m (\bar{r}) \, d\bar{r} \\
D^k_{m} &= \gamma \int_{\bar{r}_c}^{B} \frac{1}{2} \bar{r}^k \phi^{w}_m (\bar{r}) \, d\bar{r} \\
E^k_{m} &= \gamma \int_{\bar{r}_1}^{\bar{r}_2} \frac{1}{2} \bar{n} \bar{r}^k \phi^{w}_m (\bar{r}) \, d\bar{r} \\
F^k &= \sigma a \int_{\bar{r}_c}^{B} \bar{r}^k \phi^{\theta_r} (\bar{r}) \, d\bar{r} \\
G^k_{m} &= \sigma a \int_{\bar{r}_c}^{B} \bar{r}^k \phi^{\theta}_m (\bar{r}) \, d\bar{r} \\
H^k_{m} &= -\sigma a \int_{\bar{r}_c}^{B} \bar{r}^k \phi^{w'}_m (\bar{r}) \, d\bar{r} \\
J^k_{m} &= -\sigma a \int_{\bar{r}_c}^{B} \bar{r}^k \phi^{w}_m (\bar{r}) \, d\bar{r} \\
K^k &= \sigma a \int_{\bar{r}_1}^{\bar{r}_2} \bar{n} \bar{r}^k d\bar{r}
\end{aligned}
$$

$$
\begin{aligned}
L_m^k &= \gamma \int_{\bar{r}_1}^{\bar{r}_2} \frac{1}{2} \bar{p}\bar{c}\bar{r}^k \phi_m^\theta(\bar{r})\, d\bar{r} \\
M_{mn}^k &= -\gamma \int_{\bar{r}_c}^{B} \frac{\bar{c}^2}{16} \bar{r}^k \phi_n^\theta(\bar{r})\, \phi_m^\theta(\bar{r})\, d\bar{r} \\
N_m^k &= -\gamma \int_{\bar{r}_c}^{B} \frac{\bar{c}^2}{16} \bar{r}^k \phi^{\theta_r}(\bar{r})\, \phi_m^\theta(\bar{r})\, d\bar{r} \\
S_m^k &= \gamma \int_{\bar{r}_c}^{B} \frac{1}{2} \bar{r}^k \phi^{\theta_r}(\bar{r})\, \phi_m^w(\bar{r})\, d\bar{r}
\end{aligned}
$$

A.2 Structural Integrals

$$
\begin{aligned}
I_b &= \int_0^R m r^2 dr \\
m_{\ddot{a}}^*(m) &= \frac{\sigma a R}{\gamma I_b} \int_{r_e}^{R} \left(m x_{cg} \phi_m^\theta(r) - m \phi_m^w(r) \right)\, dr \\
m_{\ddot{\theta}_r}^* &= \frac{\sigma a R}{\gamma I_b} \int_{r_e}^{R} m x_{cg} \phi^{\theta_r}(r)\, dr
\end{aligned}
$$

A.3 Δ and Ψ Matrices

$$
\boldsymbol{\Delta}_{\ddot{\mathbf{a}}} = \begin{bmatrix} M_{LL} & 0 & 0 \\ 0 & M_{LL} & 0 \\ 0 & 0 & M_{LL} \end{bmatrix}, \quad \boldsymbol{\Delta}_{\dot{\mathbf{a}}} = \begin{bmatrix} 0 & 0 & 0 \\ 0 & 0 & 2M_{LL} \\ 0 & -2M_{LL} & 0 \end{bmatrix},
$$

$$
\boldsymbol{\Delta}_{\mathbf{a}} = \begin{bmatrix} K_{LL} & 0 & 0 \\ 0 & K_{LL} - M_{LL} & 0 \\ 0 & 0 & K_{LL} - M_{LL} \end{bmatrix}.
$$

$$
\boldsymbol{\Psi}_{\theta_{\mathbf{r}}} = \begin{bmatrix} K_{L0} & 0 & 0 \\ 0 & K_{L0} - M_{L0} & 0 \\ 0 & 0 & K_{L0} - M_{L0} \end{bmatrix}, \quad \boldsymbol{\Psi}_{\dot{\theta}_{\mathbf{r}}} = \begin{bmatrix} 0 & 0 & 0 \\ 0 & 0 & 2M_{L0} \\ 0 & -2M_{L0} & 0 \end{bmatrix},
$$

$$
\boldsymbol{\Psi}_{\ddot{\theta}_{\mathbf{r}}} = \begin{bmatrix} M_{L0} & 0 & 0 \\ 0 & M_{L0} & 0 \\ 0 & 0 & M_{L0} \end{bmatrix}.
$$

A.4 L and M Matrices

$$\mathbf{L_a} = \begin{bmatrix} A^2 + \frac{1}{2}\mu^2 A^0 & \frac{1}{2}\mu\,(B^1 - C^0) & \mu A^1 \\ \mu B^1 & A^2 + \frac{1}{4}\mu^2 A^0 & \frac{1}{4}\mu^2 B^0 + C^1 \\ 2\mu A^1 & \frac{1}{4}\mu^2 B^0 - C^1 & A^2 + \frac{3}{4}\mu^2 A^0 \end{bmatrix},\ \mathbf{L_{\dot{a}}} = \begin{bmatrix} C^1 & 0 & \frac{1}{2}\mu C^0 \\ 0 & C^1 & 0 \\ \mu C^0 & 0 & C^1 \end{bmatrix},$$

$$\mathbf{L}_{\theta_\mathbf{r}} = \begin{bmatrix} S^2 + \frac{1}{2}\mu^2 S^0 & 0 & \mu S^1 \\ 0 & S^2 + \frac{1}{4}\mu^2 S^0 & 0 \\ 2\mu S^1 & 0 & S^2 + \frac{3}{4}\mu^2 S^0 \end{bmatrix},\ \mathbf{L}_\lambda = \begin{bmatrix} -D^1 & 0 & -\frac{1}{2}\mu D^1 \\ 0 & -D^2 & 0 \\ -\mu D^0 & 0 & -D^2 \end{bmatrix},$$

$$\mathbf{L}_\eta = \begin{bmatrix} E^2 + \frac{1}{2}\mu^2 E^0 & 0 & \mu E^1 \\ 0 & E^2 + \frac{1}{4}\mu^2 E^0 & 0 \\ 2\mu E^1 & 0 & E^2 + \frac{3}{4}\mu^2 E^0 \end{bmatrix}.\ \mathbf{M_a} = \begin{bmatrix} 0 & -\frac{1}{2}\mu M^0 & 0 \\ 0 & 0 & M^1 \\ 0 & -M^1 & 0 \end{bmatrix},$$

$$\mathbf{M_{\dot{a}}} = \begin{bmatrix} M^1 & 0 & \frac{1}{2}\mu M^0 \\ 0 & M^1 & 0 \\ \mu M^0 & 0 & M^1 \end{bmatrix}.\ \mathbf{M}_{\theta_\mathbf{r}} = \begin{bmatrix} 0 & -\frac{1}{2}\mu N^0 & 0 \\ 0 & 0 & N^1 \\ 0 & -N^1 & 0 \end{bmatrix},$$

$$\mathbf{M}_{\dot{\theta}_\mathbf{r}} = \begin{bmatrix} N^1 & 0 & \frac{1}{2}\mu N^0 \\ 0 & N^1 & 0 \\ \mu N^0 & 0 & N^1 \end{bmatrix}.\ \mathbf{M}_\eta = \begin{bmatrix} L^2 + \frac{1}{2}\mu^2 L^0 & 0 & \mu L^1 \\ 0 & L^2 + \frac{1}{4}\mu^2 L^0 & 0 \\ 2\mu L^1 & 0 & L^2 + \frac{3}{4}\mu^2 L^0 \end{bmatrix}.$$

A.5 Γ Matrices

$$\mathbf{\Gamma_a} = \begin{bmatrix} \frac{1}{2}G^2 + \frac{1}{4}\mu^2 G^0 & \frac{1}{4}\mu H^1 - \frac{1}{4}\mu J^0 & \frac{1}{2}\mu G^1 \\ -\frac{\bar{e}}{4}\mu H^1 & -\frac{\bar{e}}{4}G^2 - \frac{\bar{e}}{16}\mu^2 G^0 & -\frac{\bar{e}}{4}J^1 - \frac{\bar{e}}{16}\mu^2 H^0 \\ \frac{\bar{e}}{2}\mu G^1 & -\frac{\bar{e}}{4}J^1 + \frac{\bar{e}}{16}\mu^2 H^0 & \frac{\bar{e}}{4}G^2 + \frac{3}{16}\bar{e}\mu^2 G^0 \end{bmatrix},$$

$$\mathbf{\Gamma_{\dot{a}}} = \begin{bmatrix} \frac{1}{2}J^1 & 0 & \frac{1}{4}\mu J^0 \\ 0 & -\frac{\bar{e}}{4}J^1 & 0 \\ \frac{\bar{e}}{4}\mu J^0 & 0 & \frac{\bar{e}}{4}J^1 \end{bmatrix}.$$

$$\mathbf{\Gamma}_{\theta_\mathbf{r}} = \begin{bmatrix} \frac{1}{2}F^2 + \frac{1}{4}\mu^2 F^0 & 0 & \frac{1}{2}\mu F^1 \\ 0 & -\frac{\bar{e}}{4}F^2 - \frac{\bar{e}}{16}\mu^2 F^0 & 0 \\ \frac{\bar{e}}{2}\mu F^1 & 0 & \frac{\bar{e}}{4}F^2 + \frac{3}{16}\bar{e}\mu^2 F^0 \end{bmatrix},$$

$$\mathbf{\Gamma}_{\lambda} = \begin{bmatrix} -\frac{1}{2}F^1 & 0 & -\frac{1}{4}\mu F^1 \\ 0 & \frac{\bar{e}}{4}F^2 & 0 \\ -\frac{\bar{e}}{4}\mu F^0 & 0 & -\frac{\bar{e}}{4}F^2 \end{bmatrix}.$$

$$\mathbf{\Gamma}_{\eta} = \begin{bmatrix} \frac{1}{2}K^2 + \frac{1}{4}\mu^2 K^0 & 0 & \frac{1}{2}\mu K^1 \\ 0 & -\frac{\bar{e}}{4}K^2 - \frac{\bar{e}}{16}\mu^2 K^0 & 0 \\ \frac{\bar{e}}{2}\mu K^1 & 0 & \frac{\bar{e}}{4}K^2 + \frac{3}{16}\bar{e}\mu^2 K^0 \end{bmatrix}.$$

A.6 Φ Matrices

$$\mathbf{\Phi}_\mathbf{a} = \begin{bmatrix} 0 & 0 & 0 \\ 0 & \frac{\bar{e}}{2}m^*_{\ddot{a}} & 0 \\ 0 & 0 & -\frac{\bar{e}}{2}m^*_{\ddot{a}} \end{bmatrix}, \quad \mathbf{\Phi}_{\dot{\mathbf{a}}} = \begin{bmatrix} 0 & 0 & 0 \\ 0 & 0 & -\bar{e}m^*_{\ddot{a}} \\ 0 & -\bar{e}m^*_{\ddot{a}} & 0 \end{bmatrix},$$

$$\mathbf{\Phi}_{\ddot{\mathbf{a}}} = \begin{bmatrix} m^*_{\ddot{a}} & 0 & 0 \\ 0 & -\frac{\bar{e}}{2}m^*_{\ddot{a}} & 0 \\ 0 & 0 & \frac{\bar{e}}{2}m^*_{\ddot{a}} \end{bmatrix}, \quad \mathbf{\Phi}_{\theta_\mathbf{r}} = \begin{bmatrix} 0 & 0 & 0 \\ 0 & \frac{\bar{e}}{2}m^*_{\ddot{\theta}_r} & 0 \\ 0 & 0 & -\frac{\bar{e}}{2}m^*_{\ddot{\theta}_r} \end{bmatrix},$$

$$\mathbf{\Phi}_{\dot{\theta}_\mathbf{r}} = \begin{bmatrix} 0 & 0 & 0 \\ 0 & 0 & -\bar{e}m^*_{\ddot{\theta}_r} \\ 0 & -\bar{e}m^*_{\ddot{\theta}_r} & 0 \end{bmatrix}, \quad \mathbf{\Phi}_{\ddot{\theta}_\mathbf{r}} = \begin{bmatrix} m^*_{\ddot{\theta}_r} & 0 & 0 \\ 0 & -\frac{\bar{e}}{2}m^*_{\ddot{\theta}_r} & 0 \\ 0 & 0 & \frac{\bar{e}}{2}m^*_{\ddot{\theta}_r} \end{bmatrix}.$$

Appendix B

Multi-Blade Coordinates

The following description of the multi-blade coornidates was also used by Garcia [7]. It is taken directly from Reference 4, and is included here for completeness.

In general, the dynamics of a rotor system are periodic, but the evaluation of continuous frequency response functions requires a linear time-invariant (LTI) assumption. Using multi-blade coordinates (MBC), an LTI approximation of the rotor dynamics will be derived. The mathematics involved in transforming the blade's degrees of freedom in the rotating frame to the rotor disk modes in the non-rotating frame are presented in this section. A more formal treatment of multi-blade coordinates is given in Johnson [11].

Using the discrete Fourier series, one can fit a periodic function at several discrete points. In the case of a helicopter rotor, these points are the azimuthal blade locations. Multi-blade coordinates use the N lowest Fourier coefficients to transform from rotor blade degrees of freedom in the rotating frame to rotor disk modes in the fixed frame. The total number of degrees of freedom are maintained, because there is a degree of freedom for each of the N blades. For example, the flap angles of the rotor blades are β_1, β_2, $\ldots \beta_{\mathrm{N}}$. The blade angles are transformed by the discrete Fourier series to the fixed frame coefficients β_0, $\beta_{1\mathrm{c}}$, $\beta_{1\mathrm{s}}$, $\ldots \beta_{\mathrm{d}}$, which represent flapping modes of the

rotor disk. The fixed frame coefficients are

$$\beta_0 = \frac{1}{\mathrm{N}} \sum_{q=1}^{\mathrm{N}} \beta(\psi_q) \ , \tag{B.1}$$

$$\beta_{nc} = \frac{2}{\mathrm{N}} \sum_{q=1}^{\mathrm{N}} \beta(\psi_q) \cos(n\psi_q) \ , \quad (n < \mathrm{N}/2) \tag{B.2}$$

$$\beta_{ns} = \frac{2}{\mathrm{N}} \sum_{q=1}^{\mathrm{N}} \beta(\psi_q) \sin(n\psi_q) \ , \quad (n < \mathrm{N}/2) \tag{B.3}$$

$$\beta_{\mathrm{d}} = \frac{1}{\mathrm{N}} \sum_{q=1}^{\mathrm{N}} \beta(\psi_q)(-1)^q \ , \quad (\mathrm{N \ \ even}) \ . \tag{B.4}$$

The coefficients β_0, β_{nc}, β_{ns}, and β_{d} are the multi-blade coordinates, and ψ_q is the azimuthal position of the qth blade ($1 \leq q \leq \mathrm{N}$). The differential term β_{d} exists only when there are an even number of blades. For the purpose of this research, we will retain only the first three multi-blade coordinates. The remaining differential terms represent reactionless modes which cause no net hub force or moment. Therefore, the MBC expansion of the flapping angle will be given by

$$\beta(\psi) = \beta_0 + \beta_c \cos\psi + \beta_s \sin\psi \ . \tag{B.5}$$

It is also assumed that all of the rotor blades behave identically. Figure B-1 illustrates the transformation from the rotating frame flapping angle, β, to the rotor disk modes, β_0, β_c, and β_s. The *coning* mode is represented by the collective coordinate β_0. The *longitudinal* and *lateral tilt* modes are represented by the cyclic coordinates β_c and β_s, respectively. Two methods for performing the MBC transformation include the substitution method and the summation operator method, which are discussed below. The substitution method will be used to transform differential equations in the rotating frame to MBC. In this work, the governing equations of motion in the rotating frame will have constant coefficients. The MBC expansion for the degree of freedom is substituted into the rotating frame equation. As an example, an equation of the form

$$m\ddot{x} + kx = f \tag{B.6}$$

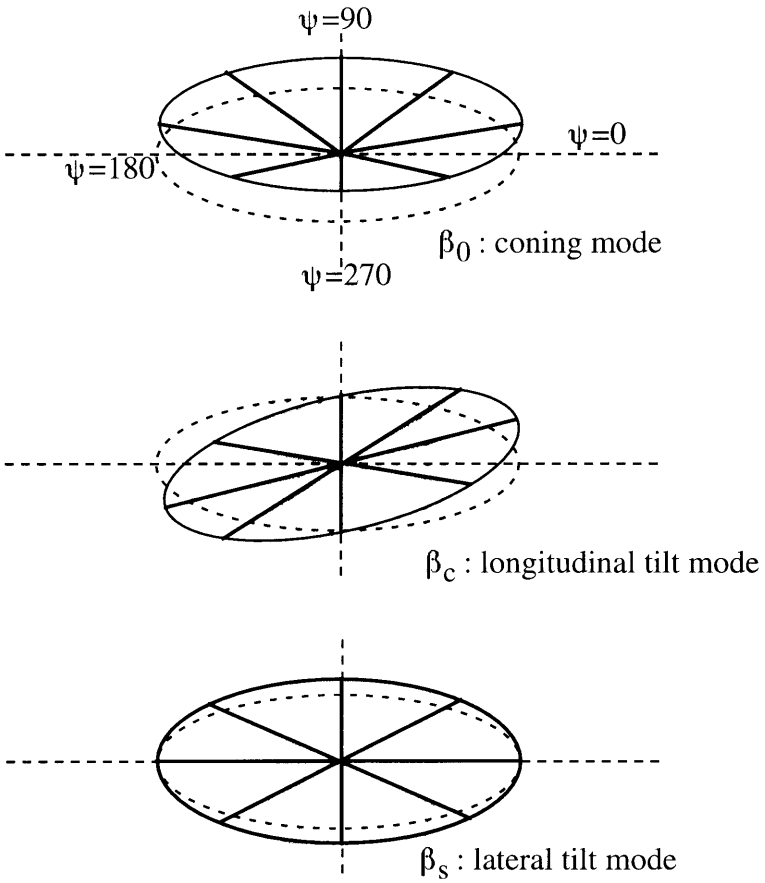

Figure B-1: MBC transformation from rigid flapping angle to rotor disk modes

will represent the dynamics of x in the rotating frame. Taking derivatives with respect to non-dimensional time ($\psi = \Omega t$), the degree of freedom x is expanded as

$$x = x_0 + x_c \cos\psi + x_s \sin\psi \,, \tag{B.7}$$

$$\dot{x} = \dot{x}_0 + \dot{x}_c \cos\psi + \dot{x}_s \sin\psi - x_c \sin\psi + x_s \cos\psi \,, \tag{B.8}$$

$$\ddot{x} = \ddot{x}_0 + \ddot{x}_c \cos\psi + \ddot{x}_s \sin\psi - 2\dot{x}_c \sin\psi + 2\dot{x}_s \cos\psi - x_c \cos\psi - x_s \sin\psi \,. \tag{B.9}$$

Inserting these into Equation (B.6) and collecting coefficients of similar terms, the

resulting equations of motion in MBC matrix form are

$$\begin{bmatrix} m & 0 & 0 \\ 0 & m & 0 \\ 0 & 0 & m \end{bmatrix} \begin{Bmatrix} \ddot{x}_0 \\ \ddot{x}_c \\ \ddot{x}_s \end{Bmatrix} + \begin{bmatrix} 0 & 0 & 0 \\ 0 & 0 & 2m \\ 0 & -2m & 0 \end{bmatrix} \begin{Bmatrix} \dot{x}_0 \\ \dot{x}_c \\ \dot{x}_s \end{Bmatrix} + \begin{bmatrix} k & 0 & 0 \\ 0 & k-m & 0 \\ 0 & 0 & k-m \end{bmatrix} \begin{Bmatrix} x_0 \\ x_c \\ x_s \end{Bmatrix} = \begin{Bmatrix} f_0 \\ f_c \\ f_s \end{Bmatrix} . \tag{B.10}$$

In addition to the substitution method, summation operators will be used to transform generalized forces on the blades to forces on the rotor disk modes. The operators are

$$(\cdot)_0 = \frac{1}{\mathrm{N}} \sum_{q=1}^{\mathrm{N}} (\cdot) , \tag{B.11}$$

$$(\cdot)_c = \frac{2}{\mathrm{N}} \sum_{q=1}^{\mathrm{N}} (\cdot) \cos(\psi_q) , \tag{B.12}$$

$$(\cdot)_s = \frac{2}{\mathrm{N}} \sum_{q=1}^{\mathrm{N}} (\cdot) \sin(\psi_q) . \tag{B.13}$$

In general, the rotating frame forces on the blades are periodic aerodynamic loads due to the azimuthally varying velocity field. As an example, the summation operators will be applied to a forcing term of the form

$$f = (1 + \mu \sin\psi)^2 x . \tag{B.14}$$

Using trigonometric identities and inserting the MBC expansion for x, Equation (B.14) is rewritten as

$$\begin{aligned} f = & \left(1 + \frac{1}{2}\mu^2 + 2\mu \sin\psi - \frac{1}{2}\mu^2 \cos 2\psi\right) x_0 + \\ & \left((1 + \frac{1}{4}\mu^2) \cos\psi + \mu \sin 2\psi - \frac{1}{4}\mu^2 \cos 3\psi\right) x_c + \\ & \left(\mu + (1 + \frac{3}{4}\mu^2) \sin\psi - \mu \cos 2\psi - \frac{1}{4}\mu^2 \sin 3\psi\right) x_s . \end{aligned} \tag{B.15}$$

Assuming a three-bladed rotor (N = 3), the summation operators yield

$$f_0 = (1 + \frac{1}{2}\mu^2)x_0 - (\frac{1}{2}\mu^2 \cos 3\psi)x_c + (\mu - \frac{1}{4}\mu^2 \sin 3\psi)x_s \ , \tag{B.16}$$

$$f_c = (-\frac{1}{2}\mu^2 \cos 3\psi)x_0 + (1 + \frac{1}{4}\mu^2)x_c - (\mu \cos 3\psi)x_s \ , \tag{B.17}$$

$$f_s = (2\mu - \frac{1}{2}\mu^2 \sin 3\psi)x_0 - (\mu \cos 3\psi)x_c + (1 + \frac{3}{4}\mu^2 - \mu \sin 3\psi)x_s \ . \tag{B.18}$$

Neglecting the periodic coefficients, the MBC forcing vector is

$$\begin{Bmatrix} f_0 \\ f_c \\ f_s \end{Bmatrix} = \begin{bmatrix} (1 + \frac{1}{2}\mu^2) & 0 & \mu \\ 0 & (1 + \frac{1}{4}\mu^2) & 0 \\ 2\mu & 0 & (1 + \frac{3}{4}\mu^2) \end{bmatrix} \begin{Bmatrix} x_0 \\ x_c \\ x_s \end{Bmatrix} \ . \tag{B.19}$$

For an N-bladed rotor, only N/rev harmonic coefficients will appear in the forcing terms when the summation operators are applied. As N increases, the periodic coefficients are swept upward in frequency and become smaller in magnitude, leaving the first collective and cyclic components to dominate the response. In general, these N/rev periodic coefficients are on the order of μ^2 and may be neglected yielding a linear time invariant approximation for the rotor dynamics. This constant coefficient approximation improves with decreasing advance ratio, μ, and increasing number of blades. For the limiting cases of a rotor in hover or a rotor with an infinite number of blades, this constant coefficient model is exact.

Using the three degree of freedom MBC expansion of Equation (B.7), all inputs, outputs, and state variables will contain terms with factors 1, $\cos\psi$, and $\sin\psi$. The rotor controls will be expressed in terms of collective and cyclic inputs. The hub load outputs will be the thrust, pitching moment, and rolling moment. Furthermore, any internal state variables will have collective and cyclic components. Unless otherwise noted, vector notation will be used to represent the MBC expansion. For example, the MBC vector for the flapping angle is

$$\boldsymbol{\beta} = \begin{Bmatrix} \beta_0 \\ \beta_c \\ \beta_s \end{Bmatrix} \ . \tag{B.20}$$

Appendix C

Inflow Dynamics

This inflow model was also used by Garcia [7]. The following description is taken directly from Reference 4, and is included here for completeness.

The inflow dynamics to be used in this model are based on that of Pitt and Peters [17]. It is a linear unsteady theory derived from actuator disk theory, that relates transient rotor loads to induced flow field response. The induced flow is expressed as

$$\lambda = \lambda_0 + \lambda_c \bar{r} \cos\psi + \lambda_s \bar{r} \sin\psi \ , \tag{C.1}$$

where λ_0, λ_c, and λ_s are the magnitudes of the uniform, fore-to-aft, and side-to-side variations in induced flow, respectively. The induced flow distributions are related to the perturbations in thrust, pitch moment, and roll moment by the linear first-order relation

$$\left[\mathcal{M} \right] \left\{ \begin{array}{c} \dot{\lambda}_0 \\ \dot{\lambda}_c \\ \dot{\lambda}_s \end{array} \right\} + \left[\mathcal{L} \right]^{-1} \left\{ \begin{array}{c} \lambda_0 \\ \lambda_c \\ \lambda_s \end{array} \right\} = \left\{ \begin{array}{c} C_T \\ C_M \\ C_L \end{array} \right\}_{\text{aero}} \ , \tag{C.2}$$

where the x-axis is positive aft, the y-axis is positive starboard, and the z-axis is positive upward. (Note that the order and orientation of these loads differ slightly from that of Pitt and Peters.) The $\mathcal{L}$ and $\mathcal{M}$ matrices have been solved in closed form in Reference [17]. With appropriate modifications for the new orientation, the

$\mathcal{L}$ and $\mathcal{M}$ matrices are

$$\mathcal{L} = \frac{1}{v_P} \begin{bmatrix} \frac{1}{2} & \frac{15\pi}{64}\sqrt{\frac{1-\sin\alpha_d}{1+\sin\alpha_d}} & 0 \\ \frac{15\pi}{64}\sqrt{\frac{1-\sin\alpha_d}{1+\sin\alpha_d}} & \frac{-4\sin\alpha_d}{1+\sin\alpha_d} & 0 \\ 0 & 0 & \frac{4}{1+\sin\alpha_d} \end{bmatrix} , \tag{C.3}$$

$$\mathcal{M} = \begin{bmatrix} \frac{128}{75\pi} & 0 & 0 \\ 0 & \frac{-16}{45\pi} & 0 \\ 0 & 0 & \frac{16}{45\pi} \end{bmatrix} , \tag{C.4}$$

respectively, where α_d is the angle of the rotor disk with respect to the free stream velocity. The mass flow parameter for the steady lift case is

$$v_P = \frac{\mu^2 + (\lambda_f + \lambda_i)(\lambda_f + 2\lambda_i)}{\sqrt{\mu^2 + (\lambda_f + \lambda_i)^2}} . \tag{C.5}$$

If the helicopter is in axial flight, the induced inflow ratio may be approximated by momentum theory [11, pg.52] as

$$\lambda_i = \frac{\lambda_c}{2} + \sqrt{(\frac{\lambda_c}{2})^2 + \frac{C_T}{2}} , \tag{C.6}$$

where λ_c is the vertical climb velocity. Note that in hover, $\lambda_c = 0$, and

$$\lambda_i = \sqrt{\frac{C_T}{2}} . \tag{C.7}$$

If the helicopter is flying at some angle of incidence, then the induced inflow velocity is governed by the equations

$$\lambda_i = \frac{C_T}{2\sqrt{\mu^2 + \lambda^2}} , \tag{C.8}$$

and

$$\lambda = \mu \tan\alpha_d + \lambda_i , \tag{C.9}$$

which may be solved iteratively. If an initial inflow is assumed, so that

$$\lambda = \mu \tan \alpha_d + \frac{C_T}{2\sqrt{\mu^2 + \frac{C_T}{2}}} , \tag{C.10}$$

the solution will converge after several iterations [11, pg. 61]. Pitt and Peters have shown that in axial flight, the inflow gains are identical to those obtained from simple momentum theory, and are independent of the radial lift distribution.

Appendix D

Listing of Matlab Code

The following is a listing of the Matlab `*.m` files which construct the State Space Rotor Model. These routines were originally written for Matlab Version 4.2. To create the state space matrices $\boldsymbol{A}$, $\boldsymbol{B}$, $\boldsymbol{C}$, and $\boldsymbol{D}$ simply type `modalmodel` at the Matlab prompt.

```
%=========================================================
% modalmodel.m
%=========================================================
%
% This is the main program that runs the modal superpostion analysis.
inflag=1
d3flag=0
cgflag=1

%h34property
SSRCboeing

modalspthr;
KL0=zeros(size(KL0));

modalintthr;
modalmat3thr;
modalstatethr2;
modalout2;
```

```
%============================================================
% h34property.m            input file of H34 rotor model
%============================================================
m=[3.5700e-02   8.9997e+00
   3.5800e-02   6.5701e+00
   9.0000e-02   1.0304e+00
   1.3000e-01   3.5417e-01
   1.7000e-01   4.0000e-01
   2.1000e-01   4.5318e-01
   2.7000e-01   5.0000e-01
   3.2500e-01   5.0000e-01
   3.7500e-01   5.0000e-01
   4.2500e-01   5.0000e-01
   4.7500e-01   5.0000e-01
   5.2500e-01   5.0000e-01
   5.7500e-01   5.0000e-01
   6.2500e-01   5.0000e-01
   6.8000e-01   5.0000e-01
   7.3000e-01   4.9999e-01
   7.7000e-01   4.9999e-01
   8.0500e-01   4.9998e-01
   8.3750e-01   4.9997e-01
   8.6250e-01   5.0002e-01
   8.8750e-01   4.9997e-01
   9.1250e-01   4.9998e-01
   9.4000e-01   6.1427e-01
   9.6000e-01   8.0000e-01
   9.8000e-01   4.8455e-01
   1.0000e+00   4.8455e-01];
Icg=[3.5700e-02   1.0365e+02
   3.5800e-02   4.1462e+01
   9.0000e-02   6.8540e+00
   1.3000e-01   2.5760e+00
   1.7000e-01   4.2504e+00
   2.1000e-01   5.2237e+00
   2.7000e-01   5.7960e+00
   3.2500e-01   5.7960e+00
   3.7500e-01   5.7960e+00
   4.2500e-01   5.7960e+00
   4.7500e-01   5.7960e+00
   5.2500e-01   5.7960e+00
   5.7500e-01   5.7960e+00
   6.2500e-01   5.7960e+00
   6.8000e-01   5.7960e+00
   7.3000e-01   5.7960e+00
```

```
   7.7000e-01   5.7960e+00
   8.0500e-01   5.7960e+00
   8.3750e-01   5.7960e+00
   8.6250e-01   5.7960e+00
   8.8750e-01   5.7960e+00
   9.1250e-01   5.7960e+00
   9.4000e-01   5.7960e+00
   9.6000e-01   9.4392e+00
   9.8000e-01   8.3634e+00
   1.0000e+00   8.3634e+00];
GJ=[3.5700e-02   1.1900e+08
   3.5800e-02   1.1900e+08
   9.0000e-02   5.8712e+07
   1.3000e-01   2.4891e+07
   1.7000e-01   2.0566e+07
   2.1000e-01   1.8960e+07
   2.7000e-01   1.8000e+07
   3.2500e-01   1.8000e+07
   3.7500e-01   1.8000e+07
   4.2500e-01   1.8000e+07
   4.7500e-01   1.8000e+07
   5.2500e-01   1.8000e+07
   5.7500e-01   1.8000e+07
   6.2500e-01   1.8000e+07
   6.8000e-01   1.8000e+07
   7.3000e-01   1.8000e+07
   7.7000e-01   1.8000e+07
   8.0500e-01   1.8000e+07
   8.3750e-01   1.8000e+07
   8.6250e-01   1.8000e+07
   8.8750e-01   1.8000e+07
   9.1250e-01   1.8000e+07
   9.4000e-01   1.8000e+07
   9.6000e-01   1.8000e+07
   9.8000e-01   1.8000e+07
   1.0000e+00   1.8000e+07];
GJ(:,2)=GJ(:,2)*1.06;     % places w_1 at 7.6/rev
%GJ(:,2)=GJ(:,2)*0.347;     % places w_1 at 4.5/rev
EI=[3.5700e-02    1.0000e14;
    1.0000e+00    1.0000e14];
shear=[3.5700e-02  0;
       1.0000e+00  0];
cg=[3.5700e-02   0;
    1.0000e+00   0];
%==================servoflap size & location=================
```

```
r1bar = 0.6000;          % inboard servoflap location
r2bar = 0.8000;          % outboard servoflap location
%====================inputs==================================
a=6.3025;                %lift curve slope
alphad=90.0;             %rotor shaft angle (0 deg is edgewise flight)
                         %                  (90 deg is axial flight)
R=28*12;                 % rotor radius in inches
omega_rpm=222;          %rotor rotational velocity(RPM)
omega=omega_rpm*2*pi/60;%(radian/sec)
nomega=222;              %rpm used for normalizing frequencies.
rho=.002195;             %density of air
cbar = 16.4/R;           %blade chord, c/R
ebar = 0.0357;           %hinge offset
rcut = 0.210;            %root cutout
Btip = 1;                %tip loss factor
nbar = 0.5;              %normalized lift coeff. of servoflap; Re=4,080,000.
pbar = -0.082;          %normalized moment coeff. of servoflap, Cm-eta/a;
mu = 0                   %advance ratio
CTsig = 0.1;             %blade loading
Q = 4;                   %number of blades
kth=0;                   %pitch link stiffness (lbf-in/rad)
d3_deg=0;                %delta3 hinge angle in degrees
d3=d3_deg*pi/180;        % in rad.
```

```
%============================================================
% modalspthr.m              Finite element model
%============================================================
% This program uses technic of modal superpostion to find modal mass
% and modal stiffness matrices.

% create spanwise station vector which covers all
% points given in blade properties.
r=m(:,1);
r=unify(r,Icg);
r=unify(r,EI);
r=unify(r,GJ);
r=unify(r,cg);
r=unify(r,shear);
% create property vectors for m, Icg, EI, GJ, shear, Cg, based on r.
m=prop2r(m,r);
Icg=prop2r(Icg,r);
EI=prop2r(EI,r);
GJ=prop2r(GJ,r);
shear=prop2r(shear,r);
Cg=prop2r(cg,r);
[z,t]=size(r);
%=============find number of elements across span==============
temp=0;
for i=1:z-1
   if r(i)==r(i+1)
      temp=temp+1;
   end
end
N=z-temp-1;                    %number of elements across span
%=========================other stuff=========================
Kp=tan(d3);
h=(r(2:z)-r(1:z-1));           %[ND]
e=(Cg-shear)*cgflag;           %[in]
nm=9;                          %number of modes
%============convert properties to desired units.=================
GJ=GJ*12;                      %[slug-in/(sec^2) -in^2]
EI=EI*12;                      %[slug-in/(sec^2) -in^2]
mass=m/32.2;                   %[slug/(in span)]
Icg=Icg/32.2;                  %[slug-in^2/(in span)]
kth=kth*12;                    %[slug-in/(sec^2) -in]
%====================Locke Number=========================
for i=1:z-1
   masslump(i)=(mass(i)+mass(i+1))*0.5*h(i)*R;
end
```

```
rlump=R*(r(1:z-1)+r(2:z))/2;
Ib=sum(masslump'.*rlump.*rlump)/144;       %slug-ft^2
gamma = rho*a*cbar*(R/12)^5/Ib;
%==============Values calculated from input==================
alpha = alphad*pi/180;              % [radians]
mus= mu^2;                          % mu squared
cbars = cbar^2;                     % cbar squared
sigma = Q*cbar/pi;                  % solidity
Cthrust = sigma*CTsig;              % thrust coefficient
%======================== velocity ratios ======================
if (alphad==90)                     % Axial Flight
vbar = mu;   % free stream velocity ratio
 lamf = vbar;                       % free stream inflow ratio
 if (vbar==0)                       % Hover Case
  lami = sqrt(Cthrust/2);           % induced velocity ratio
  lam = lamf + lami;
 else                               % Axial Vertical Flight
  lami = vbar/2 +sqrt((vbar/2)^2+Cthrust/2);
  lam = lamf + lami;
 end;
else                                % Forward Flight
 vbar = mu/cos(alpha);              % free stream velocity ratio
 lamf = mu*tan(alpha);              % free stream inflow ratio
 lamold = lamf + Cthrust/(2*sqrt(mus+Cthrust/2));
 error = 1;
% iterate to find inflow
 while abs(error) > .00001
  lami = Cthrust/(2*sqrt(mus+lamold^2));
  lam = lamf + lami;
  error = lam -lamold;
  lamold = lam;
 end
end
%==============find tension, T(r), across span=================
T(z)=0;
for i=z-1:-1:1
   T(i)=T(i+1)+(mass(i+1)+mass(i))*0.5*r(i)*R^2*omega^2*h(i);
end
T=T';
%==============Non Dimensionalizing the entries============
Ib=Ib*144;     %slug-in^2
masss=mass*R^3/Ib;
Icgg=Icg*R/Ib;
ee=e/R;
GJJ=GJ/(Ib*R*omega^2);
```

```
EII=EI/(Ib*R*omega^2);
TT=T*R/(Ib*omega^2);
kthh=kth/(Ib*omega^2);
%==============Do Finite Element Code=========================
BK=zeros(N*3+3,N*3+3);          %Big K!
BM=BK;                          %Big M!
j=1;
for i=1:z-1
   if r(i) ~= r(i+1)
      rr(j)=r(i);
      m1=masss(i);
      m2=masss(i+1);
      I1=Icgg(i);
      I2=Icgg(i+1);
      gj1=GJJ(i);
      gj2=GJJ(i+1);
      ei1=EII(i);
      ei2=EII(i+1);
      ee1=ee(i);
      ee2=ee(i+1);
      ten1=TT(i);
      ten2=TT(i+1);
      hhr=h(i);
      FE_subexact(m1,m2,I1,I2,gj1,gj2,ei1,ei2,ee1,ee2,ten1,ten2,hhr);
      K=ans(1:6,1:6);
      M=ans(7:12,1:6);
      Ktemp=zeros(size(BK));
      Ktemp(3*(j-1)+1:3*(j-1)+6,3*(j-1)+1:3*(j-1)+6)=K;
      BK=BK+Ktemp;
      Mtemp=zeros(size(BM));
      Mtemp(3*(j-1)+1:3*(j-1)+6,3*(j-1)+1:3*(j-1)+6)=M;
      BM=BM+Mtemp;
   j=j+1;
   end
end
rr(j)=r(z);
hh=(rr(2:N+1)-rr(1:N))';
clear I1 I2 gj1 gj2 ee1 ee2 ei1 ei2 ten1 ten2 m1 m2 cg
clear masss Icgg EII GJJ ee TT
cg=e*cgflag;
%
% add boundary conditions
%
% deflection at r(1) is zero;==>remove row/column 2
BKt(1,1)=BK(1,1);
```

```
BMt(1,1)=BM(1,1);
BKt(1,2:3*N+2)=BK(1,3:3*N+3);
BKt(2:3*N+2,1)=BK(3:3*N+3,1);
BMt(1,2:3*N+2)=BM(1,3:3*N+3);
BMt(2:3*N+2,1)=BM(3:3*N+3,1);
BKt(2:3*N+2,2:3*N+2)=BK(3:3*N+3,3:3*N+3);
BMt(2:3*N+2,2:3*N+2)=BM(3:3*N+3,3:3*N+3);
clear BM BK
BK=BKt;
BM=BMt;
%
% Effect of delta3 hinge and pitch link stiffness
%
D=[cos(d3) sin(d3)];
BK([3 5],[3 5])=BK([3 5],[3 5])+D'*kthh*D;
%========eigen values, then natural frequencies===============
mMK=inv(BM)*BK;
[V,wks]=eig(mMK);
wks=diag(wks);
[wk,t]=sort(sqrt(wks));
V=V(:,t);
wk=wk(1:nm);
clear K M Ktemp Mtemp BMt BKt mMK wks t mode modet modew modeb
%============mode shapes=====================================
for i=1:nm
  modet(1,i)=V(1,i);
  modet(2:N+1,i)=V(3:3:3*N+2,i);
  modew(1,i)=0;
  modew(2:N+1,i)=V(4:3:3*N+2,i);
  modeb(1,i)=V(2,i);
  modeb(2:N+1,i)=V(5:3:3*N+2,i);
  modet(:,i)=modet(:,i);
  modew(:,i)=modew(:,i);
end
moder=1*ones(N+1,1);
mode(1,:)=modet(1,:);
mode(2,:)=modeb(1,:);
mode(3:3:3*N+2,:)=modet(2:N+1,:);
mode(4:3:3*N+2,:)=modew(2:N+1,:);
mode(5:3:3*N+2,:)=modeb(2:N+1,:);
modex=zeros(3*N+2,nm+1);
modex(1,1)=moder(1);
modex(3:3:3*N+2,1)=moder(2:N+1,1);
modex(1:3*N+2,2:nm+1)=mode;
clear mode
```

```
mode=modex;
clear modex
%===========Modal Mass/Stiffness Matrices====================
clear Mbar Kbar
Mbar=mode'*BM*mode;
Kbar=mode'*BK*mode;

clear BM BK V kthh hhr;

M00=Mbar(1,1);
M0L=Mbar(1,2:nm+1);
ML0=Mbar(2:nm+1,1);
MLL=Mbar(2:nm+1,2:nm+1);
K00=Kbar(1,1);
K0L=Kbar(1,2:nm+1);
KL0=Kbar(2:nm+1,1);
KLL=Kbar(2:nm+1,2:nm+1);
clear Kbar Mbar
```

```
%============================================================
% modalintthr.m           does trapazoidal integrations
%============================================================
% (Garcia's trapint-way to do integrations)
%
% This program uses technic of modal superposition to find the
% modal forces and modal moments and all the other variables
% using Trapazoidal integrations.

%% STRUCTURAL INTEGRATIONS %%
numpts=(1-ebar)*1000+1;
dr = (1-ebar)/(numpts-1);
sumvec = [.5 ones(1,(numpts-2)) .5];
rbar=ebar*ones(numpts,1)+(1-ebar)*(0:(numpts-1))'/(numpts-1);

% spread the properties across the span ---> more spanwise stations
for i=1:nm
  twist(:,i)=span(modet(:,i),rr,numpts,ebar);
  flap(:,i)=span(modew(:,i),rr,numpts,ebar);
  slope(:,i)=span(modeb(:,i),rr,numpts,ebar);
end
rtwist=span(moder,rr,numpts,ebar);
massvec=span(mass,r,numpts,ebar);
cgvec=span(cg,r,numpts,ebar);
for m=1:nm
  madds(m)=sumvec*(massvec.*cgvec.*twist(:,m)-massvec.*flap(:,m)*R);
  madds(m)=madds(m)*dr*R^2*a*sigma/(gamma*Ib);
end
mtrdds=sumvec*(massvec.*cgvec.*rtwist)*dr*R^2*a*sigma/(gamma*Ib);

%% AERODYNAMIC INTEGRATIONS %%
rcutind = (rcut - ebar)*numpts/(1-ebar) + 1;
Bind = (Btip - ebar)*numpts/(1-ebar);
sumveca = [.5 sumvec(rcutind+1:Bind-1) .5];
rbara=rbar(rcutind:Bind);
artwist=rtwist(rcutind:Bind);
for m=1:nm
  aflap=flap(rcutind:Bind,m);
  atwist=twist(rcutind:Bind,m);
  aslope=slope(rcutind:Bind,m);
  for n=1:nm
    twista=twist(rcutind:Bind,n);
    flapa=flap(rcutind:Bind,n);
    slopea=slope(rcutind:Bind,n);
    A0(m,n)=sumveca*(twista.*aflap)*dr*gamma/2;
```

```
    A1(m,n)=sumveca*(rbara.*twista.*aflap)*dr*gamma/2;
    A2(m,n)=sumveca*(rbara.*rbara.*twista.*aflap)*dr*gamma/2;
    B0(m,n)=-sumveca*(slopea.*aflap)*dr*gamma/2;
    B1(m,n)=-sumveca*(rbara.*slopea.*aflap)*dr*gamma/2;
    C0(m,n)=-sumveca*(flapa.*aflap)*dr*gamma/2;
    C1(m,n)=-sumveca*(rbara.*flapa.*aflap)*dr*gamma/2;
    M0(m,n)=-sumveca*(atwist.*twista)*dr*(cbar/4)^2*gamma;
    M1(m,n)=-sumveca*(rbara.*atwist.*twista)*dr*(cbar/4)^2*gamma;
  end
  N0(m)=-sumveca*(atwist.*artwist)*dr*(cbar/4)^2*gamma;
  N1(m)=-sumveca*(rbara.*atwist.*artwist)*dr*(cbar/4)^2*gamma;
  D0(m)=sumveca*(aflap)*dr*gamma/2;
  D1(m)=sumveca*(rbara.*aflap)*dr*gamma/2;
  D2(m)=sumveca*(rbara.*rbara.*aflap)*dr*gamma/2;
  S0(m)=sumveca*(artwist.*aflap)*dr*gamma/2;
  S1(m)=sumveca*(rbara.*artwist.*aflap)*dr*gamma/2;
  S2(m)=sumveca*(rbara.*rbara.*artwist.*aflap)*dr*gamma/2;
  G0(m)=sumveca*(atwist)*dr*a*sigma;
  G1(m)=sumveca*(rbara.*atwist)*dr*a*sigma;
  G2(m)=sumveca*(rbara.*rbara.*atwist)*dr*a*sigma;
  H0(m)=-sumveca*(aslope)*dr*sigma*a;
  H1(m)=-sumveca*(rbara.*aslope)*dr*sigma*a;
  J0(m)=-sumveca*(aflap)*dr*sigma*a;
  J1(m)=-sumveca*(rbara.*aflap)*dr*sigma*a;
end
F0=sumveca*(artwist)*dr*sigma*a;
F1=sumveca*(rbara.*artwist)*dr*sigma*a;
F2=sumveca*(rbara.*rbara.*artwist)*dr*sigma*a;

%% SERVO FLAP INTEGRATIONS %%
r1indx=round((r1bar-ebar)*1000+1);
r2indx=round((r2bar-ebar)*1000+1);

% check if outboard flap location is in tip loss region
if r2indx > Bind,
   r2indx = Bind;
end
sfrbar= rbar(r1indx:r2indx,1);
sfnumpts = r2indx-r1indx+1;
sfsumvec = [.5 ones(1,(sfnumpts-2)) .5];
sfrtwist=rtwist(r1indx:r2indx);
for m=1:nm
  sfflap=flap(r1indx:r2indx,m);
  sftwist=twist(r1indx:r2indx,m);
  E0(m)=sfsumvec*(sfflap)*dr*nbar*gamma/2;
```

```
  E1(m)=sfsumvec*(sfrbar.*sfflap)*dr*nbar*gamma/2;
  E2(m)=sfsumvec*(sfrbar.*sfrbar.*sfflap)*dr*nbar*gamma/2;
  L0(m)=sfsumvec*(sftwist)*dr*cbar*pbar*gamma/2;
  L1(m)=sfsumvec*(sfrbar.*sftwist)*dr*cbar*pbar*gamma/2;
  L2(m)=sfsumvec*(sfrbar.*sfrbar.*sftwist)*dr*cbar*pbar*gamma/2;
end
K0=sfsumvec*(ones(size(sfrbar)))*dr*nbar*a*sigma;
K1=sfsumvec*(sfrbar)*dr*nbar*a*sigma;
K2=sfsumvec*(sfrbar.*sfrbar)*dr*nbar*a*sigma;

clear numpts r1indx r2indx sfrbar sfnumpts sfsumvec sfrtwist
clear aflap sfflap flapa aslope slopea sftwist atwist twista
clear massvec sfsumvec sumvec sumveca flap twist slope
```

```
%=========================================================
% modalmat3thr.m      construction of all matrices
%=========================================================
%
% This program builds all the necessary matrices
% that are required for modal superpostion analysis.
%
% matrix names
%
%  D = Delta:structural matrices by finite element model
%  L = modal force due to lifting
%  M = modal force due to moment
%  G = gamma:modified aerodynamics matrices(minus inertia)
%  P = phi: inertia terms
%  Ps= Psi: terms from finite element code

%% Initialize all the matrices %%
D_add=zeros(3*nm,3*nm);
D_ad=zeros(3*nm,3*nm);
D_a=zeros(3*nm,3*nm);
L_a=zeros(3*nm,3*nm);
L_ad=zeros(3*nm,3*nm);
L_thr=zeros(3*nm,3);
L_l=zeros(3*nm,3);
L_e=zeros(3*nm,3);
M_e=zeros(3*nm,3);
M_a=zeros(3*nm,3*nm);
M_ad=zeros(3*nm,3*nm);
M_thr=zeros(3*nm,3);
M_thrd=zeros(3*nm,3);
G_a=zeros(3,3*nm);
G_ad=zeros(3,3*nm);
G_l=zeros(3,3);
G_e=zeros(3,3);
G_thr=zeros(3,3);
P_add=zeros(3,3*nm);
P_ad=zeros(3,3*nm);
P_a=zeros(3,3*nm);
P_thr=zeros(3,3);
P_thrd=zeros(3,3);
P_thrdd=zeros(3,3);
Ps_thrdd=zeros(3*nm,3);
Ps_thrd=zeros(3*nm,3);
Ps_thr=zeros(3*nm,3);
```

```
D_add(1:nm,1:nm)=MLL;
D_add(nm+1:2*nm,nm+1:2*nm)=MLL;
D_add(2*nm+1:3*nm,2*nm+1:3*nm)=MLL;
D_ad(nm+1:2*nm,2*nm+1:3*nm)=2*MLL;
D_ad(2*nm+1:3*nm,nm+1:2*nm)=-2*MLL;
D_a(1:nm,1:nm)=KLL;
D_a(nm+1:2*nm,nm+1:2*nm)=KLL-MLL;
D_a(2*nm+1:3*nm,2*nm+1:3*nm)=KLL-MLL;

Ps_thrdd(1:nm,1)=ML0;
Ps_thrdd(nm+1:2*nm,2)=ML0;
Ps_thrdd(2*nm+1:3*nm,3)=ML0;
Ps_thrd(nm+1:2*nm,3)=2*ML0;
Ps_thrd(2*nm+1:3*nm,2)=-2*ML0;
Ps_thr(1:nm,1)=KL0;
Ps_thr(nm+1:2*nm,2)=(KL0-ML0);
Ps_thr(2*nm+1:3*nm,3)=(KL0-ML0);

for m=1:nm
  L_thr(m,1)=S2(m)+mus*S0(m)/2;
  L_thr(m,3)=mu*S1(m);
  L_thr(nm+m,2)=S2(m)+mus*S0(m)/4;
  L_thr(2*nm+m,1)=2*mu*S1(m);
  L_thr(2*nm+m,3)=S2(m)+0.75*mus*S0(m);
  for n=1:nm
     L_a(m,n)=A2(m,n)+mus*A0(m,n)/2;
     L_a(m,n+nm)=0.5*mu*(B1(m,n)-C0(m,n));
     L_a(m,2*nm+n)=mu*A1(m,n);
     L_a(nm+m,n)=mu*B1(m,n);
     L_a(nm+m,nm+n)=A2(m,n)+mus*A0(m,n)/4;
     L_a(nm+m,2*nm+n)=mus*B0(m,n)/4+C1(m,n);
     L_a(2*nm+m,n)=2*mu*A1(m,n);
     L_a(2*nm+m,nm+n)=mus*B0(m,n)/4-C1(m,n);
     L_a(2*nm+m,2*nm+n)=A2(m,n)+0.75*mus*A0(m,n);
     L_ad(m,n)=C1(m,n);
     L_ad(m,2*nm+n)=mu*C0(m,n)/2;
     L_ad(nm+m,nm+n)=C1(m,n);
     L_ad(2*nm+m,n)=mu*C0(m,n);
     L_ad(2*nm+m,2*nm+n)=C1(m,n);

     M_a(m,nm+n)=-mu*M0(m,n)/2;
     M_a(nm+m,2*nm+n)=M1(m,n);
     M_a(2*nm+m,nm+n)=-M1(m,n);
     M_ad(m,n)=M1(m,n);
     M_ad(m,2*nm+n)=mu*M0(m,n)/2;
```

```
      M_ad(nm+m,nm+n)=M1(m,n);
      M_ad(2*nm+m,n)=mu*M0(m,n);
      M_ad(2*nm+m,2*nm+n)=M1(m,n);
   end

   M_thr(m,2)=-mu*N0(m)/2;
   M_thr(nm+m,3)=N1(m);
   M_thr(2*nm+m,2)=-N1(m);
   M_thrd(m,1)=N1(m);
   M_thrd(m,3)=mu*N0(m)/2;
   M_thrd(nm+m,2)=N1(m);
   M_thrd(2*nm+m,1)=mu*N0(m);
   M_thrd(2*nm+m,3)=N1(m);

   L_e(m,1)=E2(m)+mus*E0(m)/2;
   L_e(m,3)=mu*E1(m);
   L_e(nm+m,2)=E2(m)+mus*E0(m)/4;
   L_e(2*nm+m,1)=2*mu*E1(m);
   L_e(2*nm+m,3)=E2(m)+0.75*mus*E0(m);
   L_l(m,1)=-D1(m);
   L_l(m,3)=-mu*D1(m)/2;
   L_l(nm+m,2)=-D2(m);
   L_l(2*nm+m,1)=-mu*D0(m);
   L_l(2*nm+m,3)=-D2(m);

   M_e(m,1)=L2(m)+mus*L0(m)/2;
   M_e(m,3)=mu*L1(m);
   M_e(nm+m,2)=L2(m)+mus*L0(m)/4;
   M_e(2*nm+m,1)=2*mu*L1(m);
   M_e(2*nm+m,3)=L2(m)+0.75*mus*L0(m);
   G_a(1,m)=G2(m)/2+mus*G0(m)/4;
   G_a(1,nm+m)=mu*(H1(m)-J0(m))/4;
   G_a(1,2*nm+m)=mu*G1(m)/2;
   G_a(2,m)=-ebar*mu*H1(m)/4;
   G_a(2,nm+m)=-ebar*(G2(m)/4+mus*G0(m)/16);
   G_a(2,2*nm+m)=-ebar*(J1(m)/4+mus*H0(m)/16);
   G_a(3,m)=ebar*mu*G1(m)/2;
   G_a(3,nm+m)=ebar*(mus*H0(m)/16-J1(m)/4);
   G_a(3,2*nm+m)=ebar*(G2(m)/4+3*mus*G0(m)/16);
end

G_l=[ -F1/2        0       -mu*F1/4;
        0        ebar*F2/4        0;
      -ebar*mu*F0/4    0    -ebar*F2/4];
```

```
G_e=[K2/2+mus*K0/4         0          mu*K1/2;
      0     -ebar*K2/4-ebar*mus*K0/16     0;
      ebar*mu*K1/2         0    ebar*K2/4+3*ebar*mus*K0/16];

G_thr=[F2/2+mus*F0/4        0           mu*F1/2;
        0     -ebar*F2/4-ebar*mus*F0/16     0;
        ebar*mu*F1/2        0    ebar*F2/4+3*ebar*mus*F0/16];

P_thr=[0         0         0;
       0  ebar*mtrdds/2   0;
       0         0    -ebar*mtrdds/2];

P_thrd=[0        0           0;
        0        0   -ebar*mtrdds;
        0  -ebar*mtrdds      0];

P_thrdd=[mtrdds      0          0;
          0    -ebar*mtrdds/2   0;
          0          0    ebar*mtrdds/2];

for m=1:nm
  G_ad(1,m)=J1(m)/2;
  G_ad(1,2*nm+m)=mu*J0(m)/4;
  G_ad(2,nm+m)=-ebar*J1(m)/4;
  G_ad(3,m)=ebar*mu*J0(m)/4;
  G_ad(3,2*nm+m)=ebar*J1(m)/4;

  P_add(1,m)=madds(m);
  P_add(2,nm+m)=-ebar*madds(m)/2;
  P_add(3,2*nm+m)=ebar*madds(m)/2;
  P_ad(2,2*nm+m)=-ebar*madds(m);
  P_ad(3,nm+m)=-ebar*madds(m);
  P_a(2,nm+m)=ebar*madds(m)/2;
  P_a(3,2*nm+m)=-ebar*madds(m)/2;
end
% =============== Pitt and Peters Inflow Matrices ===============
 vpeters = (mus+(lamf+lami)*(lamf+2*lami))/sqrt(mus+(lamf+lami)^2);
 if(alphad == 90)
   L_in = [(.5/vpeters) 0 0;0 (-2/vpeters) 0;0 0 (2/vpeters)];
 else
   L_in = (1/vpeters)*[.5 ...
        sign(mu)*((15*pi/64)*sqrt((1-sin(alpha))/(1+sin(alpha)))) 0;
        sign(mu)*((15*pi/64)*sqrt((1-sin(alpha))/(1+sin(alpha))))...
        ((-4*sin(alpha))/(1+sin(alpha))) 0;
        0 0 (4/(1+sin(alpha)))];
```

```
 end
Linv = inv(L_in);
M_in = [(128/(75*pi)) 0 0; 0 (-16/(45*pi)) 0; 0 0 (16/(45*pi))];
Minv = inflag*inv(M_in);
```

```
%============================================================
% modalstatethr2.m
%============================================================
%
% define state space with notations generated
% in modalmat.

Dinv=inv(D_add);
A=[zeros(3*nm) eye(3*nm) zeros(3*nm,3) zeros(3*nm,3) zeros(3*nm,3);
 Dinv*(L_a+M_a-D_a) Dinv*(L_ad+M_ad-D_ad) Dinv*L_l ...
 Dinv*(L_thr*1+M_thr-Ps_thr)  Dinv*(M_thrd-Ps_thrd)*1;
 zeros(3,3*nm)  zeros(3,3*nm) -Minv*Linv  zeros(3,3) zeros(3,3);
 zeros(3,3*nm)  zeros(3,3*nm) zeros(3,3)  zeros(3,3)   eye(3);
 zeros(3,3*nm)  zeros(3,3*nm) zeros(3,3)  zeros(3,3)   zeros(3,3);];

B=[zeros(3*nm,3)  zeros(3*nm,3);
Dinv*(-Ps_thrdd)*1  Dinv*(L_e+M_e);
zeros(3,3)  zeros(3,3);
zeros(3,3)  zeros(3,3);
eye(3)  zeros(3,3)];

C=[(G_a+P_a+P_add*Dinv*(L_a+M_a-D_a)) ...
(G_ad+P_ad+P_add*Dinv*(L_ad+M_ad-D_ad)) ...
G_l+P_add*Dinv*L_l ...
(G_thr+P_thr)+P_add*Dinv*(L_thr*1+M_thr-Ps_thr) ...
P_thrd+P_add*Dinv*(M_thrd-Ps_thrd)];

D=[P_thrdd G_e]+P_add*Dinv*[-Ps_thrdd (L_e+M_e)];


%% Modified Aerodyanamics (minus inertial terms) %%

Bl=[zeros(3*nm,3);zeros(3*nm,3);Minv;zeros(3,3);zeros(3,3)];
Ca=[G_a  G_ad  G_l G_thr zeros(3,3)];
Da=[zeros(3,3)  G_e];

% Convert radians to degrees
 rpd = pi/180;
 dpr = 180/pi;
 Ar2d = ones(size(A));
 Br2d = ones(size(B));
 Blr2d = ones(size(Bl));
 Cr2d = ones(size(C));
 Dr2d = ones(size(D));
```

```
 Ar2d(1:6*nm,6*nm+1:6*nm+3) = dpr*ones(6*nm,3);
 Ar2d(6*nm+4:6*nm+9,6*nm+1:6*nm+3) = dpr*ones(6,3);
 Ar2d(6*nm+1:6*nm+3,1:6*nm) = rpd*ones(3,6*nm);
 Ar2d(6*nm+1:6*nm+3,6*nm+4:6*nm+9) = rpd*ones(3,6);
 Br2d(6*nm+1:6*nm+3,1:6) = rpd*ones(3,6);
 Cr2d(1:3,1:6*nm) = rpd*ones(3,6*nm);
 Cr2d(1:3,6*nm+4:6*nm+9) = rpd*ones(3,6);
 Dr2d(1:3,1:6) = rpd*ones(3,6);

 A = Ar2d.*A;
 B = Br2d.*B;
 C = Cr2d.*C;
 D = Dr2d.*D;
 Ca = Cr2d.*Ca;
 Da = Dr2d.*Da;

%=================================================
% Include Options
% By zeroing out unwanted dynamics
%=================================================
% No Inflow
 if(inflag == 0);
    A(1:6*nm+9,6*nm+1:6*nm+3) = zeros(6*nm+9,3);
    A(6*nm+1:6*nm+3,1:6*nm+9) = zeros(3,6*nm+9);
    B(6*nm+1:6*nm+3,1:6) = zeros(3,6);
    C(1:3,6*nm+1:6*nm+3) = zeros(3,3);
 else;
   %================================================
   % Close aerodynamic loop
   %================================================
     A = A+Bl*Ca;
     B = B + Bl*Da;
     C = C;
     D = D;
 end;
%=================================================
```

```
%=========================================================
% modalout2.m
%=========================================================
%
% set up transfer functions

%    INPUTS: 1   collective root pitch
%            2   cosine root pitch
%            3   sine root pitch
%            4   collective servo-flap
%            5   cosine servo-flap
%            6   sine servo-flap
%    OUTPUTS:  collective tip pitch angle
%              Ct/sigma
Cmtip = zeros(3,6*nm+9);
for i=1:nm
  Cmtip(1,i) = modet(N+1,i);
  Cmtip(2,nm+i)=modet(N+1,i);
  Cmtip(3,2*nm+i)=modet(N+1,i);
end
Cmtip(1:3,6*nm+4:6*nm+6)=eye(3);
Dmtip = zeros(3,6);

[num1,den1]=ss2tf(A,B,C,D,1);
%[num2,den2]=ss2tf(A,B,C,D,2);
%[num3,den3]=ss2tf(A,B,C,D,3);
[num4,den4]=ss2tf(A,B,C,D,4);
%[num5,den5]=ss2tf(A,B,C,D,5);
%[num6,den6]=ss2tf(A,B,C,D,6);

[ntipth,dtipth]=ss2tf(A,B,Cmtip,Dmtip,1);
[ntipeta,dtipeta]=ss2tf(A,B,Cmtip,Dmtip,4);

% differentiate root pitch input
num1 = [num1 zeros(3,2)];
%num2 = [num2 zeros(3,2)];
%num3 = [num3 zeros(3,2)];
ntipth = [ntipth zeros(3,2)];
dpr = 180/pi;
%=========================================================
num11=num1(1,:);   %(CT)/collective root pitch
%num21=num2(1,:);   %(CT)/cosine root pitch
%num31=num3(1,:);   %(CT)/sine root pitch
num41=num4(1,:);   %(CT)/collective servo-flap
%num51=num5(1,:);   %(CT)/cosine servo_flap
```

```
%num61=num6(1,:);   %(CT)/sine servo_flap

%Remember to devide sigma to get CT/sigma response

ntipth=ntipth(1,:);        %blade tip angle/collective root pitch
ntipeta=ntipeta(1,:);      %blade tip angle/collective servo-flap
```

```
%=========================================================
% FE_subexact.m   subroutine for finite element code
%=========================================================
%
% This function reads in values of m, Icg, GJ, EI, e, Tension and h
% then build matrix [M] and [K].
%
%q={theta(i), theta(i+1), w(i), beta(i),w(i+1), beta(i+1)}'
% where
%      theta=torsional angle
%      w=flapping deflection
%      beta=beta=flapping angle
%      i=left side of element
%      i+1=right side of element
%
% Beware of Units
%
% GJ=slug-in/(sec^2) - in^2    {force inch square}
% EI= same as GJ
% h=length of element, in inches or meters
% e=distance between cg and shear axis, [inch]
% m=mass of element  [slug/in span]
% Icg=moment of inertia at cg [slug-in^2/in span]
%
%FE_subexact(m1,m2,I1,I2,gj1,gj2,ei1,ei2,e1,e2,t1,t2,h)

function [answer]=FE_subexact(m1,m2,I1,I2,gj1,gj2,ei1,ei2,e1,e2,t1,t2,h);

K=zeros(6,6);
M=zeros(6,6);

% Coefficients for linear properties for element between 0 & h
% property=A*x+B

% Below properties, gj,tension,ei are for K matrix only.
ag=gj2-gj1;
bg=gj1;
at=t2-t1;
bt=t1;
ae=ei2-ei1;
be=ei1;
b=h;

K(1:2,1:2)=[1 -1;-1 1]*(ag/2+bg)/h;
K(3:6,3:6)=[6*ae+12*be  (2*ae+6*be)*b    -6*ae-12*be   (4*ae+6*be)*b;
```

```
          (2*ae+6*be)*b (ae+4*be)*b^2  (-2*ae-6*be)*b  (ae+2*be)*b^2;
           -6*ae-12*be  (-2*ae-6*be)*b   6*ae+12*be   (-4*ae-6*be)*b;
    (4*ae+6*be)*b (ae+2*be)*b^2  (-4*ae-6*be)*b (3*ae+4*be)*b^2]/(h^3);

Tension=[36*at+72*bt   (6*at+6*bt)*b    -36*at-72*bt  (6*bt)*b;
        (6*at+6*bt)*b  (2*at+8*bt)*b^2 (-6*at-6*bt)*b (-at-2*bt)*b^2;
        -36*at-72*bt   (-6*at-6*bt)*b   36*at+72*bt   (-6*bt)*b;
    (6*bt)*b       (-at-2*bt)*b^2  (-6*bt)*b   (6*at+8*bt)*b^2]/(60*h);
K(3:6,3:6)=K(3:6,3:6)+Tension;

% Below properties,m,I,e are for M matrix only.
am=m2-m1;
bm=m1;
ai=I2-I1;
bi=I1;
ae=e2-e1;
be=e1;

%Icg+me^2= d3*(x/h)^3+d2*(x/h)^2+d1*(x/h)+d0
d3=am*ae^2;
d2=ae^2*bm+2*am*ae*be;
d1=ai+am*be^2+2*ae*be*bm;
d0=bi+bm*be^2;

M(1:2,1:2)=[1*d3+2*d2+5*d1+20*d0  2*d3+3*d2+5*d1+10*d0;
            2*d3+3*d2+5*d1+10*d0  10*d3+12*d2+15*d1+20*d0]*h/60;

% me=g2*(x/h)^2+g1*(x/h)+g0;
g2=am*ae;
g1=am*be+ae*bm;
g0=bm*be;

M(3:6,1:2)=[13*g2+35*g1+147*g0   15*g2+28*g1+63*g0;
           (3*g2+7*g1+21*g0)*b   (4*g2+7*g1+14*g0)*b;
           22*g2+35*g1+63*g0     90*g2+112*g1+147*g0;
         (-4*g2-7*g1-14*g0)*b  (-10*g2-14*g1-21*g0)*b]*h/420;
M(1:2,3:6)=M(3:6,1:2)';

a=am;
%b=bm;
M(3:6,3:6)=[36*a+156*bm (7*a+22*bm)*h   27*a+54*bm  (-6*a-13*bm)*h;
      (7*a+22*bm)*h  (1.5*a+4*bm)*h^2 (7*a+13*bm)*h (-1.5*a-3*bm)*h^2;
       27*a+54*bm  (7*a+13*bm)*h     120*a+156*bm   (-15*a-22*bm)*h;
 (-6*a-13*bm)*h (-1.5*a-3*bm)*h^2 (-15*a-22*bm)*h (2.5*a+4*bm)*h^2]*h/420;
```

```
%
% Now, K and M are in the form of
% theta(i),theta(i+1), w(i), beta(i), w(i+1), beta(i+1)
%
% Do row/column switching to achieve
% theta(i),w(i), beta(i), theta(i+1), w(i+1), beta(i+1)
%
%====>move 2nd row/column in between 4th and 5th.

Mtemp=M;
Mtemp(:,2:3)=M(:,3:4);
Mtemp(:,4)=M(:,2);
M=Mtemp;
Mtemp(2:3,:)=M(3:4,:);
Mtemp(4,:)=M(2,:);
M=Mtemp;

Ktemp=K;
Ktemp(:,2:3)=K(:,3:4);
Ktemp(:,4)=K(:,2);
K=Ktemp;
Ktemp(2:3,:)=K(3:4,:);
Ktemp(4,:)=K(2,:);
K=Ktemp;
answer=[K;M];
```

```
%============================================================
% unify.m     subroutine to create spanwise statetion vector, r.
%                   used in modalspthr.m
%============================================================
% this program combines two sets of spanwise distance vectors
% namely r and V.  R=span length.

function [answer]=unify(r,V)
 cntr=1;
cntv=1;
i=1;
[m,n]=size(r);
while cntr <= m
  if r(cntr,1) > V(cntv,1)
    rr(i,1)=V(cntv,1);
    cntv=cntv+1;
    i=i+1;
  elseif r(cntr,1) == V(cntv,1)
    rr(i,1)=r(cntr,1);
    cntr=cntr+1;
    cntv=cntv+1;
    i=i+1;
  else
    rr(i,1)=r(cntr,1);
    cntr=cntr+1;
    i=i+1;
  end
end
answer=rr;
```

```
%============================================================
% prop2r.m     subroutine to make all properties have same length
%                      used in modalspthr.m
%============================================================
% This program expands a certain property to a desired
% spanwise locations.
%
function [answer]=prop2r(f,r)
X(1,1)=f(1,2);
cntr=2;
n=2;
[m,t]=size(r);
while cntr <= m
  if r(cntr,1) < f(n,1)
    slope=(f(n,2)-f(n-1,2))/(f(n,1)-f(n-1,1));
    C=(f(n-1,2)*f(n,1)-f(n,2)*f(n-1,1))/(f(n,1)-f(n-1,1));
    X(cntr,1)=slope*r(cntr,1)+C;
    cntr=cntr+1;
  else
    X(cntr,1)=f(n,2);
    cntr=cntr+1;
    n=n+1;
  end
end
answer=X;
```

```
%============================================================
% span.m    mki
%============================================================
% this routine converts a spanwise distribution into a discretized
% vector for use with the numerical integration, modalintthr.m
%============================================================
function [spanout] = span(spanin,rspan,numpts,ebar)
% spanin is the span varying property
% rspan is the radial station.
% radial station vector starts from inboard and goes out

[m,n] = size(spanin);
spanout = zeros(numpts,1);
        k1 = round(((rspan(1)-ebar)/(1-ebar))*numpts)+1;
        k2 = round(((rspan(2)-ebar)/(1-ebar))*numpts);
temp=round((k2-k1)/2+k1);
for j = k1:temp;
        spanout(j) = spanin(1);
end
for j = temp+1:k2
        spanout(j) = 0.5*(spanin(1)+spanin(2));
end
for i = 2:m-1;
        k1 = k2+1;
        k2 = round(((rspan(i+1)-ebar)/(1-ebar))*numpts);
        temp=round((k2-k1)/2+k1);
        for j = k1:temp;
           spanout(j) = spanin(i);
        end
        for j=temp+1:k2
           spanout(j) = (spanin(i)+spanin(i+1))/2;
        end
end
%temp=round((numpts-(k2+1))/2);
for j = k2+1:numpts;
        spanout(j) = spanin(m);
end
```

References

[1] R. Barrett, "Intelligent Rotor-Blade Actuation Through Directionally Attached Piezoelectric Crystals, " *46th Annual Forum*, American Helicopter Society, Washington D.C., 1990.

[2] R.L. Blisplinghoff, H. Ashley, and R.L. Halfman, "Aeroelasticity," Addison-Wesley, Cambridge, MA, 1955.

[3] R.A. Desjardins and W.E. Hooper, "Rotor Isolation of the Hingeless Rotor BO-105 and YUH-61 Helicopters, " Second European Rotorcraft and Powered Lift Aircraft Forum, Buckeburg, Federal Republic of Germany, Sept. 20-22, 1976.

[4] R.A. Desjardins and V. Sankewitsch, "Integrated Floor/Fuel Isolation System for the Model 234 Commercial Chinook," 5th European Rotorcraft and Powered Lift Aircraft Forum, Amsterdam, Paper No. 39, 1979.

[5] M. Drela, "XFOIL: An Analysis and Design System for Low Reynolds Number Airfoils," *Low Reynolds Number Aerodynamics.* Springer-Verlag Lecture Notes in Engineering, No. 54, 1989.

[6] M.E. Fox, "Blade-Mounted Actuation for Helicopter Rotor Control," Master's thesis, Massachusetts Institute of Technology, Department of Aeronautics and Astronautics, Cambridge, MA, June 1993.

[7] J.C. Garcia, "Active Helicopter Rotor Control Using Blade-Mounted Actuators," Master's thesis, Massachusetts Institute of Technology, Department of Mechanical Engineering, Cambridge, MA, February 1991.

[8] S.R. Hall and E.F. Prechtl, "Development of a Piezoelectric Servoflap for Helicopter Rotor Control," Proceedings of Active Materials and Smart Structures, Bellingham, WA, Oct. 10-12, 1994.

[9] S.R. Hall and N.M. Wereley, "Performance of Higher Harmonic Control Algorithms for Helicopter Vibration Reduction," Journal of Guidance, Control, and Dynamics, Vol. 16, No. 4, July-August 1993, pp. 793-797.

[10] P.W. Hardenberg and C. Niebanck, "Helicopter Airframe Variable Tune Vibration Absorber," AIAA/AHS Systems, Design and Operations Conference, San Diego, CA, Oct. 31-Nov. 2, 1984.

[11] W. Johnson, "Helicopter Theory," Princeton University Press, 1957.

[12] S. Kottapalli, S. Swanson, P. LeMasurier, and J. Wang, "Full-Scale Higher Harmonic Control Research to Reduce Hub Loads and Noise," *49th Annual Forum*, American Helicopter Society, St. Louis May 19-21, 1993.

[13] L. Meirovitch, "Elements of Vibration Analysis, Second Edition," McGraw-Hill Book Company, 1975.

[14] W. Miao, S. Kottapalli, and H. Frye, "Flight Demonstration of Higher Harmonic control (HHC) on S-76," *42nd Annual Forum*, American Helicopter Society, Alexandria, VA, 1986, pp. 777-791.

[15] T.A. Millott and P.P. Friedmann, "Vibration Reduction in Helicopter Rotors Using an Actively Controlled Partial Span Trailing Edge Flap Located on the Blade," NASA Contractor Report 4611, June 1994.

[16] S. Jacklin and K. Nguyen,"Full-Scale Wind Tunnel Test of a Helicopter Individual Blade Control System," *50th Annual Forum*, American Helicopter Society, Washington DC, May 11-13, 1994.

[17] D.M. Pitt and D.A. Peters, "Theoretical Prediction of Dynamic-Inflow Derivatives," *Vertica*, Vol.5, No.1, 1981, pp.21-34.

[18] E.F. Prechtl, "Development of a Piezoelectric Servo-Flap Actuator for Helicopter Rotor Control," Master's thesis, Massachusetts Institute of Technology, Cambridge, MA, May 1994.

[19] J. Shaw, N. Albion, E.J. Hanker, and R.S. Teal, "Higher Harmonic Control:Wind Tunnel Demonstration of Fully Effective Vibratory Hub Force Suppression," *41st Annual Forum*, American Helicopter Society, Fort Worth, TX, 1985.

[20] R.L. Spangler and S.R. Hall, "Piezoelectric Actuators for Helicopter Rotor Control," Space Systems Laboratory Report SSL No.1-89, Massachusetts Institute of Technology, Cambridge, MA, January 1989.

[21] K. Wilkerson and D. Linck, "The Application of Circulation Control Aerodynamics to a Helicopter Rotor Model," Journal of the American Helicopter Society, Vol. 19, No. 2, April 1974, pp. 2-16.

[22] E.R. Wood, R.W. Powers, J.H. Cline, and C.E. Hammond, "On Developing and Flight Testing a Higher Harmonic Control System," Jounal of the American Helicopter Society, Vol. 30, No. 1, 1985, pp.3-20.